

UNIVERSITY OF CALIFORNIA
RIVERSIDE

Data-Driven Analysis and Applications of Time-Synchronized
Waveform Measurements in Power Systems

A Dissertation submitted in partial satisfaction
of the requirements for the degree of

Doctor of Philosophy

in

Electrical Engineering

by

Milad Izadi

December 2022

Committee Members:

Dr. Hamed Mohsenian-Rad, Chairperson
Dr. Fabio Pasqualetti
Dr. Salman Asif

Copyright by
Milad Izadi
2022

The Dissertation of Milad Izadi is approved:

Committee Chairperson

University of California, Riverside

Acknowledgments

First and foremost, I would like to thank my wonderful advisor, Dr. Hamed Mohsenian-Rad, for his profound insight, careful guidance, and unconditional support throughout my Ph.D. program. He taught me to be curious, to never give up, and to look for answers to questions. Thank you!

Second, I would like to warmly thank my wonderful family, the beloved ones in Kermanshah, in Iran, for their continued support throughout my education. I sincerely thank my mom, my dad, my brother, and my sisters for making my education always their first priority and for having always high expectations for me. I love you!

I would also like to thank my dear friends and colleagues in Riverside, in California, and all over the world. I thank you all for being there for me, no matter what.

I would like to thank the members of my committee, Dr. Fabio Pasqualetti and Dr. Salman Asif, for their feedback, guidance, and thoughtful comments about my work. I would also like to thank the staff of the Department of Electrical Engineering for their help and assistance through the years.

Last but not least, I thank me for doing all this hard work, for never giving up, and for making it this far.

To my mom and my dad for their unending supports.

ABSTRACT OF THE DISSERTATION

Data-Driven Analysis and Applications of Time-Synchronized
Waveform Measurements in Power Systems

by

Milad Izadi

Doctor of Philosophy, Graduate Program in Electrical Engineering
University of California, Riverside, December 2022
Dr. Hamed Mohsenian-Rad, Chairperson

Real-time monitoring of the power electric grid is more important than ever, to prevent catastrophic failures and to support fast-acting power electronic devices, renewable energy resources, and extreme weather conditions. Accordingly, there is an emerging need to a new class of wide-area monitoring sensors that can capture time-synchronized voltage and current waveforms. This thesis is about the new *frontier* in the power system monitoring using *synchronized waveform measurements*.

Waveform Measurement Units (WMUs) are a *new* class of smart grid sensors that provide precise *time-synchronized voltage waveform and current waveform measurements*, also known as *synchro-waveform measurements*. WMUs can show the wave-shape of the voltage and current at very high resolutions. Further, the waveform measurements are precisely synchronized across different WMUs. The very high reporting rate of WMUs and the fact that we have access to synchronized waveform measurements, can significantly enhance our *understanding* and *awareness* about the status of the power electric grid and its components. However, the sole availability of such huge amount of data in itself is not

sufficient; we need to translate the WMUs data to actionable information to be useful.

This thesis provides new methodologies for the practical applications of synchro-waveform measurements in *event detection*, *event classification*, *event location identification*, and *event-based network parameters estimation*. An event is defined as any sort of change in any component across the power electric grid, with focus on sub-cycle events; which are the type of events that call for the use of waveform measurements. This thesis also presents real-life applications of synchronized waveform data for asset monitoring and wildfire monitoring.

Contents

List of Figures	xi
List of Tables	xiii
1 Introduction	1
1.1 Background	1
1.2 Motivation	2
1.3 Contribution	7
1.4 Definitions	11
2 Event Detection and Classification	14
2.1 Summary of Technical Contributions	15
2.2 Related Literature	16
2.3 Substitution Theorem	18
2.4 Intuition based on Circuit Analysis	20
2.5 Synchronized Lissajous Curves	22
2.6 Characteristics of the Synchronized Lissajous Curves	23
2.6.1 Area of the Synchronized Lissajous Curves	23
2.6.2 Rotational Angle of the Synchronized Lissajous Curves	25
2.6.3 Shape of the Synchronized Lissajous Curves	27
2.7 Event Detection Method	30
2.7.1 Similarity Index	30
2.7.2 Adaptive Detection Threshold	31
2.8 Event Classification Method	32
2.8.1 Challenging Factors	33
2.8.2 Synchronized Lissajous Curve as Image	36
2.8.3 Convolutional Neural Networks	37
2.9 Case Studies	39
2.9.1 Event Detection Results	41
2.9.2 Event Classification Results	44
2.9.3 Classification based on Images versus Time Series	47
2.9.4 Sensitivity Analysis	48
2.9.5 Performance Comparison	49
2.10 Experimental Results	52

2.10.1	Real-World Field Measurements	52
2.10.2	Hardware-in-the-Loop Testing	57
2.11	Conclusions of the Chapter	61
3	Event Location Identification	63
3.1	Summary of Technical Contributions	64
3.2	Related Literature	65
3.3	Modal Analysis of Synchronized Waveform Measurements	66
3.3.1	Single-Signal vs Multi-Signal Modal Analysis	67
3.3.2	Selecting the Time Window and the Number of Modes	70
3.3.3	Selecting the Dominant Transient Event Mode(s)	71
3.3.4	Comparison with Time Domain Analysis	72
3.4	Constructing the Feeder Model at the Dominant Transient Modes	73
3.4.1	Case I: Transient Event Does not Create a New Mode	74
3.4.2	Case II: Transient Event Creates a New Mode	75
3.4.3	Load Modeling in Cases I and II	76
3.5	Event Location Identification Method	77
3.5.1	Methodology	77
3.5.2	Algorithm	80
3.5.3	Extension to Arbitrary Number of WMUs	80
3.6	Case Studies	81
3.6.1	Scenario I: Sub-cycle Incipient Fault	82
3.6.2	Scenario II: Multi-cycle Incipient Fault	85
3.6.3	Scenario III: Permanent Fault	86
3.6.4	Scenario IV: Capacitor Bank Switching Event	86
3.6.5	Impact of Measurement Reporting Rate	87
3.6.6	Performance Comparison	88
3.6.7	Sensitivity Analysis	91
3.6.8	Active Distribution Networks	93
3.6.9	Extension to Unbalanced Three-Phase Networks	94
3.7	Conclusions of the Chapter	95
4	Network Parameters Estimation and Field Implementation	97
4.1	Problem Statement	99
4.2	Voltage Waveform Approximation	101
4.3	Reconstructing the Unknown Network Parameters	103
4.3.1	Intuition	103
4.3.2	Using Regression to Estimate Line Parameters	105
4.3.3	Selecting the Number of Line Segments	107
4.4	Event Location Identification	108
4.5	Case Studies	111
4.5.1	Line Parameter Estimation Result	111
4.5.2	Event Location Identification Results	114
4.6	Conclusions of the Chapter	116

5 Conclusions and Future Works	117
5.1 Conclusions	117
5.2 Discussion on Potential Real-Life Applications	120
5.3 Future Works	121
A Multi-Signal Modal Analysis	122
B Load Types	124
Bibliography	126

List of Figures

1.1	An example of real-world synchro-waveform measurements	5
1.2	An example for a sub-cycle incipient fault on a distribution feeder	6
2.1	Application of the substitution theorem	18
2.2	An example of the synchronized Lissajous curve	20
2.3	The angle in the synchronized Lissajous curves	26
2.4	Five cycles of synchronized Lissajous curves for three different types of events	29
2.5	The impact of different firing angles on the synchronized Lissajous curves .	33
2.6	The impact of different locations on the synchronized Lissajous curves . .	34
2.7	The impact of different fault parameters on the synchronized Lissajous curves	35
2.8	The IEEE 33-bus distribution system with two WMUs	40
2.9	The results for event detection	42
2.10	Confusion matrix of the proposed method and competing RNN-based method	45
2.11	The ROC curve of the proposed event classifier	47
2.12	Confusion matrix for the state-of-the-art method	51
2.13	An example for real-world synchronized waveform measurements	53
2.14	Another example for real-world synchronized waveform measurements . .	54
2.15	The results of event detection applied to real-world synchronized measurements	55
2.16	Nine cycles of the synchronized Lissajous curves of waveforms in Fig. 2.13 .	56
2.17	Nine cycles of the SPM curves of waveforms in Fig. 2.13	56
2.18	Nine cycles of the synchronized Lissajous curves of waveforms in Fig. 2.14 .	58
2.19	Nine cycles of the SPM curves of waveforms in Fig. 2.14	58
2.20	The architecture of the implemented HIL testing experiments	59
2.21	Confusion matrix of the proposed event classification method	61
3.1	Synchronized waveform measurements during an incipient fault	68
3.2	Synchronized waveform measurements during a capacitor switching	69
3.3	A power distribution feeder that is equipped with two WMUs.	73
3.4	Analysis of voltage and current waveforms at a line segment	74
3.5	The IEEE 33-bus distribution system with five WMUs	82
3.6	Discrepancy index in Scenario I	84
3.7	Discrepancy index in Scenario II	85

3.8	Discrepancy index in Scenario III	86
3.9	Discrepancy index in Scenario IV	87
3.10	The results of estimating the impedance of an incipient fault	89
3.11	Comparing the discrepancy indices in an <i>active</i> network and a <i>passive</i> network	94
3.12	Discrepancy indices in an <i>unbalanced three-phase</i> network	95
4.1	Real-world synchronized e-field and current waveform measurements	100
4.2	An illustration to reconstruct an unknown distribution feeder	105
4.3	The single line diagram of the real-world power distribution feeder	112
4.4	Distribution of (a) the combined resistance; (b) the combined inductance .	112
4.5	Discrepancy index using waveform measurements from line-mounted sensors	115
A.1	An example for multi-signal Prony analysis in Appendix A	123

List of Tables

2.1	The Structure of the Proposed CNN Model	38
2.2	Performance Metrics of the Confusion Matrix in Fig. 2.10(a)	46
3.1	Dominant Mode of the Transient Event in Fig. 3.1	68
3.2	Dominant Modes of the Transient Event in Fig. 3.2	69
3.3	Comparison Between state-of-the-art Methods and the Proposed Method	90
3.4	Impact of Error in Line Parameters	92
3.5	Impact of Error in Pseudo-Measurements	92
3.6	Impact of Harmonic Distortion and Measurement Noise	93
4.1	Results of the Event-based Line Parameter Estimation	113

Chapter 1

Introduction

1.1 Background

The power electric grid consists of four main sectors: *generation*, *transmission*, *distribution*, and *consumption*; it delivers the electricity from generators to consumers through transmission and distribution systems [1]. The electricity is mostly delivered in the form of *alternating current* (AC) power with voltage and current that vary *sinusoidally* in time. The generation sector generates the AC power. The transmission system increases the generation voltage level to a higher level to carry the electricity over long distances from the generation to the distribution system. The distribution system reduces the transmission voltage level to a lower level to deliver the electricity to customers. The consumption sector consumes the AC power. Among these four sectors, power distribution systems comprise the bulk of the power electric grid. They are also the most vulnerable part of the grid since they are continuously exposed to all kind of *events*, where an event is any kind of change, minor and major, in any component across the grid that is worth studying [2]. Further-

more, the basic parameters of most distribution systems, such as line parameters, are often *unreliable* or even *not known* [3]. Thus, it is *critical* to study power distribution systems.

The modern power electric grid has been facing with a wide range of challenges: *load diversification, fast-acting power electronic devices, renewable energy resources, and extreme weather conditions*. The integration of new types of electrified technologies, such as plug-in electric vehicles, has increased the diversity of loads. The implementation of fast-acting power electronic devices, such as inverter-based resources, has introduced harmonics and inter-harmonics into the power system, specially at the distribution circuits. The proliferation of renewable energy resources, such as solar farms, has added significant complexity to the structure of the grid. Extreme weather conditions, such as wildfires, have been a serious threat to the grid component which consequently cause more frequent events. These challenges have highlighted the need for better real-time monitoring and situational awareness of the modern power electric gird. This is particularly *necessary* in power distribution systems, which are frequently exposed to various sources of events. Therefore, this thesis is about situational awareness in power distribution systems.

1.2 Motivation

The *first critical* step to address the challenges in Section 1.1 is to modernize the power electric grid to make it “smart” through the use of cutting-edge technologies, such as *smart grid sensors* [4]. Smart grid sensors provide a wide range of benefits for real-time monitoring and situational awareness in the power distribution system. Measurements from sensors can help us gain a better *understanding* and *awareness* about the operational status

of the system and its components. The three main classes of smart grid sensor technologies that are available on power distribution systems are explained as follows.

Supervisory control and data acquisition (SCADA) are the *old class* of sensors that have been integrated widely into distribution systems over the past fifty years ago [5]. SCADA systems report the root-mean-square (RMS) representation of the voltage and current measurements. They operate at low reporting rates, such as 1 sample per second.

Phasor measurement units (PMUs) are *another class* of smart grid sensors that have been deployed in distribution systems over the past two decades [6]. PMUs report the phasor representation of the voltage and current measurements. They are equipped with global positioning system (GPS) to provide *time-synchronized phasor* measurements, also known as *synchro-phasor*. PMUs operate at high reporting rates, such as 2 samples per AC cycle, i.e., 120 samples per second.

Although both of the above two classes of smart grid sensors, i.e., SCADAs and particularly PMUs, bring significant advancements for monitoring and situational awareness in power distribution systems, they are primarily limited when the voltage and current waveforms include *distortions* and take *non-sinusoidal* shape [7] or when events have very short duration [8], which are increasingly common situations in the modern power electric grid. This has highlighted an emerging need to a new class of smart grid sensors that can capture the actual voltage and current waveforms, instead of their representations, with extremely higher reporting rate.

Waveform measurement units (WMUs) are the *new class* of smart grid sensors that have been emerging recently [2, 3, 7–13]. WMUs report the waveform of the voltage

and current measurements in time-domain, i.e., they record the wave-shape of the voltage and current. They are equipped with GPS to provide *time-synchronized waveform* measurements, also known as *synchro-waveform* [2, 7]. WMUs operate at very high reporting rates, such as 256 samples per AC cycle, i.e., 15,360 samples per second. This is much higher than the reporting rates of SCADAs and PMUs [8–10]. At such high reporting rate, a WMU reports $7,962,624,000 = 256 \times 60 \times 60 \times 60 \times 24 \times 2 \times 3$ data samples per day from voltage and current waveforms on three phases. This is an overwhelming amount of data to report. Furthermore, given that one data sample requires 2 bytes of memory [14], then we will need over 15.9 GB of memory to store only one day of data recorded by a WMU. This is a huge volume of memory just for one WMU. Therefore, the data from WMUs can eventually form Big Data in power systems [15].

The first field installations of WMUs are in our test bed power distribution feeders in Riverside, CA. Fig. 1.1 shows an example of the synchronized voltage waveform and the synchronized current waveform measurements that are captured by two WMUs during an event on a real-life distribution feeder in Riverside, CA. The event occurs at 13:38:20.705 on December 1, 2021. It immediately creates a sudden drop in the voltage waveforms on Phase B and particularly on Phase A. It also causes a sudden rise in the current waveforms on the same two phases. This eventually evolves into Phase C due to the mutual coupling between the three phases. Furthermore, the event creates a momentary ringing distortion in the waveforms due to the resonance formed between capacitor banks and inductive loads across the distribution system. This example shows that waveforms show *much more details* about the event.

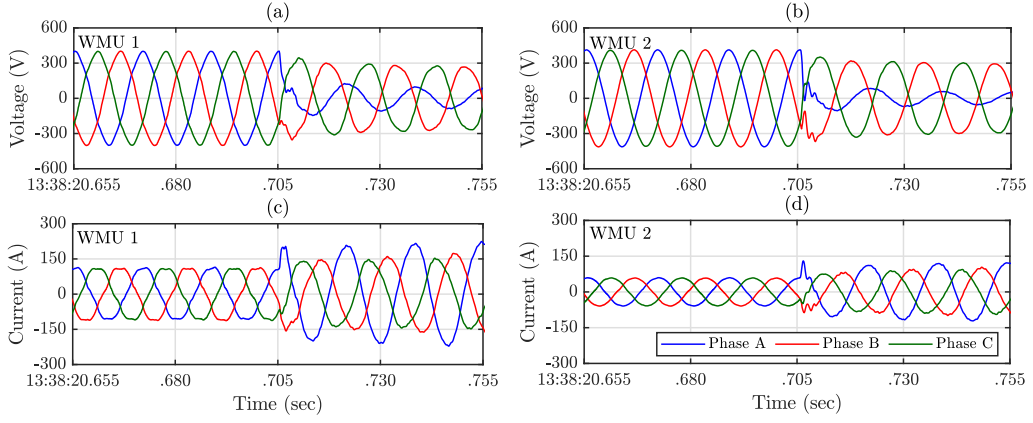


Figure 1.1: Real-world three-phase synchronized voltage waveform and synchronized current waveform that are measured by two WMUs on a distribution feeder in Riverside, CA during an event that occurred on December 1, 2021: (a)-(c) voltage and current waveforms at WMU 1; (b)-(d) voltage and current waveforms at WMU 2.

Accordingly, the synchro-waveform measurements from WMUs can significantly improve our *understanding* and *awareness* about the root cause of events and particularly transient events in power distribution systems, specifically, when we compare them with the synchro-phasor measurements from PMUs. Fig. 1.2 shows an example of data from two PMUs (also known as D-PMUs in distribution systems) and two WMUs [8]. They both represent *the exact same event*, which is an incipient fault, at *the exact same time*. An incipient fault occurs when there is a crack in the insulation of an equipment, such as a cable, which ignites an electric arc [8, 16]. Incipient faults are typically *self-clearing* faults and have short duration, ranging from a quarter of an AC cycle (sub-cycle), to up to four AC cycles (multi-cycle) [17]. In this example, PMU 1 and WMU 1 are installed at the beginning of the power distribution feeder; and PMU 2 and WMU 2 are installed at the end of the feeder. The incipient fault causes very small changes in the phasor measurements of the PMUs, see Figs. 1.2(b) and (c). The exact shape of such small changes depends on the

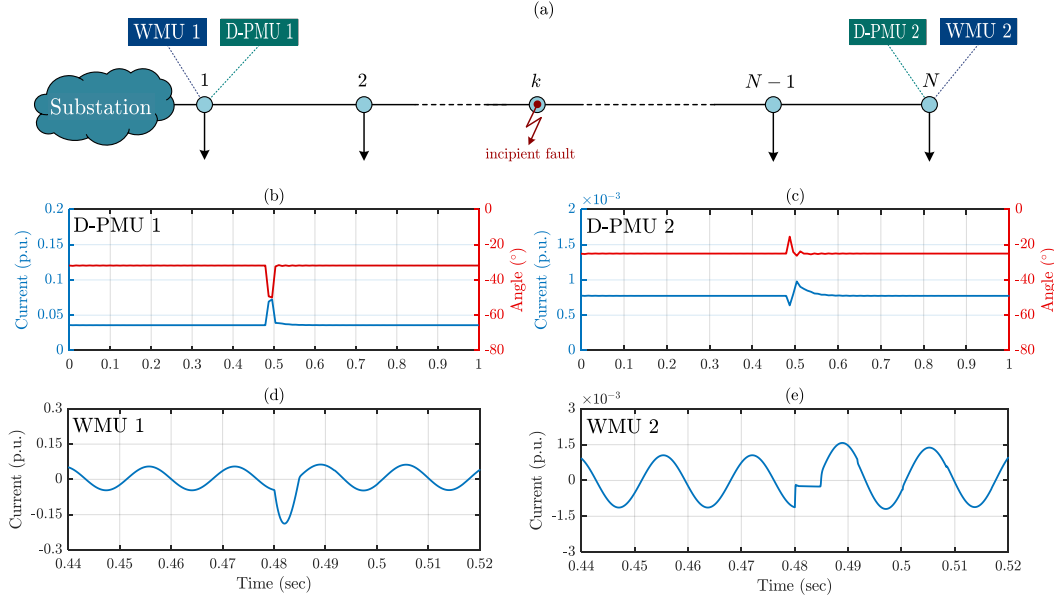


Figure 1.2: An example for a sub-cycle incipient fault on a distribution feeder that is seen by two PMUs versus by two WMUs: (a) the locations of the sensors; (b)-(c) synchronized current phasor measurements from the two PMUs; (d)-(e) synchronized current waveform measurements from the two WMUs. PMUs that are deployed in distribution systems are known as D-PMUs.

internal filtering, the size of the measurement window, and other dynamic characteristics of the PMUs. Importantly, these small changes in synchro-phasors are *not* much informative; because they appear just like a normal variation in current, as opposed to an indication of an incipient fault. In a sharp contrast, the impact of the incipient fault is clearly visible in the waveform measurements of the two WMUs, see Figs. 1.2(d) and (e). This example further highlights the need for using synchro-waveform data from WMUs, instead of the phasor data, for advanced situational awareness.

1.3 Contribution

Motivated by the discussion and examples in Section 1.2, our focus in this thesis is on the use of synchro-waveform data from WMUs for situational awareness in power distribution systems. However, data availability in itself does not lead to enhanced situational awareness and grid intelligence. We need to translate the WMU data to insightful and actionable knowledge. This thesis primarily addresses this open problem to provide awareness of the system condition to the grid operator and various engineering applications by leveraging high-resolution synchro-waveform measurements.

To such aim, this thesis develops data analytic techniques and computational algorithms to analyze the data from WMUs to turn the gigabytes of synchro-waveform data into useful knowledge. Particularly, it proposes a *situational awareness framework* using the WMUs data that includes *event detection*, *event classification*, *event location identification*, and *event-based network parameters estimation*. The rest of the thesis is organized as follows.

- Chapter 2 presents new methods to *detect* and *classify* events in power distribution systems by using synchro-waveform measurements. The methods are built upon a novel graphical concept, called *synchronized Lissajous curve*; where we plot the synchronized voltage waveform versus the synchronized current waveform measurements. The proposed event detection and event classification methods work by analyzing the shape of the synchronized Lissajous curves during disturbances and events. The proposed event detection method monitors the changes in the areas of two successive synchronized Lissajous curves. Once an event occurs, the area sharply changes,

indicating that an event has occurred. The impact of challenging factors, such as the angle, the location, and other parameters of the event are discussed. We show that these challenges can be addressed if we treat the synchronized Lissajous curves as *images*, instead of as time series as in the raw synchronized waveform measurements. Hence, we can take advantage of the recent advancements in the field of *image processing* so as to capture the overall characterizing patterns in the shapes of the synchronized Lissajous curves. The proposed event classification method works by classifying the synchronized Lissajous images. We develop a Convolutional Neural Network (CNN) method to classify the events, where the input is the synchronized Lissajous images. The effectiveness of the proposed event detection and classification methods is demonstrated through computer simulations, including hardware-in-the-loop simulations, and real-world field data. Multiple case studies verify the performance of the proposed methods. The proposed event detection method can accurately detect events, and identify the start time and the end time of each event. The proposed event classification method can classify power quality events with high accuracy. The proposed detection and classification methods do *not* require any prior knowledge about the network. They use data from as few as *only two* WMUs.

The content of this chapter is a reprint of the material that are appeared in the following publications:

- **Milad Izadi** and Hamed Mohsenian-Rad, “A Synchronized Lissajous-based Method to Detect and Classify Events in Synchro-waveform Measurements in Power Distribution Networks,” *IEEE Transactions on Smart Grid*, May 2022.

- **Milad Izadi** and Hamed Mohsenian-Rad, “Characterizing Synchronized Lissajous Curves to Scrutinize Power Distribution Synchro-waveform Measurements,” *IEEE Transactions on Power Systems*, September 2021.
- **Milad Izadi** and Hamed Mohsenian-Rad, “A Synchronized Lissajous-based Approach to Achieve Situational Awareness Using Synchronized Waveform Measurements,” *Proc. of IEEE Power and Energy Society General Meeting*, Washington, DC, July 2021.
- Chapter 3 presents a new method to *identify the location* of events, particularly incipient faults and transient events, in power distribution systems, by using synchro-waveform measurements from WMUs. The proposed event location identification method consists of three steps. The first step is to characterize the oscillatory modes of the transient components of all the captured synchronized voltage and current waveforms from all WMUs, by conducting a multi-signal modal analysis. The second step is to construct a circuit model for the underlying distribution feeder at the identified dominant mode(s) of the transient event. The final step is to identify the location of the transient event with the means of a method that involves certain forward and backward analyses of the constructed circuit model. The proposed event location identification method requires installing as few as only two WMUs. It can also utilize several synchronized waveform measurements when several WMUs are available. The performance of the proposed method is assessed on a test system; for different cases of transient events, such as sub-cycle incipient faults, multi-cycle incipient faults, permanent faults, as well as benign yet informative events such as capacitor bank switching.

The results verify the accuracy and robustness of the proposed method in identifying the location of events in distribution networks.

The content of this chapter is a reprint of the material that are appeared in the following publications:

- **Milad Izadi** and Hamed Mohsenian-Rad, “Synchronous Waveform Measurements to Locate Transient Events and Incipient Faults in Power Distribution Networks,” *IEEE Transactions on Smart Grid*, September 2021.

- **Milad Izadi** and Hamed Mohsenian-Rad, “Event Location Identification in Distribution Networks Using Waveform Measurement Units,” *Proc. of IEEE PES Innovative Smart Grid Technologies Europe*, The Hague, Netherlands, October 2020.

- Chapter 4 presents an event-based method to *estimate* the basic network parameters of power distribution systems in order to *identify* the location of events without having information about the network. In this chapter, we study a real-world field case, where the network parameters of the understudy distribution feeder is not known. Instead, we are provided with the time-synchronized *electric field (e-field) waveform* and *current waveform* measurements from a group of line-mounted sensors [18] at four sites of a three-phase power distribution feeder in the United States. These line-mounted sensors are similar to WMUs, but they do *not* report voltage waveform; instead, they report e-field waveform. Our goal in this chapter is to estimate network parameters of the unknown real-world distribution feeder and then to identify the source location of events in the reconstructed distribution feeder using data from a few line-mounted

sensors. This framework consists of three steps. The first step is to approximate the voltage waveform from the available e-field waveform measurement provided by the line-mounted sensors. The second step is to develop a novel event-based network parameters estimation method to completely reconstruct the circuit model of the understudy distribution feeder by leveraging the approximated voltage waveform and the current waveform measurements. The final step is to identify the location of the event by adopting the proposed event location identification method in Chapter 3 on the data-driven reconstructed circuit model. The framework in this chapter is purely data-driven and model-free. Despite not using any knowledge about the network parameters and only using measurements from a few line-mounted sensors, the results demonstrate the accuracy and consistency of the proposed framework in identifying the location of the events in real-world distribution systems.

The content of this chapter is a reprint of the material that are appeared in the following publication:

- **Milad Izadi**, Mirrasoul J. Mousavi, Jong Min Lim, and Hamed Mohsenian-Rad, “Data-Driven Event Location Identification Without Knowing Network Parameters Using Synchronized Electric-Field and Current Waveform Data,” *Proc. of IEEE Power and Energy Society General Meeting*, Denver, CO, July 2022.

1.4 Definitions

The following technical terms are used throughout this thesis.

Waveform Measurement Unit (WMU): A smart grid sensor that reports synchro-waveform measurements of AC voltage and AC current in time-domain using a GPS clock.

Synchro-waveform (or Synchronized Waveform): An AC waveform provided by a WMU which is time-stamped to the Universal Time Coordinated (UTC) standard time.

Line-mounted Sensor: A non-contact smart grid sensor that reports synchro-waveform measurements of AC electric-field and AC current in time-domain.

Phasor Measurement Unit (PMU): A smart grid sensor that reports synchro-phasor measurements of voltage and current using a GPS clock.

Synchro-phasor (or Synchronized Phasor): A phasor representation of an AC waveform provided by a PMU which is time-stamped to the UTC standard time.

Event (or Disturbance): Any kind of changes in any component across the power electric grid that is worth studying.

Cycle: A cycle takes $1/60$ seconds = 16.67 msec at a 60 Hz power system.

Incipient Fault: An event that is caused when there is a crack in the insulation of an equipment, e.g., a cable, which ignites an electric arc. It is typically self-clearing faults and has very short duration, ranging from a quarter of an AC cycle (sub-cycle), to up to four AC cycles (multi-cycle).

High Impedance Fault: A event that is caused when there is an electrical contact between an energized conductor, such as a power line, with a high grounding impedance surface, such

as a tree. It typically has a small fault current and odd-harmonics nonlinear characteristics.

Capacitor Bank Switching: A event that is caused when a capacitor bank switches on or off in the electric grid. It typically causes an immediate rise in the voltage and creates high frequency oscillatory transient mode in AC waveforms.

Lissajous Curve (or Lissajous Graph): A graph that is obtained by plotting one AC waveform versus another AC waveform.

Synchronized Lissajous Curve: A graph that is constructed by plotting the *difference* of two synchronized voltage waveforms versus the *difference* of two synchronized current waveforms.

Convolutional Neural Networks (CNN): A class of deep learning artificial neural networks that is typically used for image classification.

Chapter 2

Event Detection and Classification

In this chapter, we propose new methods to *detect* and *classify* power quality events in power distribution systems by using synchro-waveform measurements. The methods are built upon the substitution theorem, a circuit analysis intuition, and a novel graphical concept, called *synchronized Lissajous curve*. The fundamental characteristics of the synchronized Lissajous curves are discussed. The proposed event detection and event classification methods work by analyzing the *shape* of the synchronized Lissajous curves during disturbances and events. The impact of challenging factors, such as the angle, the location, and other parameters of the event are discussed. We show that these challenges can be addressed if we treat the synchronized Lissajous curves as *images*, instead of as time series as in the raw synchronized waveform measurements. We develop a Convolutional Neural Network (CNN) method to classify the events, where the input is the synchronized Lissajous images. The effectiveness of the proposed event detection and classification methods is demonstrated

through computer simulations, including hardware-in-the-loop simulations, and real-world field data. The proposed detection and classification methods do *not* require any prior knowledge about the network. They use data from as few as *only two* WMUs.

2.1 Summary of Technical Contributions

The main contributions of the work in this chapter are as follows:

1. A new data-driven situational awareness framework is proposed in power distribution systems based on the analysis of synchro-waveform measurements. The new framework is built upon the new concept of synchronized Lissajous curves. During normal operating conditions, the synchronized Lissajous curve is an ellipse. Once an event occurs, the *shape* and the *area* of the synchronized Lissajous curve can change significantly, depending on the type, location, and other characteristics of the event.
2. The *characteristics* of the synchronized Lissajous curves during event conditions are investigated. Three key quantitative features are extracted, namely *area*, *rotational angle*, and *shape*. Through illustrative examples, the applications of each of these key features are investigated.
3. It is shown that the areas of synchronized Lissajous curves have physical meanings; as they resemble the weighted sum of active power and the weighted sum of reactive power. The areas can also be used to *detect* the event. The rotational angle of the synchronized Lissajous curves provide clear insight about the *location* of the event. The shape of the synchronize Lissajous curves help distinguish the *type* of the event.

4. The proposed event detection method monitors the changes in the areas of two successive synchronized Lissajous curves. Once an event occurs, the area sharply changes, indicating that an event has occurred. We present an adaptive detection threshold based on a statistical threshold selection method that is robust against outliers.
5. The proposed event classification method works by classifying the synchronized Lissajous *images*. A Convolutional Neural Network (CNN) is developed as the image classification method. Our approach is in sharp contrast to the common practice in the literature to conduct classification based on the time series of the waveform measurements. The proposed method reaches a high accuracy, even at lower measurement reporting rates, under missing data, and under major measurement noise.
6. The proposed framework is able to correctly detect and classify a wide range of events, such as sustained events with steady-state component, e.g., high impedance fault; sustained events with transient component, e.g., capacitor bank switching; and temporary events with very short duration, e.g., incipient faults. The proposed detection and classification methods are model-free and they do *not* require any knowledge about the network. These methods require data from as few as only two WMUs.

2.2 Related Literature

For a method to be truly relevant to synchro-waveform measurements, it must take advantage of the *synchronized* waveform measurements from *multiple* WMUs. However, even before the development of synchro-waveforms, there was a literature on the analysis of waveform measurements that come from *individual* power quality sensors. Both event

detection and event classification are addressed in such literature; but the focus has been mainly on major events such as major faults.

Traditionally, a common approach in event detection has been to monitor the changes in the root-mean-square (RMS) of the voltage waveforms, e.g., in [19]. There are other methods that work based on signal processing tools, such as wavelet transform [20], wavelet packet transform [21], S-transform [22], and Fourier transform [23]. Although these methods perform well in many cases, they are often sensitive to the presence of harmonics in the waveforms and also to the parameters of the transformation technique that is being used. Unlike the above and other similar methods, the event detection method in this chapter is meant for *synchro-waveform* measurements as it takes direct advantage of the multiple available synchronized waveform measurements. It works in time-domain therefore it does not require any data transformation. It is not sensitive to harmonics. Furthermore, it makes use of both the synchronized voltage waveform and the current waveform measurements.

As for the traditional methods on event classification, various techniques have been used, such as decision trees [24], neural networks [25], support vector machines [26], and hierarchical process [27]. The common approach in the above papers and other similar studies is to conduct event classification based on the *time series* data that come from power quality sensors. In a sharp contrast, here we propose a fundamentally different approach to conduct event classification based on the graphical representation of the events in Lissajous images. Accordingly, our method is a CNN-based image classification. It is designed to use both the synchronized voltage waveform measurements and the synchronized current waveform measurements.

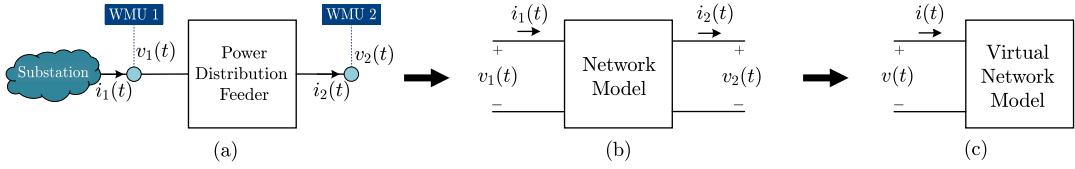


Figure 2.1: System Model: (a) a distribution feeder that is equipped with two WMUs; (b) the equivalent two-port network; (c) the virtual one-port network.

There is a limited literature on classifying power quality events using image classification methods, including different choices of CNN models. For example, in [28–30], wavelet transformation is used to generate *scalogram* image representation for the power quality events. As another example, in [31], image representation of the waveforms is done by using the *space-phasor* analysis and discrete quantization.

2.3 Substitution Theorem

According to the *substitution theorem* in Circuit Theory, an element in a circuit can be replaced by a voltage source or a current source that represents the characteristics of the element, c.f. [32]. Hence, we propose to model the network that is seen by each WMU with an AC voltage source based on the WMU's voltage waveform measurements and an AC current source based on the WMU's current waveform measurements.

Consider the power distribution feeder in Fig. 2.1(a). Suppose it is equipped with two WMUs, where WMU 1 is installed at the beginning of the feeder and WMU 2 is installed at the end of the feeder. Let $v_1(t)$ denote the voltage waveform and $i_1(t)$ denote the current waveform that are measured by WMU 1. Also, let $v_2(t)$ denote the voltage

waveform and $i_2(t)$ denote the current waveform that are measured by WMU 2. According to the *substitution theorem*, we can replace the network at WMU 1 with voltage source $v_1(t)$ and current source $i_1(t)$, which are connected in *series*, as shown in Fig.2.1(b). Similarly, we can replace the network at WMU 2 with voltage source $v_2(t)$ and current source $i_2(t)$, which are connected in *series*, as shown in Fig. 2.1(b). Together, WMU 1 and WMU 2 simultaneously monitor the feeder as a two-port network, as shown in Fig. 2.1(b). When an event or a disturbance occurs on the power distribution feeder, it may affect the voltage and current waveforms that are measured by WMU 1 as well as the voltage and current waveforms that are measured by WMU 2. The *relative* impact with respect to these two pairs of synchronized waveform measurements can reveal the characteristics of the event or disturbance. Therefore, next, we revise the two-port network model in Fig. 2.1(b) into a one-port network model in Fig. 2.1(c). Let us define:

$$v(t) = v_1(t) - v_2(t), \quad (2.1)$$

$$i(t) = i_1(t) - i_2(t), \quad (2.2)$$

as the *difference* between the synchronized voltage waveforms at WMU 1 and WMU 2, and the *difference* between the synchronized current waveforms at WMU 1 and WMU 2, respectively. By construction, $v(t)$ and $i(t)$ capture the *synchronized* nature of the waveform measurements that are obtained by WMU 1 and WMU 2. The one-port network model is a *virtual* model. It can help us in discussing the concepts that we introduce in this chapter. For example, consider the product $v(t) i(t)$. While this product may *not* be intuitive if it is defined based on the initial two-port physical network model in Fig. 2.1(b), it *is* intuitive when it is defined based on the one-port virtual network model in Fig. 2.1(c); because it

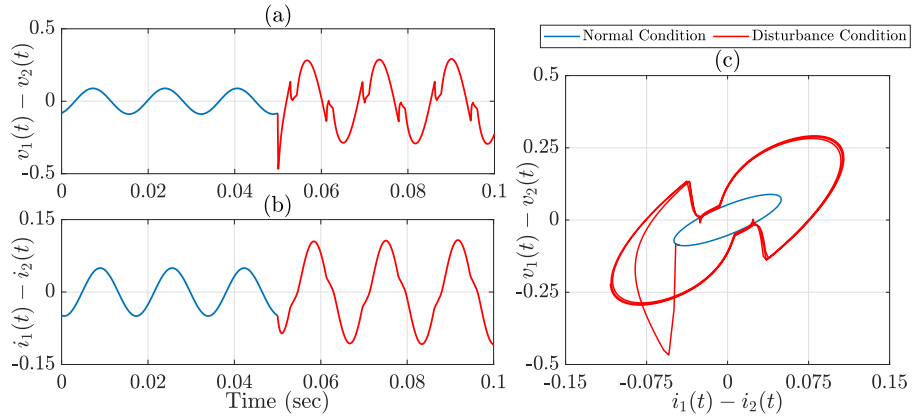


Figure 2.2: An example of the synchronized Lissajous curve for a high impedance fault on a distribution feeder that is seen by two WMUs during normal operating conditions (blue) and disturbance conditions (red): (a) the difference of two synchronized voltage waveform; (b) the difference of two synchronized current waveform measurements; (c) the corresponding synchronized Lissajous curve.

simply denotes the instantaneous power that is injected into such *virtual* network model. Any other discussion involving the *difference* waveform measurements $v(t)$ and $i(t)$ can be similarly explained in the context of such virtual network model. The waveforms in (2.1) and (2.2) are in *per unit*; i.e., they are normalized to be comparable. Figs. 2.2(a) and (b) show examples of the synchronized waveforms in (2.1) and (2.2) that are captured by WMUs 1 and 2 when a power quality disturbance occurs. The impact of the disturbance is clearly visible in these synchronized waveforms.

2.4 Intuition based on Circuit Analysis

Even though the analysis in this chapter is data-driven, one can still discuss the event-triggered changes in synchronized waveforms also in the context of the underlying power distribution circuit. Such analysis can provide additional insights on why it is rea-

sonable to use the voltage waveform in (2.1) and the current waveform in (2.2) for the purpose of obtaining the synchronized Lissajous curve, as we will introduce in Section 2.5. To see this, again consider the power distribution feeder with two WMUs that we saw in Fig. 2.1(a). Suppose an event occurs somewhere between the two WMUs. Once the event occurs, almost the entire event current flows through the substation at the upstream of the event, as opposed to flowing through the loads at the downstream of the event bus. This physical concept is commonly used in the literature in power distribution systems, e.g., see [1]; and it can be explained by comparing the Thevenin equivalent of the circuit at the upstream of the event with the Thevenin equivalent of the circuit at the downstream of the event. In particular, since the Thevenin impedance of the substation at the upstream of the event is much smaller than the Thevenin impedance of the loads at the downstream of the event, the event current is approximately equal to the change in the waveform $i_1(t) - i_2(t)$ that is defined in (2.2), i.e., the change in the difference between the current waveform at WMU 1 and the current waveform at WMU 2. As a result, the waveform in (2.2) provides valuable information about the current characteristics of the event.

We can similarly explain the physical intuition for the definition of the waveform in (2.1). Given the fact that the event current does not flow through the loads at the downstream of the event, it does *not* cause any change in the voltage at the buses at the downstream of the event. However, since the event current flows through the substation at the upstream of the event, it *does* cause some changes in the voltage at the buses at the upstream of the event. As a result, the change in voltage that is caused at the location of the event, which we can refer to as the event voltage, is approximately equal to the change

in the waveform $v_1(t) - v_2(t)$ that is defined in (2.1), i.e., the change in the difference between the voltage waveform that is measured at WMU 1 and the voltage waveform that is measured at WMU 2. As a result, the waveform in (2.1) provides valuable information about the voltage characteristics of the event.

Accordingly, the voltage waveform difference in (2.1) and the current waveform difference in (2.2) can capture both the voltage characteristics and the current characteristics of the event, despite the fact that WMU 1 and WMU 2 are not at the location of the event; as the event rather occurs at an arbitrary location between WMU 1 and WMU 2.

2.5 Synchronized Lissajous Curves

A Lissajous curve is a graph that is constructed by plotting one waveform versus another waveform. It has various applications in signal and image processing; such as in electrocardiogram analysis and dielectric discharge analysis [33]. Furthermore, the Lissajous curves have had occasional applications also in power system engineering; such as to analyze non-linear single-phase circuits [34] or to identify fault location in transmission lines [35]. However, these existing applications have focused on the specific physical characteristics of the particular circuit or the particular equipment of interest.

In this thesis, we propose to plot the voltage waveform *difference* in (2.1) versus the current waveform *difference* in (2.2). We refer to such Lissajous curve as the *synchronized Lissajous curve* [7, 9]; because it is constructed based on synchronized waveform measurements in WMU 1 and WMU 2.

The synchronized Lissajous curve that is corresponding to the waveforms in Fig. 2.2(a) and (b) is shown in Fig. 2.2(c). The blue curve represents the *pre-disturbance* conditions, i.e., the normal operating conditions before the disturbance occurs. The red curve represents the *post-disturbance* conditions, i.e., the circumstances immediately after the disturbance occurs.

As we will explain in Section 2.7 and Section 2.8, the above novel graphical concept is well-suited to help us detect and identify different types of events that occur at power distribution networks and captured by WMUs. However, we will first study the fundamental characteristics of the synchronized Lissajous curves, namely *area*, *rotational angle*, and *shape*, both analytically and through examples.

2.6 Characteristics of the Synchronized Lissajous Curves

In this section, we investigate the fundamental characteristics of the synchronized Lissajous curves that we introduced in Section 2.5, and what they reveal about the events.

2.6.1 Area of the Synchronized Lissajous Curves

We can define the area of the synchronized Lissajous curve in each cycle T as:

$$Area_{v-i} = \left| \int_{i(t=0)}^{i(t=T)} v(t) di(t) \right|. \quad (2.3)$$

The above area can be obtained in *closed-form* during the *steady-state* conditions both before and after the event occurs. At steady-state conditions, we can express $v(t)$ and $i(t)$ as follows:

$$v(t) = \sum_{h=1}^H V_h \cos(h\omega t + \theta_h), \quad (2.4)$$

$$i(t) = \sum_{h=1}^H I_h \cos(h\omega t + \gamma_h), \quad (2.5)$$

where ω is the fundamental rotational frequency; h is the harmonic order; V_h and θ_h are the magnitude and phase angle of the h th harmonic of the voltage waveform; I_h and γ_h are the magnitude and phase angle of the h th harmonic of the current waveform; and H is the maximum number of harmonic orders.

From (2.3), (2.4), (2.5), we can go through all the steps to obtain the equation for the area as follows:

$$\begin{aligned} Area_{v-i} &= \left| \int_{i(t=0)}^{i(t=T)} v(t) di(t) \right| \\ &= \left| \int_{t=0}^T \left(\sum_{h=1}^H V_h \cos(h\omega t + \theta_h) \right) \left(- \sum_{h=1}^H h\omega I_h \sin(h\omega t + \gamma_h) \right) dt \right| \quad (2.6) \\ &= \left| - \sum_{h=1}^H \sum_{k=1}^H k\omega V_h I_k \left(\int_{t=0}^T \cos(h\omega t + \theta_h) \sin(k\omega t + \gamma_k) dt \right) \right|. \end{aligned}$$

Next, we note that

$$\begin{aligned} \cos(h\omega t + \theta_h) \sin(k\omega t + \gamma_k) &= \frac{1}{2} \left(\sin((h+k)\omega t + \theta_h + \gamma_k) \right. \\ &\quad \left. - \sin((h-k)\omega t + \theta_h - \gamma_k) \right). \end{aligned} \quad (2.7)$$

Therefore, we have:

$$\int_{t=0}^T \cos(h\omega t + \theta_h) \sin(k\omega t + \gamma_k) dt = \begin{cases} -(\pi/\omega) \sin(\theta_h - \gamma_h) & \text{if } k = h, \\ 0 & \text{if } k \neq h. \end{cases} \quad (2.8)$$

By replacing (2.8) in (2.6), we obtain

$$\begin{aligned} Area_{v-i} &= \left| \sum_{h=1}^H (\pi h) (V_h I_h \sin(\theta_h - \gamma_h)) \right| \\ &= \sum_{h=1}^H \alpha_h |Q_h|, \end{aligned} \quad (2.9)$$

where for each $h = 1, \dots, H$, $Q_h = V_h I_h \sin(\theta_h - \gamma_h)$ denotes reactive power and $\alpha_h = \pi h$ is a *unit-less* constant. From (2.9), the area of the synchronized Lissajous curve in Section 2.5 is the weighted summation of *reactive power* Q_h in all harmonic orders. Here, the reactive power is defined based on the *difference* voltage waveform $v(t)$ and the *difference* current waveform $i(t)$, i.e., with respect to the *virtual* one-port network that we previously defined in Fig. 2.1(c).

It is worth clarifying that the area in (2.9) is *not* equal to reactive power associated with $v(t)$ and $i(t)$. The expression in (2.9) is different from $Q = \sum_{h=1}^H Q_h$. In fact, here we have no reason to calculate Q ; because it can be obtained directly from the raw waveform signals $v(t)$ and $i(t)$. Instead, the above analysis was meant to analytically answer the following question: *is there any physical meaning associated with the area of the synchronized Lissajous curves?*

It is worth adding that, as shown in Section IV-A in [7], there exists another definition for the synchronized Lissajous curve whose area can be interpreted as the weighted summation of the active power that one can define with respect to the voltage waveform in (2.1) and the *derivative* of the current waveform in (2.2).

Inspired by the area characteristic of the synchronized Lissajous curves, we will develop a new event detection method in Section 2.7.

2.6.2 Rotational Angle of the Synchronized Lissajous Curves

Another important feature in the synchronized Lissajous curves is their *rotational angle*; which may indicate the location of the event. For example, consider the synchronized

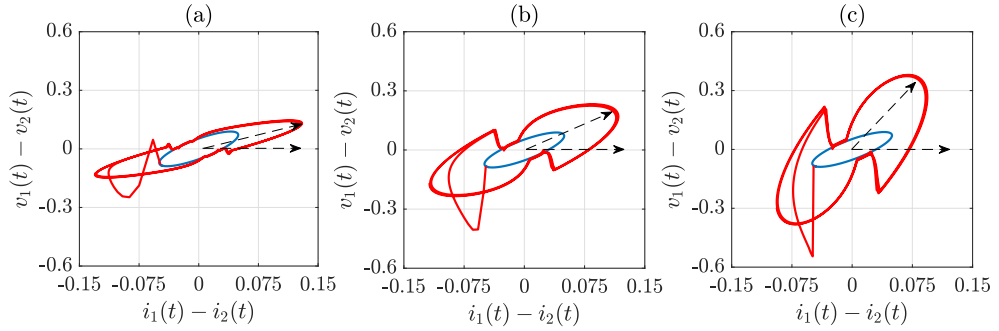


Figure 2.3: The angle (marked with dashed arrows) in the synchronized Lissajous curves during the same event that occurs at three different buses: (a) near WMU 1; (b) in the middle of WMU 1 and WMU 2; (c) near WMU 2.

Lissajous curves in Fig. 2.3. They all represent *the exact same event*, i.e., a high impedance fault. However, the location of the fault is different in these three cases. While the shapes of the curves are similar, there are *rotational differences* among these figures; which are caused due to the different locations of the fault. When the fault occurs near the feeder head, i.e., near WMU 1, the voltage drop between the two WMUs is smaller. This results in a smaller rotational angle, see Fig. 2.3(a). However, when the fault occurs near the end of the feeder, i.e., near WMU 2, the voltage drop between the two WMUs is larger. This results in a larger angle between voltage and current in the synchronized Lissajous curve, see Fig. 2.3(c). Note that, the fault current is almost the same in all the three fault cases in this example.

The *rotational angle* of the synchronized Lissajous curve can be used for *event location identification*. As we learned, if the event occurs near the feeder head, then the rotational angle of the synchronized Lissajous curve is *smaller*. If the event occurs near the end of the feeder, then the angle of the synchronized Lissajous curve is *larger*.

2.6.3 Shape of the Synchronized Lissajous Curves

In addition to the area and angle, the actual shape of each synchronized Lissajous curve can too draw a picture about the state of the power system and the root cause of the disturbance. First, we will discuss the synchronized Lissajous curve during *normal* operating conditions. Next, we will discuss the synchronized Lissajous curve during the event condition.

During a *normal* operating condition, the synchronized waveforms in (2.1) and (2.2) are all purely sinusoidal. Thus, (2.4) and (2.5) include only the *fundamental* components and we have:

$$v(t) = V_1 \cos(\omega t + \theta_1), \quad (2.10)$$

$$i(t) = I_1 \cos(\omega t + \gamma_1). \quad (2.11)$$

Next, we obtain the relationship between waveform $v(t)$ and waveform $i(t)$ by eliminating ωt from equations (2.10) and (2.11). Accordingly, from (2.10), we have:

$$\omega t = \cos^{-1} \left\{ \frac{v(t)}{V_1} \right\} - \theta_1. \quad (2.12)$$

If we substitute (2.12) into (2.11), we can rewrite (2.11) as follows:

$$\begin{aligned} i(t) &= I_1 \cos \left(\cos^{-1} \left\{ \frac{v(t)}{V_1} \right\} - \theta_1 + \gamma_1 \right) \\ &= I_1 \cos \left(\cos^{-1} \left\{ \frac{v(t)}{V_1} \right\} \right) \cos(\theta_1 - \gamma_1) \\ &\quad + I_1 \sin \left(\cos^{-1} \left\{ \frac{v(t)}{V_1} \right\} \right) \sin(\theta_1 - \gamma_1) \\ &= I_1 \cos(\theta_1 - \gamma_1) \frac{v(t)}{V_1} + I_1 \sin(\theta_1 - \gamma_1) \sqrt{1 - \frac{v(t)^2}{V_1^2}}. \end{aligned} \quad (2.13)$$

We square both sides and rearrange the terms to obtain:

$$Av(t)^2 + Bv(t)i(t) + Ci(t)^2 + D = 0, \quad (2.14)$$

where

$$\begin{aligned} A &= 1/V_1^2, & B &= -2 \cos(\theta_1 - \gamma_1)/V_1 I_1, \\ C &= 1/I_1^2, & D &= -\sin^2(\theta_1 - \gamma_1). \end{aligned} \quad (2.15)$$

Equation (2.14) always represents an *ellipse* because

$$B^2 - 4AC < 0. \quad (2.16)$$

Therefore, the synchronized Lissajous curve that is obtained based on $v(t)$ versus $i(t)$ is always an ellipse during *normal* operating conditions.

Once an event occurs, the synchronized Lissajous curve deviates from its initial ellipse shape. The new (i.e., post-event) shape of the synchronized Lissajous curve would depend on the type of the event. To better understand the pre-disturbance and post-disturbance conditions, it is beneficial to plot the synchronized Lissajous curve *separately for each cycle*. Such sequence of the graphical snapshots can be referred to as *cyclic* synchronized Lissajous curve. Fig. 2.4 shows five successive cycles of the synchronized Lissajous curves for three different events, respectively. In all three cases, the cyclic synchronized Lissajous curves are initially an ellipse but then they change to some other shapes.

We can distinguish two broad types of disturbances: *sustained disturbances*; such as high impedance faults and capacitor bank switching; and *temporary disturbances*, such as incipient faults. For the events in Fig. 2.4, the first and the second events are sustained while the third event is only temporary.

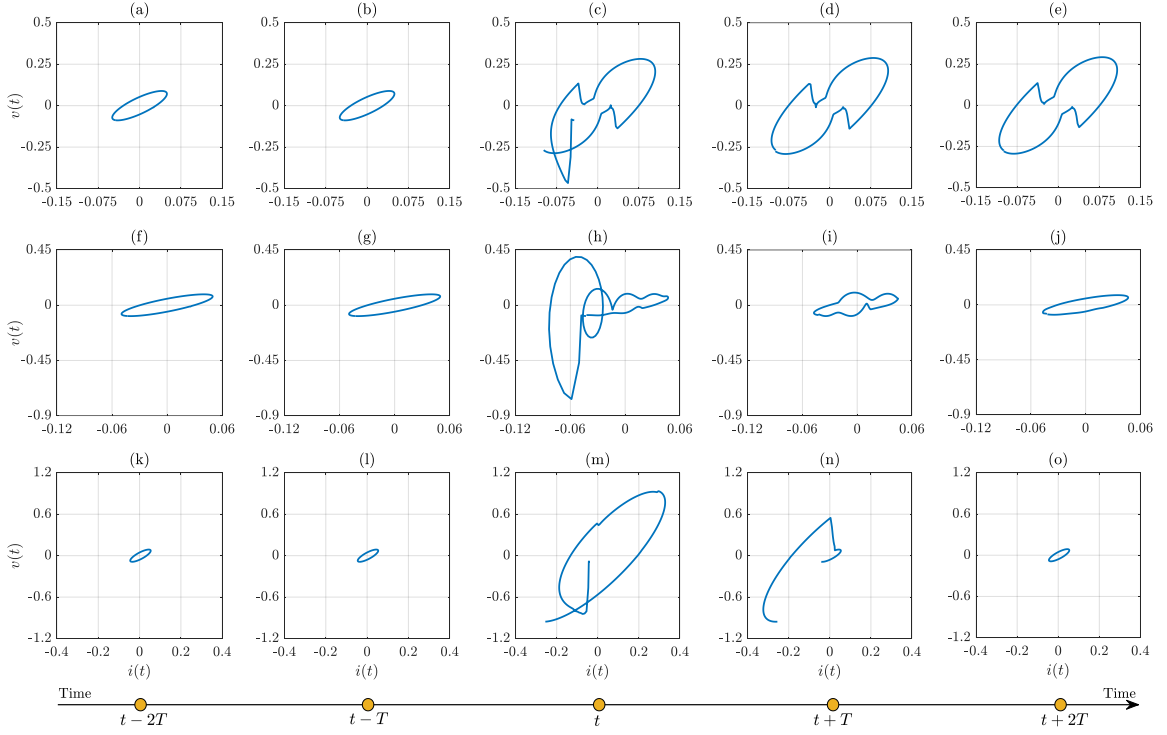


Figure 2.4: Five cycles of synchronized Lissajous curves for three different types of events: (a)-(e) high impedance fault which is a sustained event; (f)-(j) capacitor bank switching which is a sustained event with a major transient component; (k)-(o) incipient fault which is only a short temporary event. T is one cycle period.

As shown in Figs. 2.4(a)-(e), if a high impedance fault occurs, the synchronized Lissajous curve deviates to a very different shape, see Figs. 2.4(c)-(e), compared with the ellipse shape during the normal operating condition, see Figs. 2.4(a)-(b). This is because the fault current in the high impedance fault contains odd order harmonics. As shown in Figs. 2.4(f)-(j), if a capacitor bank switches on, then the synchronized Lissajous curve oscillates for a very short period of time and then it converges to a new (different) ellipse shape, see Figs. 2.4(h)-(i). This happens because of the new transient mode of oscillation of the capacitor bank [2,8]. As shown in Figs. 2.4(k)-(o), if an incipient fault occurs, then the

synchronized Lissajous curve deviates from the shape of an ellipse for the duration of the incipient fault, see Figs. 2.4(m)-(n), then it turns back to the ellipse shape at the normal operating condition, see Fig. 2.4(o). This happens because the incipient fault is self-clearing and has a very short duration.

Motivated by the above examples that showed the shape of the synchronized Lissajous curve can draw a unique picture about the presence and the root cause of the power quality events, we will develop a new event classification method in Section 2.8.

2.7 Event Detection Method

Motivated by the examples and the analysis in Section 2.6.1, our goal in this section is to use the synchronized Lissajous curves as the means to detect power quality events.

2.7.1 Similarity Index

Let us again define the area of the synchronized Lissajous curve at time t over period T of the past cycle as follows:

$$Area(t) = \left| \int_{i(\tau=t-T)}^{i(\tau=t)} v(\tau) di(\tau) \right|. \quad (2.17)$$

During normal operating conditions, there is little to no difference between two successive calculations of the areas in (2.17). However, once an event occurs, such difference suddenly becomes significant. This can help us detect the event. Suppose $Area(t)$ and $Area(t - \Delta t)$ denote the areas of the synchronized Lissajous curves at times t and $t - \Delta t$, where Δt is the

reporting interval of the WMUs, e.g., $\Delta t = 65 \mu\text{sec}$. We define the *similarity index* at time t as follows:

$$\mathcal{S}(t) = 1 - \left| \frac{\text{Area}(t) - \text{Area}(t - \Delta t)}{\max\{\text{Area}(t), \text{Area}(t - \Delta t)\}} \right|. \quad (2.18)$$

If the areas of the two successive synchronized Lissajous curves are almost equal, then $\mathcal{S}(t)$ is close to one. However, if the areas of the two successive synchronized Lissajous curves are considerably different, then $\mathcal{S}(t)$ is close to zero, indicating that a sudden change has occurred in the synchronized Lissajous curve at time t . This means an event has occurred at time t .

2.7.2 Adaptive Detection Threshold

We propose an *adaptive* detection threshold by considering the past similarity indices to minimize the number of false alarms. In this regard, consider a window of time period W immediately before time t , i.e., from time $t - W$ to time $t - \Delta t$. The similarity indices of such window of duration W are

$$\mathcal{S}(t - W), \mathcal{S}(t - W + \Delta t), \dots, \mathcal{S}(t - \Delta t). \quad (2.19)$$

Let us define $M(t)$ and $MAD(t)$ as the *median* and *median absolute deviation* of the similarity indices in (2.19) [36]. We propose to define the adaptive threshold as follows:

$$\mathcal{T}(t) = \alpha \left(M(t) - \eta \text{MAD}(t) \right), \quad (2.20)$$

where α is a number between 0 and 1 to control the sensitivity of the event detection method. A common choice for η is 2.5 [36]. We use the median and median absolute

deviation statistics because they are robust against outliers. We detect an event at time t if the following inequality holds:

$$\mathcal{S}(t) < \mathcal{T}(t). \quad (2.21)$$

Importantly, the detection threshold must be revised after an event is detected. We *discard* the very small similarity index at event time from the next calculation of the adaptive threshold. That is, the similarity index at time t is used in the calculation of the next threshold *only if* time t is not an event time.

2.8 Event Classification Method

Once the power quality event is detected by the proposed method in Section 2.7, we construct a new synchronized Lissajous curve from the moment that the event is detected and for the duration of one cycle. Next, we need to identify the *type* of the detected power quality event based on this one-cycle synchronized Lissajous curve. Therefore, in this section, we propose a novel method based on *image classification* to categorize each detected event into different classes based on the shape of their one-cycle synchronized Lissajous curves. To the best of our knowledge, no prior study has used any variation of the synchronized Lissajous curves to conduct event classification in this context. Furthermore, all the prior studies are focused on making use of only event classification based on measurements from only one power quality or waveform sensor.

First, we will discuss the factors that affect the shape of the synchronized Lissajous curves and why they make the classification problem a highly challenging task. Second, we will convert the detected synchronized Lissajous curves to images so that they can

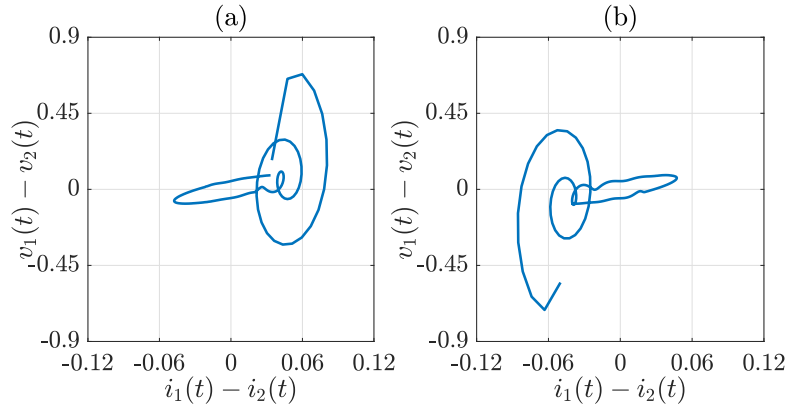


Figure 2.5: The synchronized Lissajous curves during the same event that occurs at two different firing angles: (a) near positive peak; (b) near negative peak.

be classified by using image processing techniques. Third, we will develop an efficient Convolution Neural Network (CNN) to extract features of the synchronized Lissajous images in order to conduct event classification.

2.8.1 Challenging Factors

The shape of the synchronized Lissajous curve depends on not only the type (i.e., the class) of the event, but also other factors such as the angle, the location, and the size of the affected physical components. Therefore, even when we look at *different examples of the exact same class of events*, the shapes of the synchronized Lissajous curves can have considerable differences based on the above various factors. They can make the event classification problem challenging, as we explain next.

Impact of the Event Angle: Consider the synchronized Lissajous curves in Fig. 2.5. They both represent *the exact same disturbance*, which is a capacitor bank switching event. However, the firing angle of the switching action is different in these two cases.

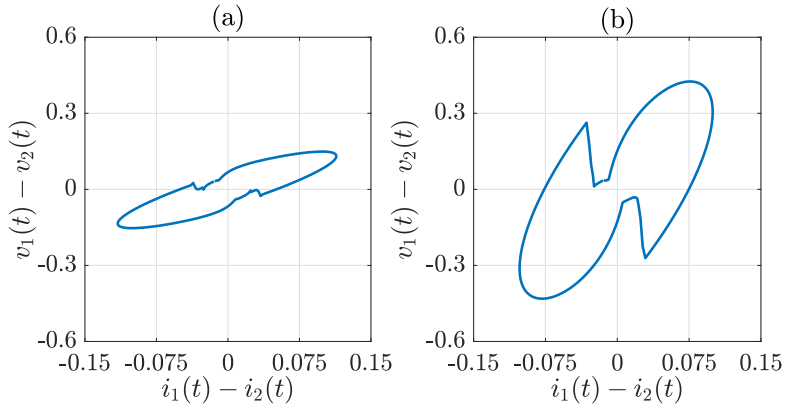


Figure 2.6: The synchronized Lissajous curves during the same event that occurs at two different locations: (a) near WMU 1; (b) near WMU 2.

One switching event occurs near the positive peak of the voltage waveform. The other switching event occurs near the negative peak of the voltage waveform. We can see that the oscillations in the corresponding Lissajous curves start at two different places on the voltage-current plane; making the two curves look differently. In fact, one curve is almost the mirror reflection of the other curve. Therefore, we can conclude that the angle of the event can affect the shape of the synchronized Lissajous curve, thereby creating additional challenges and complications in the event classification problem.

Impact of the Event Location: Next, consider the synchronized Lissajous curves in Fig. 2.6. They represent *the exact same disturbance*, which is a high impedance fault with equal fault impedance. However, the location of the fault is different in these two cases; one is closer to the substation at the beginning of the feeder; while the other one is closer to the end of the feeder. We can see that the shapes of the two curves are somewhat similar; however, there are major *rotational differences* among these curves. If the fault occurs near the beginning of the feeder, i.e., near WMU 1, then the angle between

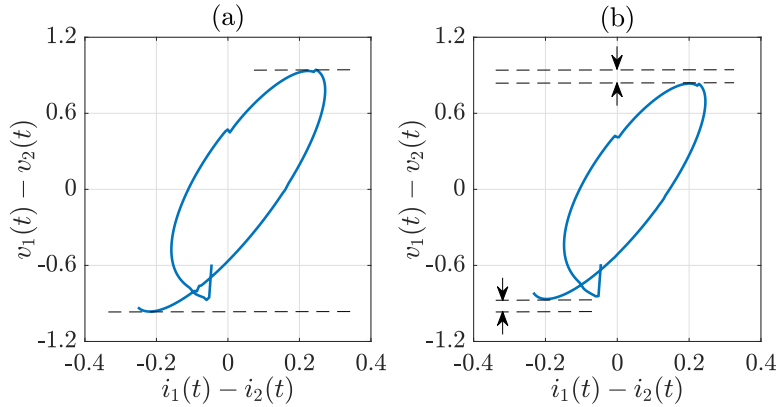


Figure 2.7: The synchronized Lissajous curves during two incipient faults with different fault parameters: (a) lower fault impedance; (b) higher fault impedance.

the voltage difference waveform and the current difference waveform in the synchronized Lissajous curve is *smaller*, see Fig. 2.6(a). However, if the fault occurs near the end of the feeder, i.e., near WMU 2, then the angle between the voltage difference waveform and the current difference waveform in the synchronized Lissajous curve is *larger*, see Fig. 2.6(b). We can conclude that the location of the event can directly affect the shape of the synchronized Lissajous curve, thereby making classification a challenging task.

Impact of other Event Parameters: Finally, consider the synchronized Lissajous curves in Fig. 2.7. They show *the exact same disturbance*, which is an incipient fault. However, the impedance of the fault is different in these two cases. One fault has a smaller impedance. The other fault has a larger impedance. We can see that the shapes of the two curves are almost similar; however, the sizes of the curves are different; which is due to the different fault impedances. If the impedance of the incipient fault is smaller, then the size of the Lissajous curve is larger, see Fig. 2.7(a). Conversely, if the impedance of the incipient fault is larger, then the size of its corresponding Lissajous curve is smaller,

see Fig. 2.7(b). We can conclude that the parameters of an event can highly affect not only the shape but also the size of the synchronized Lissajous curve.

2.8.2 Synchronized Lissajous Curve as Image

The challenges in Section 2.8.1 can be addressed if we treat the synchronized Lissajous curves as *images* and subsequently take advantage of the recent advancements in the field of image processing to solve the event classification problem.

There are multiple reasons why it is beneficial to study a synchronized Lissajous curve as an *image*, as opposed to studying the raw synchronized waveform measurements as *time series*. *First*, graphical images can capture the overall *patterns* in the shape of the synchronized Lissajous curves; while such overall patterns are inherently spread over time in the original time series. For example, there are clear similarities between the two synchronized Lissajous curves in Fig. 2.6. It is clear that one image is almost a *squeezed version* of the other image. Therefore, the two Lissajous images belong to the same class of events. However, such similarity would not be clear if we only look at the raw waveform measurements corresponding to these two events. *Second*, the sequential nature of time series is embedded with many important characteristics, which lays outside of a typical time-domain analysis. Therefore, it is difficult to perform classification in time-domain using the state-of-the-art sequence classification methods. *Third*, deep machine learning methods have shown particularly promising results in recent years in solving image processing problems. Thus, if we present the event classification problem based on synchronized Lissajous curves as an image processing problem, then we benefit from powerful image processing tools.

The synchronized Lissajous curves are converted to synchronized Lissajous images by using various readily available conversion functions in MATLAB and/or Python. For example, one option is to use the combination of functions `getframe` and `frame2im` in MATLAB; see [37, 38].

We will verify the importance of treating synchronized Lissajous curves as images through case studies in Section 2.9.3.

2.8.3 Convolutional Neural Networks

Once the synchronized Lissajous curves are converted to images, one can use various advanced image processing methods to classify the events based on their synchronized Lissajous images. In this thesis, we use Convolutional Neural Networks (CNNs) to classify the detected Lissajous images into multiple classes of events. CNNs are effective deep machine learning techniques that are widely used in image recognition and speech recognition, among other fields [39, 40].

The structure of CNN includes an input layer, a few hidden layers, and an output layer. The input layer takes as input the synchronized Lissajous images of the detected power quality events. The hidden layers consist of the convolutional, batch normalization, activation, max-pooling, dropout, and the fully-connected layers. The convolutional layer is the key layer to extract features. It includes a series of kernel filters. The batch normalization layer normalizes the input, to speed up the training of the CNN. The activation layer implements non-linearity functions to the CNN model, by using functions such as sigmoid, hyperbolic tangent, or rectified linear unit (ReLU). The max-pooling layer performs down-sampling to summarize the extracted features. The dropout layer randomly assigns zero

Table 2.1: The Structure of the Proposed CNN Model

Layer	Layer Type	Activation
1.1	Convolutional	(120,120,60)
1.2	Batch Normalization	(120,120,60)
1.3	ReLU	(120,120,60)
2.1	Convolutional	(120,120,60)
2.2	Batch Normalization	(120,120,60)
2.3	ReLU	(120,120,60)
3.4	Max-Pooling	(60,60,60)
3.1	Convolutional	(60,60,120)
3.2	Batch Normalization	(60,60,120)
3.3	ReLU	(60,60,120)
3.4	Max-Pooling	(30,30,120)
3.5	Dropout	(30,30,120)
4.1	Fully-connected	(1,1,3)
4.2	Softmax	(1,1,3)
4.3	Classification	—

to the input to prevent over-fitting. The fully-connected layer integrates the features from the previous layers to the softmax activation layer to obtain probabilities of the input. The output layer is the classification layer that determines the label of the input image given the probabilities from the previous layer.

Table 2.1 shows the structure of the proposed CNN for event classification based on Lissajous images. It consists of a four-layer architecture, where each architecture includes multiple layers. Since the size of the input Lissajous images is large, a wide kernel filter is used in the first convolutional layer to extract more features from the Lissajous images. The ReLU is used in the activation layers to speed up learning and improve its performance [41]. Softmax is used in the final activation layer to get a probability distribution density for the classes. The proposed CNN classification approach is implemented in MATLAB using its available CNN model [42].

After examining a few different CNN structures, the current structure based on the four-layer CNN was selected due to its desirable performance. This structure is similar to the structure of other CNN-based image classification method in the literature, e.g. see [28–31]. The performance of the proposed classification method is examined in Section 2.9.2 and Section 2.10.2.

It bears mentioning that the size of a synchronized Lissajous image depends on the size of the event. This may affect the results in the classification task. This issue is addressed by *normalizing* each synchronized Lissajous curve with respect to its energy *before* the curves are converted to graphical images.

2.9 Case Studies

In this section, we assess the performance of the proposed event detection and event classification methods. All simulations are done in PSCAD [43] based on the IEEE 33-bus test system. The one line diagram of the simulated test system is shown in Fig. 2.8. Two WMUs are assumed to be installed in the network. WMU 1 is installed at bus 1. WMU 2 is installed at bus 18. Each WMU captures the time-synchronized voltage and current waveforms at its location. To emulate real-world WMU measurements, white Gaussian noise is added to the simulated voltage and current waveform measurements. Unless stated otherwise, we consider a signal-to-noise-ratio (SNR) of 80 dB in both voltage and current waveforms. The nominal system frequency is 60 Hz. Unless stated otherwise, the reporting rate of the WMUs is assumed to be 256 samples per cycle.

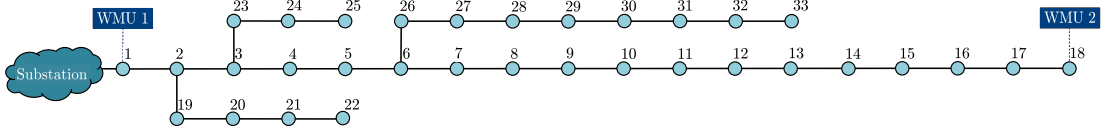


Figure 2.8: The IEEE 33-bus distribution system with two WMUs.

The events that we study in this section are of the type that would typically require examining waveform measurements, i.e., they typically *cannot* be investigated properly by using phasor measurements. For example, we do not consider voltage sags, voltage swells, and interruptions; because they often do not require examining the waveform measurements in order to be detected or even classified. We also consider some events that *could* be captured by phasor measurements; but they are understood much better if one can instead capture the waveform measurements. One such example is capacitor bank switching; where capturing the waveform can further reveal the ringing oscillations as well as potential incipient faults.

The proposed event detection and event classification methods can be used both in post-mortem analysis and in real-time analysis. When it comes to real-time analysis, the steps that are taken are as follows. The proposed event detection method is run continuously to plot and examine the synchronized Lissajous curves to immediately detect any event as soon as it occurs. Once an event is detected, a new synchronized Lissajous curve of the detected event is plotted from the start time of the event and for a duration of one cycle. Most power quality events have a short duration, such as less than one cycle. Even for longer events, the event signature during the first cycle is particularly informative. Thus,

one cycle of the synchronized Lissajous curve is long enough to examine the signature of a power quality event quickly after it is detected. This one-cycle synchronized Lissajous curve is then converted to a synchronized Lissajous image using an image conversion function, as it was previously explained in Section 2.8.2. Finally, the obtained synchronized Lissajous image is used as input to the proposed CNNs, which is already trained when it comes to real-time operation, in order to identify the type of the detected event.

2.9.1 Event Detection Results

We examine the performance of the proposed event detection method on three different classes of disturbances. Here, the sensitivity factor is set to 0.9; and the window duration is set to $W = 133$ msec. The results of event detection for the first class, i.e., the high impedance fault, the second class, i.e., the capacitor bank switching, and the third class, i.e., the incipient fault, are shown in Figs. 2.9(a), (b), and (c), respectively.

In Fig. 2.9(a), the similarity index drops from almost 1 to 0.82 at time $t = 0.50$ sec, indicating that an event occurs at this time, which is the correct event time. The similarity index fluctuates right after the event occurs, for about one cycle, from $t = 0.50$ sec to $t = 0.517$ sec, see the zoomed-in figure. The similarity index goes back to almost 1 after time $t = 0.517$ sec. We can conclude that the event at time $t = 0.50$ sec is the only event that occurs during this one second period; and the event is a sustained event. Thus, the *profile* of the similarity index can help us identify the start time and the end time of each event. These are all useful parameters. For example, when it comes to event classification, the synchronized Lissajous curve from the start time of the event and for the

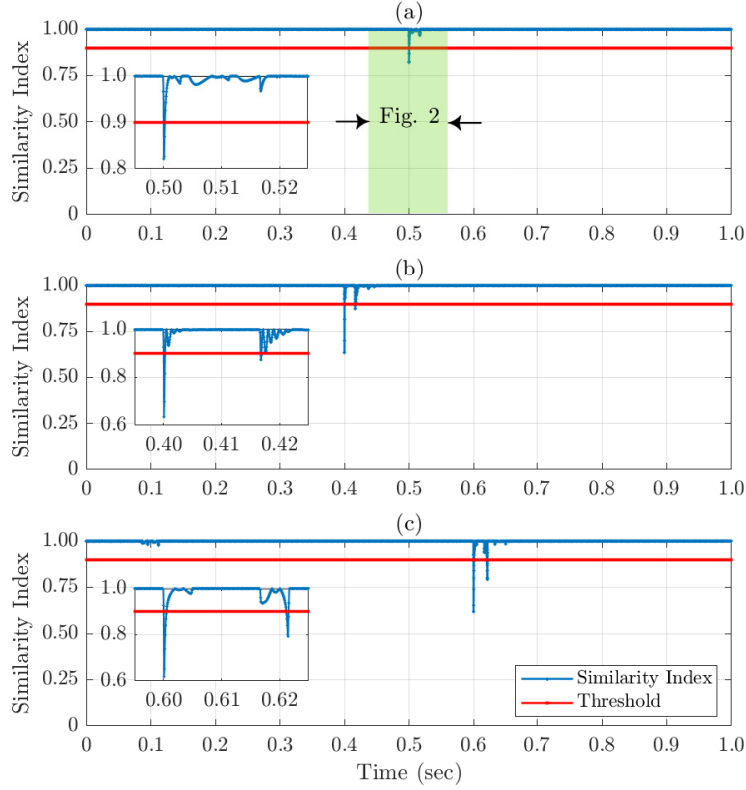


Figure 2.9: The results for event detection, including the similarity index and the adaptive threshold for three example events: (a) the high impedance fault that we saw in Fig. 2.2; (b) a capacitor bank switching; (c) a sub-cycle incipient fault.

duration of one cycle will be converted into an image. For the example in Fig. 2.9(a), we convert the synchronized Lissajous curve from time $t = 0.50$ sec to time $t = 0.517$ sec to an image. The image will be later used for event classification.

In Fig. 2.9(b), the similarity index drops from about 1 to nearly 0.6 at time $t = 0.40$ sec, indicating that an event occurs at this time; which is correct. One cycle later, the similarity index again drops from almost 1 to about 0.9 at time $t = 0.417$ sec, which is lower than the event detection threshold at this time. However, the similarity index rises

to almost 1 after time $t = 0.417$ sec. Thus, the *profile* of the similarity index can help characterize the transient component of the event. It starts at time $t = 0.40$ sec and lasts for about one cycle till $t = 0.417$ sec. This is correct because the capacitor bank switching has a very short transient behaviour. We use the information on the similarity index profile to identify the correct duration of the event signature. In this example, we convert the synchronized Lissajous curve from time $t = 0.40$ sec to time $t = 0.417$ sec to an image. The image will be later used for event classification.

Finally, in Fig. 2.9(c), the profile of the similarity index indicates that an event occurs at time $t = 0.60$ sec, which is correct because the incipient fault is a temporary event that occurs for a short period of time. Hence, the results in Fig. 2.9(c) confirm the effectiveness of the proposed event detection method, even for events with very short duration. In this example, we convert the synchronized Lissajous curve from $t = 0.60$ sec till $t = 0.617$ sec to a synchronized Lissajous image. The image will be later used for event classification.

The above results confirms the effectiveness and the precision of the proposed power quality event detection method.

It bears mentioning that, the similarly index is obtained in an online setting, meaning that we obtain a new similarity index as soon as a new sample becomes available in the waveform measurements. This allows us to immediately detect an event and analyze it as soon as it happens. The computation time of the proposed event detection method is less than 0.3 msec; therefore, it can be used for real-time event detection.

2.9.2 Event Classification Results

In this section, we assess the performance of the proposed event classification method. We first generate a database for the synchronized voltage and current waveforms from two WMUs that occur during 120 events. For each event, we capture one second (60 cycles) of voltage and current waveforms at each WMU. Thus, we collect four synchronized waveforms for each event over 60 cycles. The data for each event includes a few cycles before the event and a few cycles after the event. Each event generates $4 \times 60 \times 256 = 61,440$ samples of data. We generate one synchronized Lissajous image for each event. Thus, the number of synchronized Lissajous images is 120 images. The size for input images of the CNN model is 240×240 . The database consists of 40 high impedance faults, 40 capacitor bank switching, and 40 incipient faults with short arcs, where they are labeled in the following three classes of disturbances: Class I for high impedance faults, Class II for capacitor bank switching, and Class III for incipient faults.

The database is divided into three data sets: training data, validation data, and test data. The training data set includes 70% of the total events which are selected randomly. The validation data set includes 10% of the total events. The test data set includes the remaining 20% of the total events. We use Adam optimization algorithm to train the CNN model, see [44]. The initial learning rate in the training process is set to 1×10^{-4} , which remains constant throughout the training. The maximum number of epochs is set to 100, with the mini-batch size of 32.

The training accuracy of the proposed classification method converges to 100% and the validation accuracy converges to 97%; the figures are not shown here. The small

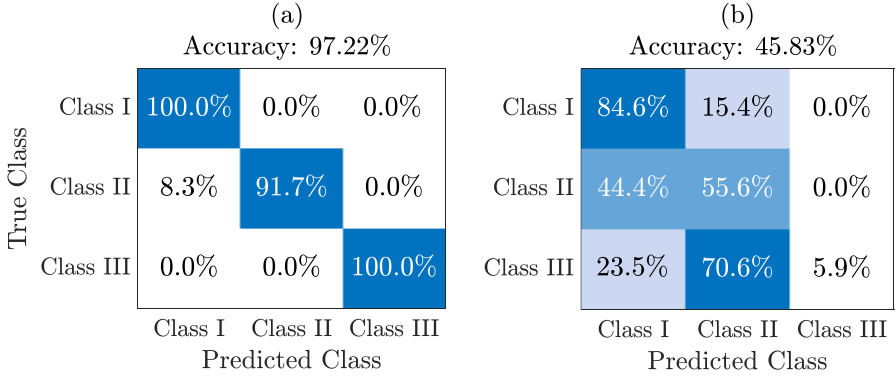


Figure 2.10: Confusion matrix for the test data when we use: (a) the proposed CNN-based image classification method; (b) the competing RNN-based classification method that uses the raw time series measurements.

difference between the two accuracies indicates the generalization capability of the proposed classification method to unseen events.

The confusion matrix for the *test* results for the proposed Lissajous-based CNN model is shown in Fig. 2.10(a). The diagonal entries denote the events that are classified *correctly*. The off-diagonal entries denote the events that are classified *incorrectly*. For each class, the accuracy is at least 91.7%. High impedance faults (Class I) and incipient faults (Class III) are classified better than capacitor bank switching (Class II). The minor shortcoming in the classification of capacitor bank switching is because the image of a capacitor bank switching has some features that also exist in other events. Interestingly, the converse is not true and all the incipient faults are classified correctly. The overall accuracy of the test results is 97.2%, which is very close to the accuracy of the training results, i.e., 100%.

Table 2.2: Performance Metrics corresponding to the Confusion Matrix in Fig. 2.10(a)

Class	Precision	Sensitivity	Specificity	F_1 Score
I	100.0%	92.3%	100.0%	96.0%
II	100.0%	100.0%	100.0%	100.0%
III	94.4%	100.0%	96.8%	97.1%

Next, we use the following various statistical metrics to further evaluate the performance of the proposed classification method: precision, sensitivity (a.k.a. recall), specificity, and F_1 score. Table 2.2 shows each metric for each class. As we can see, the worst-case precision and the worst-case specificity rates of the proposed classification method are 94.4% and 96.8%, respectively, both for Class III (incipient faults). Also, the worse-case sensitivity and the worst-case F_1 score rates are 92.3% and 96.0%, respectively, both for Class I (high impedance faults). These additional metrics further confirm the performance of the proposed event classification method.

Fig. 2.11 shows the Receiver Operating Characteristic (ROC) curve of the proposed event classifier at each class. The Area Under Curve (AUC) for each class is marked in the legend box. The ROC curve is a graph that shows the classifier's ability to distinguish different classes for different probability thresholds. It is obtained by plotting the sensitivity versus the 1-specificity at different threshold settings. As we can see in Fig. 2.11, the AUC is at least 0.971, which indicates that the proposed event classifier can almost perfectly distinguish classes from each other. These results reveal the high performance of the proposed event classification model in correctly classifying events.

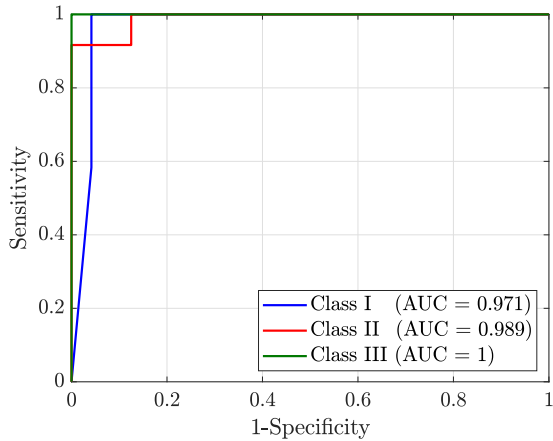


Figure 2.11: The ROC curve of the proposed event classifier at each class. The AUC corresponding to each class is marked inside the legend box. Notice that the ROC curve for Class III appears on the x-axis and the y-axis.

2.9.3 Classification based on Images versus Time Series

As we discussed in Section 2.8, it is highly beneficial to do event classification based on the synchronized Lissajous *images*, as opposed to based on the raw synchronized waveform measurements in time domain. This point is verified here by comparing the proposed CNN classification method that uses synchronized Lissajous images with a recurrent neural network (RNN) classification method that uses the time series of voltage and current waveforms. The latter method is implemented by developing a long short-term memory (LSTM) network to classify the time series of voltage difference waveform in (2.1) and the current difference waveform in (2.2). An LSTM is an RNN that takes time series as input. The hidden layers include two LSTM layers, a dropout layer, a fully connected layer, and a softmax layer. The output layer is the classification layer.

To have a fair comparison, we apply the RNN classification method and our proposed classification method to the *same* training data set and the *same* test data set.

The confusion matrix for the *test* results of the time series classification model is shown in Fig. 2.10(b). The overall accuracy is 45.83%, which is much smaller than the overall accuracy of our Lissajous-based classification method, i.e., 97.2%.

The above results verify the effectiveness of the proposed classification method based on Lissajous images.

From the above results, there are indeed advantages to conduct event classification by using the synchronized Lissajous curves, as opposed to using the raw time-series. The key advantage here is the fact that synchronized Lissajous images can better capture the *fundamental similarities* between the events of the *same type*; that we may sometimes miss if we solely look at the raw measurements as time-series. For example, the *same type* of event may create some characteristics in the raw synchronized waveform measurements that can vary depending on the location of the event or the size of the event. Such variations can sometimes make it difficult for the classification algorithms to realize the fact that the events belong to the *same type*, if we examine the raw measurements as time-series, see [7]. Thus, when possible, it is recommended to use the synchronized Lissajous curves for event classification.

2.9.4 Sensitivity Analysis

Here we investigate the impact of various parameters on the performance of the proposed event classification method through conducting several sensitivity analyses.

First, we investigate the impact of the reporting rate of the WMUs on the performance of the proposed event classification method. We consider four different reporting rates: 32, 64, 128, and 256 samples per cycle. In all four cases, we reach 100% accuracy for

the training data. The accuracy for the test data varies between 95.8% at 32 samples per cycle to 97.2% at 256 samples per cycle. This confirms the effectiveness of the proposed method even at lower measurement reporting rates.

Next, we examine the performance of the proposed event classification method against measurement noise. We consider three different noise levels: 40 dB (very noisy), 60 dB (noisy), and 80 dB (less noisy). The results reveal that the accuracy always reaches 100% for the training data and it is at least 97.2% for the test data. This confirms the robustness of the proposed method even under significant noise levels.

Next, we study the performance of the proposed event classification method against missing data. We assume that we momentarily lose a chunk of measurements; which means we need to construct the synchronized Lissajous curve with missing measurements. We consider three different sizes for the window of data that is missed: 5%, 10% and 15%. The results reveal that the accuracy for the test data varies between 97.2% under 5% missing data to 94.4% under 15% missing data. This further confirms the robustness of the proposed method even under low reliability conditions of the waveform measurements.

2.9.5 Performance Comparison

In this section, we compare the performance of the proposed event classification method with the comparable state-of-the-art method in [31]. Importantly, both the method in this chapter and the method in [31] conduct event classification by using image processing based on CNN. However, the method in [31] does *not* use synchronized Lissajous curves. Instead, it uses a graphical method that is based on the *space-phasor model* (SPM). The purpose of the method in [31] is to characterize voltage waveforms from one WMU to

identify the type of events. In the context of the analysis in this chapter, the method in [31] makes use of the waveform measurements from WMU 1, i.e., the WMU that is located at the upstream of the event. This method does *not* use the synchronized measurements from WMU 2. Thus, similar to most methods in the literature, the method in [31] is inherently *not* designed to take advantage of the synchro-waveforms from multiple WMUs. SPM is a *complex number* and it is calculated as follows [31]:

$$\text{SPM}(t) = \frac{2}{3} \left(v_1^A(t) + \alpha v_1^B(t) + \alpha^2 v_1^C(t) \right), \quad (2.22)$$

where $\alpha = e^{j2\pi/3}$ and $j = \sqrt{-1}$. The superscripts denote the phase. That is, $v_1^A(t)$, $v_1^B(t)$, and $v_1^C(t)$ denote the voltage waveform measurements at WMU 1 on Phase A, Phase B, and Phase C, respectively. The SPM *image* is then generated by plotting the *imaginary* part of $\text{SPM}(t)$ over the *real* part of $\text{SPM}(t)$. The method in [31] applies the CNN-based image classification approach to the SPM images.

To have a fair comparison, we apply the classification method in [31] as well as our proposed classification method to the same database. The dataset in this case study is three-phase; otherwise the SPM formulation in (2.22) cannot be used. For our method, we use the synchronized Lissajous image based on one phase only, i.e., one of the phases that is affected by the event.

Fig. 2.12 shows the confusion matrix when we apply the method in [31] to the test data. As we can see, the overall accuracy is 75%, which is not bad, but considerably less than the overall accuracy of our Lissajous-based classification method at 97%, see Fig. 2.10(a). There are at least two reasons for the better performance of the proposed event classification method. One reason comes from the fact that SPM is not a suitable

		Accuracy: 75.00%		
		Class I	Class II	Class III
True Class	Class I	75.00%	12.50%	12.50%
	Class II	12.5%	87.50%	0.0%
	Class III	0.0%	37.5%	62.5%
		Class I	Class II	Class III
		Predicted Class		

Figure 2.12: Confusion matrix for applying the method in [31]. The results can be compared with those in Fig. 2.10(a).

formulation to represent events that are almost balanced on all three phases. Notice that, by construction, SPM is identical (in form of a circle) for all balanced events. Thus, in general, the use of SPM is only suitable when the focus is on distinguishing balanced events versus unbalanced events. When it comes to distinguishing different types of balanced events, the method in [31] cannot differentiate the events because of their very similar shapes in the SPM images.

Another reason for the better performance of the proposed method is that it uses *both* voltage waveforms and current waveforms. This is an inherent property of the Lissajous graph. There would be no synchronized Lissajous curve without using the synchronized current measurements. However, the method in [31] does not use the current waveform measurements.

In summary, the use of the proposed synchronized Lissajous images has fundamental advantages over the use of SPM images; even though both method ultimately involve image processing for the purpose of event classification.

2.10 Experimental Results

While the case studies in Section 2.9 were extensive and insightful, they were all based on computer simulations. To complement the results in Section 2.9, in this section, we provide additional case studies that are based on *experimental* results.

2.10.1 Real-World Field Measurements

In this section, we evaluate the performance of the proposed event detection method by using real-world synchro-waveform measurements from the publically available data set on the EPRI/DoE (Electric Power Research Institute/Department of Energy) website [45]. This data set contains three-phase voltage waveform and three-phase current waveforms for about 300 power quality disturbances. The waveforms are recorded using various power quality sensors, therefore, they have different reporting rate, ranging from 16 samples per cycle up to 128 samples per cycle. Importantly, the vast majority of the waveform measurements in the EPRI/DoE data set are *not* synchro-waveforms; they are rather individual unsynchronized waveform measurements. However, there *are* very few cases where *synchronized* waveform measurements were obtained by two waveform sensors for the *same* event.

We use two examples of such real-world synchro-waveform measurements. The first example includes the synchronized measurements from two WMUs at Record Numbers 2892 and 2893. This event is related to a line tripping that happened during a lightning. The second example includes the synchronized measurements from two WMUs at Record Numbers 2786 and 2787. This event is related to a fault that happened during a major

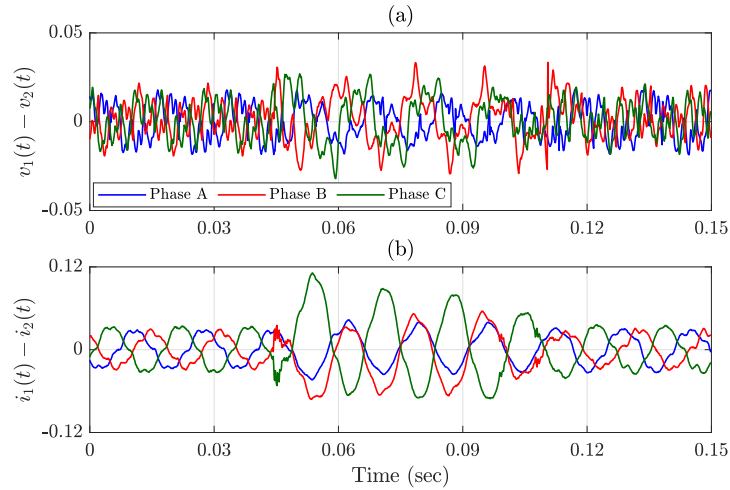


Figure 2.13: An example for real-world synchronized waveform measurements during an event: (a) three-phase voltage difference waveform; (b) three-phase current difference waveform. The two sets of three-phase waveforms are from the waveform records 2892 and 2893 in the EPRI/DoE database [45].

storm. As the starting point for our analysis, we used the above raw waveform measurements and obtained the *difference waveforms* as in (2.1) and (2.2). Given that the measurements in [45] are three-phase, we obtained the difference waveforms for each phase. Figs. 2.13 and 2.14 show the obtained difference waveforms in the first and second examples, respectively.

Performance of Event Detection

Figs. 2.15(a) and (b) show the profile of the similarity index for the real-world synchronized waveform measurements in Figs. 2.13 and 2.14, respectively. Only one phase is shown here. The similarity index profile in Fig. 2.15(a) indicates that the event occurs at time $t = 0.045$ sec, which is indeed correct. The similarity index then fluctuates right after the event for about five cycles, from $t = 0.045$ sec to $t = 0.12$ sec. The similarity index

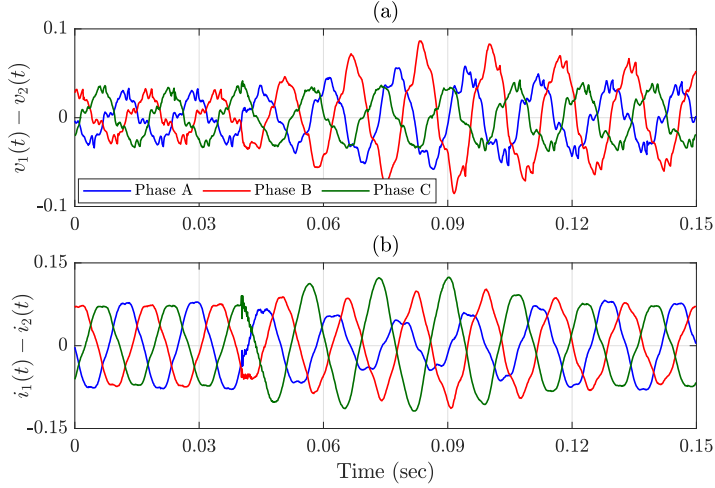


Figure 2.14: Another example for real-world synchronized waveform measurements during an event: (a) three-phase voltage difference waveform; (b) three-phase current difference waveform. The two sets of three-phase waveforms are from the waveform records 2787 and 2786 in the EPRI/DoE database [45].

goes back to almost 1 after time $t = 0.12$ sec. The similarity index profile in Fig. 2.15(b) indicates that an event occurs at time $t = 0.04$ sec, which is correct. Hence, the results in Figs. 2.15(a) and (b) further confirm the accuracy of the proposed event detection method, including for real-world waveform measurements.

Comparison with Another Graphical Tool

Next, we compare the proposed method that is based on using synchronized Lissajous curves with another graphical method that was proposed in [31]. The graphical method in [31] is based on the SPM from one WMU, as we discussed in Section 2.9.5.

From (2.22), it is clear that the method in [31] does *not* use the current waveforms, as opposed to the method in this chapter that uses *both* voltage and current waveforms. This limitation was *not* an issue in [31]; because the primary purpose of the study in [31]

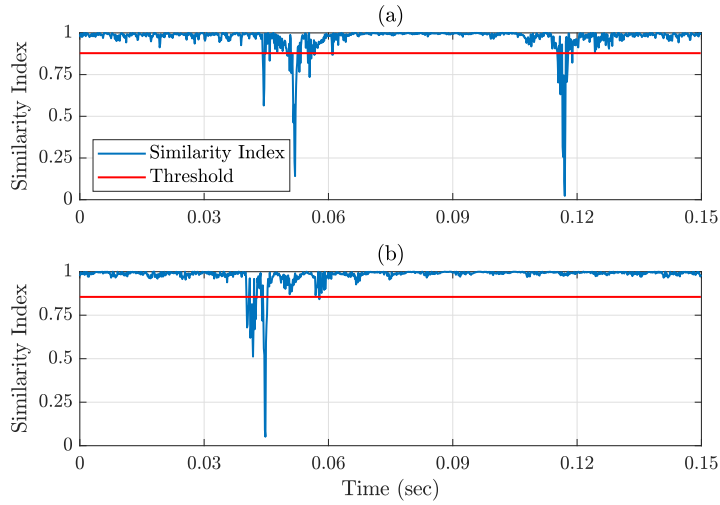


Figure 2.15: The results of event detection applied to the real-world synchronized waveform measurements, including the similarity index and the adaptive threshold: (a) Phase B of the difference waveform measurements in Fig. 2.13; (b) Phase C of the difference waveform measurements in Fig. 2.14.

was to classify events based on whether they involve disturbances on *one phase*, on *two phases*, or on *three phases*. Because of such focus on the analysis of unbalance, the method in [31] did not need to reveal all the characteristics of the event on each phase. However, this is needed for the type of study that is done in this chapter, i.e., to examine the detailed shape of the event on every phase, even in a single-phase system. Clearly, if we focus on one phase only, the method in [31] is no longer applicable; because SPM is all about the *relative* shape of the voltage waveforms across the three phases.

Figs. 2.16 and 2.17 show nine successive cycles of the synchronized Lissajous images and the SPM images corresponding to the real-world event in Fig. 2.13. As we can see, the shape of the SPM image in the nine cycles in Fig. 2.17 are more or less the same, making it difficult to identify the detailed characteristics of the event. However, the

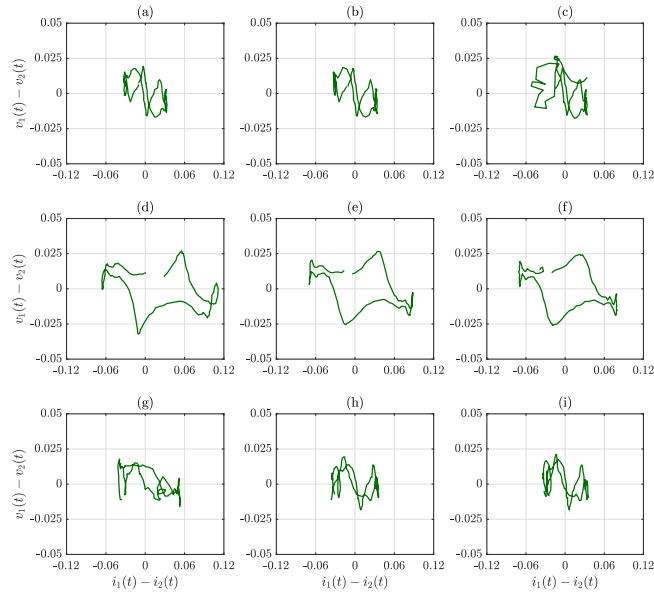


Figure 2.16: Nine cycles of the synchronized Lissajous curves on Phase C for the real-world waveform event in Fig. 2.13.

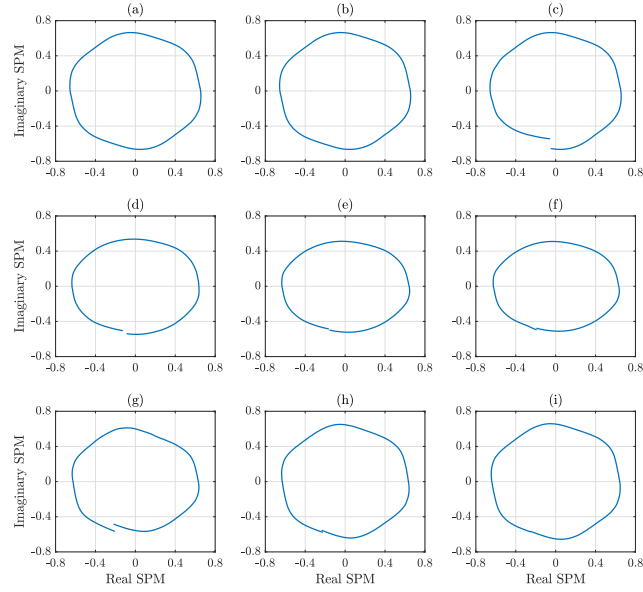


Figure 2.17: Nine cycles of the SPM curves [31] for the same real-world waveform event that was discussed in Fig. 2.13. Compare the graphs with those in Fig. 2.16.

synchronized Lissajous images in Fig. 2.16 do take *very different shapes* when the event occurs, e.g., see the image at cycle 4 in Fig. 2.16(d), and compare it with the image at cycle 3 in Fig. 2.16(c) and the image at cycle 7 in Fig. 2.16(g), i.e., before and after the event. Notice that the new shape of the synchronized Lissajous curve remains for a total of about three cycles, from cycle 4 to cycle 6, see Figs. 2.16(d)-(f). Thus, the synchronized Lissajous images draw a unique and more comprehensive picture about the presence and the characteristics of the event, much more than the SPM images.

Therefore, although both the synchronized Lissajous images and SPM images are regular images, the shape of the synchronized Lissajous images provide us with further, and more insightful information about the characteristics of the event.

We can make similar observations also for the second example of the real-world synchronized waveform measurements in Fig. 2.14. Figs. 2.18 and 2.19 show nine successive cycles of the synchronized Lissajous images and SPM images corresponding to this example. Comparing the images in Figs. 2.18 and 2.19, we can again see that the synchronized Lissajous images provide more information and *more distinction* about the event, compared to the SPM images. This further confirms the effectiveness of the proposed graphical tool for event monitoring.

2.10.2 Hardware-in-the-Loop Testing

The real-world field measurements in Section 2.10.1 were suitable for the analysis of the proposed event detection method. They were also useful to highlight the importance of using the proposed synchronized Lissajous curve, compared to other graphical tools in

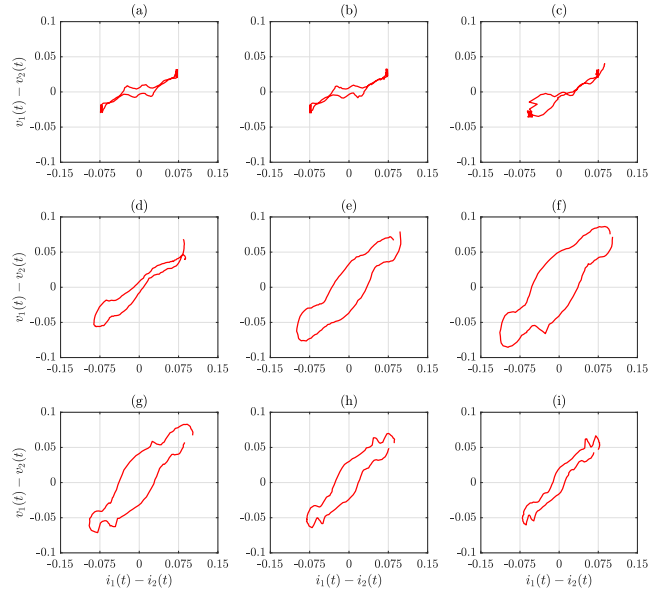


Figure 2.18: Nine cycles of the synchronized Lissajous curves on Phase B for the real-world waveform event in Fig. 2.14.

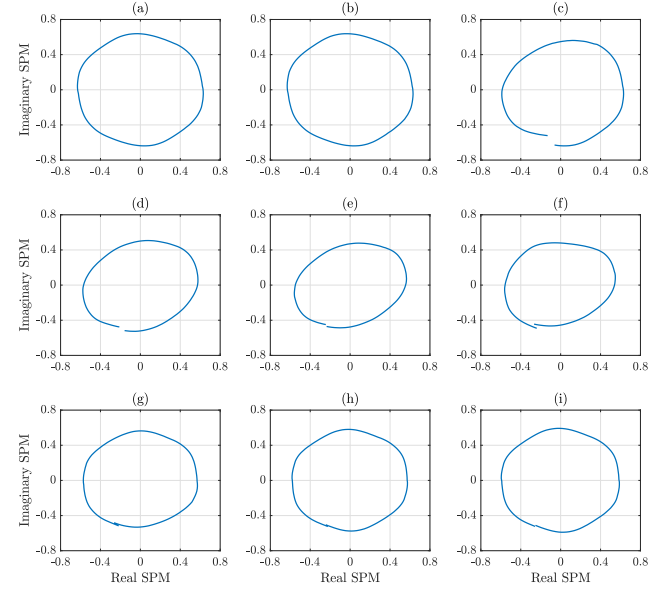


Figure 2.19: Nine cycles of the SPM curves [31] for the same real-world waveform event that was discussed in Fig. 2.14. Compare the graphs with those in Fig. 2.18.

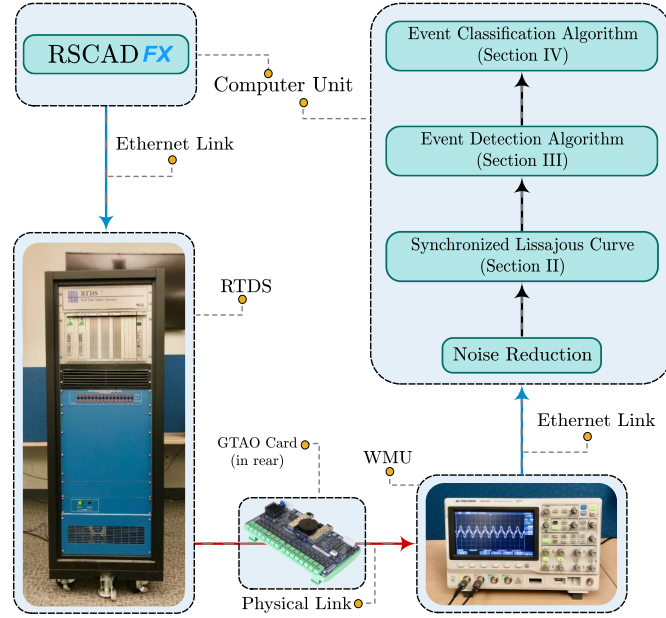


Figure 2.20: The architecture of the implemented HIL testing experiments.

the literature, such as in [31]. However, such field measurements are not sufficient to train and to test the proposed event classification method. Therefore, in this section, we conduct Hardware-in-the-Loop (HIL) testing so that we can examine the event classification method.

HIL testing is a technique for testing an external hardware in real-time simulations. For the purpose of this study, we used HIL testing to capture real-time waveform measurements by using an *external hardware* for the sensor device. Our HIL testing setup consists of the following components, as shown in Fig. 2.20: 1) a Real Time Digital Simulator (RTDS) that simulates a power distribution network in real-time [46]. Importantly, RTDS is the industry standard HIL testing equipment that is widely used by utilities; 2) a multi-channel BK Precision 2569 Series Digital Storage and Mixed Signal Oscilloscope

that serves as the external WMU hardware; 3) a computer unit that runs the simulations and also receives and stores the real-time measurements; 4) the RSCAD software that is used for running the simulations on the RTDS [47]; and 5) the algorithmic software that we developed in MATLAB to collect the raw waveform measurements from the external WMU hardware, conduct noise reduction, obtain the synchronized Lissajous curves, obtain the corresponding images, and conduct event classification according to the proposed method.

The power distribution network that is simulated in RSCAD inside the RTDS is the same IEEE 33-bus distribution feeder that we previously saw in Fig. 2.8. The voltage waveform and the current waveform from bus 1 and bus 18 are extracted from RTDS to feed into the ports of a GTAO (GIGA-Transceiver Analog Output) Card to generate external Analog waveforms. Such Analog waveforms are then supplied as inputs to the channels of the external WMU hardware. The differential synchro-waveforms are then captured by the external WMU hardware and subsequently sent to a computer server through an Ethernet connection, i.e., a Local Area Network (LAN) cable. The obtained measurements are then used to evaluate the performance of our proposed event classification method.

The distribution of different classes, the assumptions, and the choices of the training parameters remain the same as in Section 2.9.2. Since the waveform measurements are done by using an actual external hardware sensor, the raw measurements are *noisy*. Thus, before we can use the waveform measurements, we need to do *noise reduction*. We do so by using a lowpass filter to remove the high frequency noises from the raw measurements.

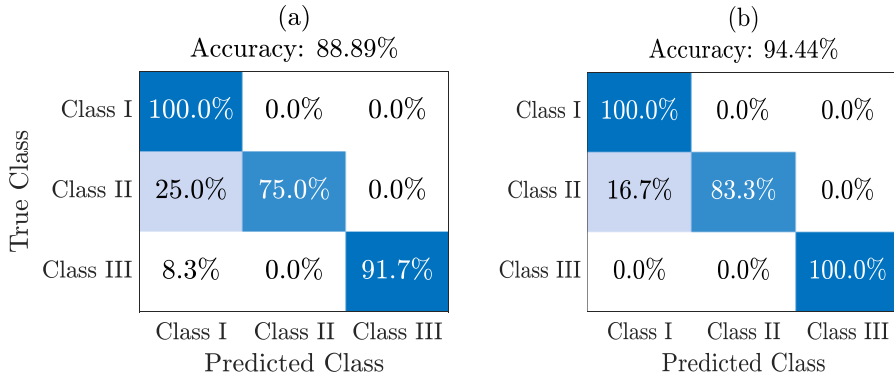


Figure 2.21: Confusion matrix for applying the proposed event classification method to the test data in HIL testing: (a) without initial noise reduction; (b) with initial noise reduction.

Figs. 2.21(a) and (b) show the confusion matrix for the test data, without and with initial noise reduction, respectively. As we can see, the proposed model is able to correctly classify most of the unseen events in the HIL tests. The overall accuracy of the test results is 88.9% for the case without initial noise reduction, see Fig. 2.21(a), and 94.4% for the case with initial noise reduction, see Fig. 2.21(b). The results further confirm the effectiveness of the proposed event classification method.

2.11 Conclusions of the Chapter

A new data-driven situational awareness framework is proposed in power distribution systems based on the analysis of synchro-waveform measurements that are provided by WMUs. The new framework is built upon a fundamentally new concept, called the synchronized Lissajous curve, where we plot the difference of two synchronized voltage waveforms versus the difference of two synchronized current waveforms. The synchronized Lissajous curves provide insight about the operation of the power system during power quality events,

thereby improving our knowledge about the root cause and the characteristics of various events. The characteristics of the synchronized Lissajous curves, namely *area*, *rotational angle*, and *shape*, are studied both analytically and through examples. It is shown that, the *area* of the synchronized Lissajous curves resembles a notion of reactive power. Therefore, the synchronized Lissajous curves provide *complementary* insight about the WMU measurements. The *rotational angle* of the synchronized Lissajous curves further provides information about the location of the event. Finally, the *shape* of the synchronized Lissajous curves indicate the type of the event. We used the changes in areas of two successive synchronized Lissajous curve as the metric to detect an event. The proposed detection method is able to accurately detect events and also identify the start time and the end time of each event. We also used the images of the synchronized Lissajous curves to classify the detected events. In this regard, we developed a CNN-based image classification method. The proposed classification method is able to classify power quality events with high accuracy, even at very low measurement reporting rate, under missing data, and under very noisy environment.

Chapter 3

Event Location Identification

In this chapter, we propose a new method to *identify* the location of transient events, including incipient faults, in power distribution systems, by using synchro-waveform measurements from WMUs. Given such data, the proposed method identifies the bus number where the event occurred. It consists of three steps. The first step is to characterize the oscillatory modes of the transient components of all the captured synchronized voltage and current waveforms from all WMUs; namely their frequency, damping rate, magnitude, and angle, by conducting a multi-signal modal analysis. The second step is to construct a circuit model for the underlying distribution feeder at the identified dominant mode(s) of the transient event. The final step is to identify the location of the transient event based on certain forward and backward analyses of the constructed circuit model. The proposed method requires installing as few as only two WMUs, one at the beginning of the feeder and one at the end of the feeder. It can also utilize several synchronized waveform measurements

when several WMUs are available. The performance of the proposed event location identification method is assessed on a standard test system; for a wide range of events, such as sub-cycle incipient faults, multi-cycle incipient faults, permanent faults, as well as benign yet informative events such as capacitor bank switching.

3.1 Summary of Technical Contributions

The main contributions of the work in this chapter are as follows:

1. On one hand, this chapter introduces a new use case for WMUs, as an emerging smart grid sensor technology. On the other hand, this chapter addresses a challenging problem in power distribution systems. Here, our focus is specifically on transient events; which are *inherently very short in duration*. Identifying the location of such short events is very challenging. Nevertheless, the proposed method can identify the correct location in most cases.
2. The proposed method is applicable to different types of transient events, such as sub-cycle and multi-cycle incipient faults. This is a direct result of using the synchronized waveform measurements, as opposed to using synchronized phasor measurements as in other methods, e.g., in [48], which cannot suitably observe transient events.
3. The proposed method takes advantage of the availability of synchronized waveform measurements from multiple WMUs; as opposed to the common approach in the existing incipient fault location methods that work based on measurements from one sensor. Furthermore, unlike the existing incipient fault location methods, such as

in [49], the proposed method considers the fact that there are loads between the sensor location and the fault location.

4. The proposed method works for two fundamentally different types of transient events:
the events that are static in nature, such as in case of arcs in incipient faults that are resistive and do *not* create any new oscillation mode; as well as the events that are dynamic in nature, such as in case of capacitor bank switching that is reactivate and create new oscillation mode(s) in the system.
5. The proposed method is also able to pin-point the correct location of *permanent events*, such as permanent faults and capacitor bank switching. The advantage here is that the proposed method is prompt because there is no need to wait until the system reaches steady-state conditions before we can identify the location of the event.

3.2 Related Literature

The majority of the existing methods in the area of event and fault location identification use measurements that are meant for steady-state analysis, such as phasor measurements, which are suitable only to analyze permanent events and faults, e.g., see the impedance-based methods in [50–52] and the wide area-based methods in [48, 53, 54]. As we saw in the example in Section 1.2 in Chapter 1, phasor measurements cannot accurately capture short transient events, such as incipient faults.

There is a limited literature on incipient fault location identification using waveform measurements, e.g., in [49, 55–61]. The methods in these papers use waveform mea-

surements from one sensor to estimate the *distance* between the fault location and the sensor location. Their accuracy decreases when there are loads between the fault location and the sensor location; which is often the case in power distribution feeders. This issue can be alleviated by using a load compensation strategy [59]. Also, they may not work well with locating sub-cycle incipient faults; because of their extremely short duration.

There are also a few studies that address location identification for benign events, such as capacitor bank switching, using waveform measurements from one sensor, e.g., see [62,63], where the proposed methods are distance-based methods. Further, as we learned in Section 2.6 in Chapter 2, the new graphical tool of the synchronized Lissajous curve can provide us some insight about the location of events using synchro-waveform measurements from as few as only two WMUs [7,9,10].

3.3 Modal Analysis of Captured Transient Synchronized Waveform Measurements

The starting point in our proposed methodology is to characterize the *transient component* of the synchronized waveform measurements during an event. Here, we assume that the event *is already detected and classified*, by using any event detection and classification methods, such as those in [9,17,24,27,64], and particularly the methods that we proposed in Chapter 2 of this thesis.

Figs. 3.1 and 3.2 show two examples of WMU measurements that are captured during two different types of transient events. The transient components are marked with green boxes. The event in Fig. 3.1 is an *incipient fault*. The event in Fig. 3.2 is a *capacitor*

bank switching. In both events, the duration of the transient part is *one cycle or less*.

We propose to characterize the transient component of the event waveforms by conducting *modal analysis*. In this regard, the transient component of the waveforms is characterized as one or more *oscillation modes*. Each oscillation mode itself is characterized based on the following parameters:

- Frequency,
- Damping Rate,
- Magnitude,
- Phase Angle.

Modal analysis can be done in different ways, such as by using Prony method [65], matrix pencil method [66], or the methods based on rotational invariance techniques [67].

3.3.1 Single-Signal vs Multi-Signal Modal Analysis

Regardless of which method is used, modal analysis can be done in two different ways: *single-signal* and *multi-signal*. There is a considerable difference between these two approaches in the context of this chapter, as we explain next.

In *single-signal* modal analysis, each individual waveform is analyzed *independently*; thus, the modes are calculated for each waveform *separately*. For instance, for the cases in Figs. 3.1 and 3.2, where we have two WMUs, we need to do a separate modal analysis for each of the following four signals within the marked green boxes: voltage waveform at WMU 1, current waveform at WMU 1, voltage waveform at WMU 2, and current

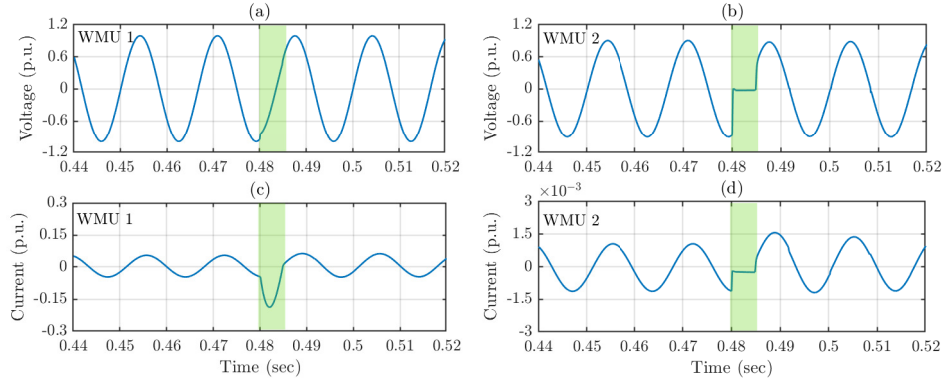


Figure 3.1: Synchronized waveform measurements during an incipient fault: (a)-(c) voltage and current waveforms that are captured by WMU 1; (b)-(d) voltage and current waveforms that are captured by WMU 2. The green rectangle marks the transient component that was the subject of modal analysis.

Table 3.1: Dominant Mode of the Transient Event in Fig. 3.1, Obtained by Using the Multi-Signal Modal Analysis

WMU	Signal	Frequency (Hz)	Damping Rate (Hz)	Magnitude (p.u.)	Phase Angle (deg.)
1	Voltage	60.00	0.00	0.96	0.00
	Current			0.32	-35.56
2	Voltage			~ 0.00	-17.94
	Current			~ 0.00	-32.94

waveform at WMU 2. In theory, the frequency should be the same for all the four signals and the damping rate should also be the same for all the four signals; because waveform signals, regardless of where on the circuit they are captured, oscillate at the same frequency and the same damping rate [68].

However, in practice, the results are often slightly different for each signal. This is due to numerical issues, noise in measurements, slight waveform distortions, etc. For example, the fundamental frequency can be obtained as 60.3 Hz from one waveform and 59.9 Hz from another waveform. Such discrepancy can be problematic for the purpose of event location identification that we will discuss in Section 3.5.

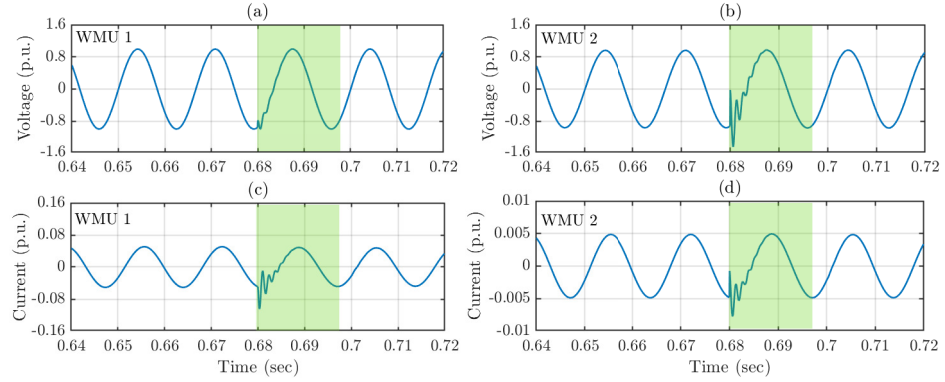


Figure 3.2: Synchronized waveform measurements during a capacitor switching: (a)-(c) voltage and current waveforms that are captured by WMU 1; (b)-(d) voltage and current waveforms that are captured by WMU 2. The green rectangle marks the transient component that was the subject of modal analysis.

Table 3.2: Dominant Modes of the Transient Event in Fig. 3.2, Obtained by Using the Multi-Signal Modal Analysis

WMU Signal	Frequency (Hz)	Damping Rate (Hz)	Magnitude (p.u.)	Phase Angle (deg.)
1	Voltage			0.98 / 0.20 0.00 / 0.00
	Current	60.00 / 747.72	0.00 / -624.30	0.04 / 0.06 -25.19 / 82.43
2	Voltage			0.96 / 0.92 -0.49 / -1.07
	Current			0.004 / 0.004 -25.96 / -3.23

* The two most dominant modes are separated with a slash.

The above issue can be resolved by using *multi-signal* modal analysis. In this approach, the transient modes are obtained for all waveforms in the same unified estimation analysis. Hence, the frequency is the same for all the four signals. Likewise, the damping rate is the same for all the four signals.

The dominant mode of the incipient fault in Fig. 3.1 is shown in Table 3.1. The dominant modes of the capacitor bank switching event in Fig. 3.2 are shown in Table 3.2. The results in Tables 3.1 and 3.2 are obtained by using the multi-signal Prony method.

In Tables 3.1 and 3.2, the frequency of the dominant mode(s) is the same for all

the four waveform signals; and similarly the damping rate of the dominant mode(s) is the same for all the four waveform signals. The reference for the phase angles is with respect to phase angle of the voltage waveform at WMU 1. Also, notice that, the modal analysis in Table 3.1 includes one dominant mode while the modal analysis in Table 3.2 includes two dominant modes. Next, we discuss the reason for this key difference between the two types of transient events.

3.3.2 Selecting the Time Window and the Number of Modes

There are two basic parameters in any modal analysis: the time window and the number of the modes. The choices of these parameters and their required accuracy depend on the type and the duration of the event. For example, the temporary event in Fig. 3.1 has a short duration; therefore, it requires a small window size. As another example, the permanent event in Fig. 3.2 has a much longer duration; therefore, it requires a longer window size; and it is less sensitive to the exact size of the time window for the purpose of the modal analysis. In this chapter, we obtain the start time of an event by using the event detection method in Section 2.7 in Chapter 2, see [9,10]; which is proven to accurately obtain the event start time. The event detection method in Chapter 2 also provides us with the end time for an event; although, obtaining the end time of an event is usually more challenging. The window size for the purpose of the modal analysis should be equal or less than the time period between the start time and the end time of the event. For example, if we apply the event detection method in Chapter 2 on the waveforms in Fig. 3.1, the start time of the event is obtained at $t = 480$ msec, and the end time of the event is obtained at $t = 485$ msec. Therefore, time window for modal analysis is set to $485 - 480 = 5$ msec or

less, see the lengths of the green rectangles in Fig. 3.1; to make sure that we do not include the part of the signal that is not related to the event.

In this study, we also use an exhaustive search to further refine the window size and also to select the number of modes in the multi-signal modal analysis. For each event, we seek to select these two parameters such that we minimize the *root mean square error* (RMSE) in modal analysis. This is done by conducting the modal analysis for different time windows that are less than the initial time window that we obtain from the method in Section 2.7 in Chapter 2 and also for different number of modes. The RMSE is obtained in each case; and the minimum RMSE is identified and the time window and the number of modes are set accordingly.

3.3.3 Selecting the Dominant Transient Event Mode(s)

Depending on the nature of the transient event, it may only magnify an *existing mode*; or it may create *new modes*. The former occurred in the case of the incipient fault in Fig. 3.1. The latter occurred in the case of the capacitor switching in Fig. 3.2.

The incipient fault in Fig. 3.1 was due to a momentary arcing in the system. The arc added a new resistance to the circuit; therefore, it did *not* create any new dynamic mode. As a result, the only dominant mode during the transient event in Fig. 3.1 is the fundamental mode, i.e., at 60 Hz, as we saw in Table 3.1.

The situation was different for the capacitor bank switching event in Fig. 3.2. In this case, the event caused a change in the dynamic components of the system; therefore, it created a new dynamic mode of oscillation. As a result, we captured two dominant modes during this transient event. One is the fundamental mode, i.e., at 60 Hz, and the other one

is a high-frequency mode, at 748 Hz, as we saw in Table 3.2.

We can use *mode reduction* to decide which dominant mode(s) should be kept for the purpose of our event analysis in Section 3.4. One Option is to keep the modes with high magnitude. Another option is to check the energy of each mode, and keep the modes with high energy.

3.3.4 Comparison with Time Domain Analysis

It is insightful to compare some key aspects of our analysis, which is done in modal phasor domain, versus an analysis that could be done in time domain by using the raw waveform measurements. First, the phasor analysis in this chapter allows us to focus on the dominant event mode of the signals; which makes our analysis more robust to noises, compared to conducting the analysis on the raw time-series of the waveform measurements. Second, the phasor representation is easier to work with when it comes to solving the circuit. Note that, our method requires conducting the forward analysis and the backward analysis on the circuit model of the underlying power distribution feeder. If we use time representations; then we would have to deal with solving several differential equations and we would have to also consider an *initial solution*; all of which would unnecessarily complicate the analysis. Third, we use phasor representation only for the exact duration of the event, which ranges from less than a cycle to a few cycles. Thus, we inherently focus on the specific short interval of the *transient* component of the event. Fourth, the proposed method uses the Prony method to capture the dominant event modes in the waveform signals, as opposed to using the fast Fourier transformation. Therefore, although our analysis is done in phasor domain, we do *not* lose the information about the event,

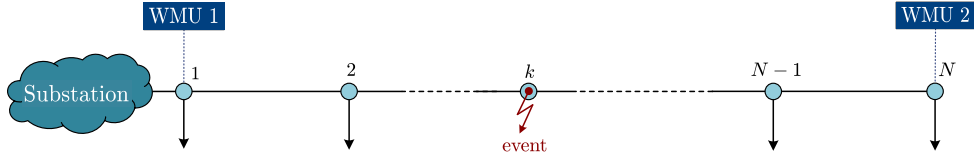


Figure 3.3: A power distribution feeder that is equipped with two WMUs. An event occurs somewhere along the feeder at *unknown* bus k .

unlike in the case of the phasor measurements in PMUs. In fact, we fully capture the transient behavior of the event, even if it is only a short period of time.

3.4 Constructing the Feeder Model at the Dominant Transient Modes

Given the dominant modes of the synchronized waveform measurements during the transient event, the next step is to construct the feeder circuit model at those dominant modes. In this regard, consider a power distribution feeder, as in Fig. 3.3, and let us focus on any arbitrary line segment in this feeder, such as the one that is shown in Fig. 3.4(a).

Let R and L denote the resistance and inductance of the line segment.

Suppose a transient event occurs at time $t = 0$ at a bus on the distribution feeder. Suppose the location of the event is *unknown*. The voltage waveform at bus m is denoted by $v_m(t)$; the voltage waveform at bus n is denoted by $v_n(t)$; and the current waveform on the line segment is denoted by $i_m(t)$, where t indicates the timestamp immediately after the event occurs.

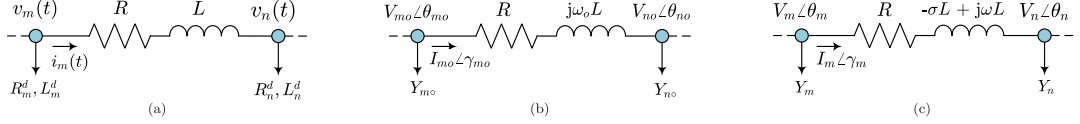


Figure 3.4: Analysis of voltage and current waveforms at a line segment immediately after the transient event occurs: (a) the circuit model in time domain; (b) the circuit model under the *fundamental mode*; (c) the circuit model under the *new transient mode* that might be created by the event.

As mentioned in Section 3.3.3, the transient event may either only magnify the existing fundamental mode; or it may create new dominant modes. Next, we discuss how to model the circuit of the distribution feeder under both circumstances.

3.4.1 Case I: Transient Event Does not Create a New Mode

If the transient event does *not* create any new oscillation mode, e.g., as in Fig. 3.1, then the only dominant mode during the transient event is the fundamental mode, as in Table 3.1.

Let f_\circ and $\omega_\circ = 2\pi f_\circ$ denote the frequency and rotational frequency of the fundamental mode. Also, let $V_{m\circ}$ and $\theta_{m\circ}$ denote the magnitude and phase angle of $v_m(t)$ at the fundamental mode; $V_{n\circ}$ and $\theta_{n\circ}$ denote the magnitude and phase angle of $v_n(t)$ at the fundamental mode; and $I_{m\circ}$ and $\gamma_{m\circ}$ denote the magnitude and phase angle of $i_m(t)$ at the fundamental mode. We can write the voltage difference between buses m and n at the fundamental mode as follows:

$$V_{m\circ}\angle\theta_{m\circ} - V_{n\circ}\angle\theta_{n\circ} = Z_\circ I_{m\circ}\angle\gamma_{m\circ}, \quad (3.1)$$

where

$$Z_o = R + j\omega_o L \quad (3.2)$$

is the impedance of the line at the fundamental mode. The circuit model under the fundamental mode is as in Fig. 3.4(b).

3.4.2 Case II: Transient Event Creates a New Mode

If the transient event creates a new oscillation mode, e.g., as in Fig. 3.2, then the dominant modes are not only the fundamental mode but also one or more new modes, as in Table 3.2. Without loss of generality, we assume that there exists only one new dominant mode in the transient event. If the transient event introduces multiple new modes, then we can simply take the dominant mode and the rest of the analysis remains the same.

Let f , $\omega = 2\pi f$, and $-\sigma$ denote the frequency, the rotational frequency, and the damping rate of the new event mode. Also, let V_m and θ_m denote the magnitude and phase angle of $v_m(t)$ at the new event mode; V_n and θ_n denote the magnitude and phase angle of $v_n(t)$ at the new event mode; and I_m and γ_m denote the magnitude and phase angle of $i_m(t)$ at the new event mode. We write the voltage difference between buses m and n at the new event mode as follows:

$$V_m \angle \theta_m - V_n \angle \theta_n = Z I_m \angle \gamma_m, \quad (3.3)$$

where

$$Z = R - \sigma L + j\omega L \quad (3.4)$$

is the impedance of the line at the new event mode. The circuit model under the new event mode is shown in Fig. 3.4(c). Notice the difference between (3.2) and (3.4) and the fact that the damping rate of the new event mode appears as a *resistive* term in (3.4).

3.4.3 Load Modeling in Cases I and II

We assume that the active and reactive power loads are given at all buses, either by direct measurements, such as via smart meters; or by using pseudo-measurements, such as via historical data or the ratings of the load transformers. This is a reasonable assumption; because the rating of the load transformers and the substation measurements are always available in practice. Importantly, the proposed method is very robust against errors in pseudo-measurements; as we will verify through case studies in Section 3.6.7. Thus, we can estimate the equivalent resistance and inductance of the load at each bus. Let R_m^d and L_m^d denote the resistance and inductance of the load at bus m ; and R_n^d and L_n^d denote the resistance and inductance of the load at bus n , as we already marked in Fig. 3.4(a). We can express the admittance of the loads at buses m and n at the fundamental mode in Case I in Section 3.4.1 as:

$$\begin{aligned} Y_{m\circ} &= 1/(R_m^d + j\omega_0 L_m^d), \\ Y_{n\circ} &= 1/(R_n^d + j\omega_0 L_n^d). \end{aligned} \tag{3.5}$$

Similarly, we can express the admittance of the loads at buses m and n at the new event mode in Case II in Section 3.4.2 as:

$$\begin{aligned} Y_m &= 1/(R_m^d - \sigma L_m^d + j\omega L_m^d), \\ Y_n &= 1/(R_n^d - \sigma L_n^d + j\omega L_n^d). \end{aligned} \tag{3.6}$$

Notice the difference between (3.5) and (3.6). The damping rate of the new event mode appears as a *resistive* term in (3.6).

In (3.5) and (3.6), we assume that all loads are constant impedance. However, other types of loads, namely constant current and constant power loads, can also be similarly

formulated and integrated into the model using pseudo-measurements. The use of other types of loads is discussed in Appendix B.

3.5 Event Location Identification Method

In this section, we propose a method to pin-point the location of a transient event. We assume that the synchronized waveform measurements are already characterized by their multi-signal modal analysis, as in Section 3.3; and the distribution feeder is already modeled, as in Section 3.4.1 or Section 3.4.2, depending on whether the transient event magnifies the existing fundamental mode or it creates a new event mode, respectively.

3.5.1 Methodology

Consider the power distribution feeder that we saw in Fig. 3.3. It has N buses. Suppose two WMUs are installed on the distribution feeder, one at the beginning of the feeder at bus 1 and one at the end of the feeder at bus N . Suppose a transient event occurs somewhere along the feeder at *unknown* bus $k \in \{1, \dots, N\}$.

Forward Sweep and Backward Sweep

The starting point in our event location identification method is to conduct a forward sweep and a backward sweep, see [69, ch. 10], on the constructed circuit model of the distribution feeder.

In forward sweep, we start from the phasor representation of the *dominant mode* that is obtained in WMU 1 at bus 1, and we calculate the nodal voltages at all the buses

on the distribution feeder at the dominant mode, all the way forward to WMU 2 at bus N .

We denote the results in forward sweep by

$$V_1^f, \dots, V_{k-1}^f, V_k^f, V_{k+1}^f, \dots, V_N^f. \quad (3.7)$$

In backward sweep, we start from the phasor representation of the *dominant mode* that is obtained in WMU 2 at bus N , and we calculate the nodal voltages at all the buses on the distribution feeder at the dominant mode, all the way back to WMU 1 at bus 1. We denote the results in backward sweep by

$$V_1^b, \dots, V_{k-1}^b, V_k^b, V_{k+1}^b, \dots, V_N^b. \quad (3.8)$$

Note that, if the transient event does *not* create any new mode, then we use the line impedance in (3.2) and the load admittance in (3.5) to conduct the forward sweep and the backward sweep. However, if the transient event *does* create any new mode, then we use the line impedance in (3.4) and the load admittance in (3.6) to conduct the forward sweep and the backward sweep.

Minimizing Discrepancy

Let Ψ_i denotes the *discrepancy index* at bus i between the results from the forward sweep in (3.7) and the results from the backward sweep in (3.8):

$$\Psi_i = |V_i^f - V_i^b|, \quad \forall i = 1, \dots, N, \quad (3.9)$$

where $|.|$ returns the magnitude of a complex number. The location of the transient event is obtained as follows:

$$k^* = \arg \min_i \Psi_i. \quad (3.10)$$

Algorithm 1 Event Location Identification: Two WMUs

Input: WMU measurements and network data

Output: The location of the transient event

- 1: // **Step I:**
 - 2: Use multi-signal modal analysis to obtain the dominant mode(s) of the captured waveforms during the transient event, such as within the green boxes in Figs. 3.1 and 3.2.
 - 3: // **Step II:**
 - 4: **if** the event does not create a new mode **then**
 - 5: Construct the circuit model based on (3.1), (3.2), and (3.5).
 - 6: **else if** the event creates a new mode **then**
 - 7: Construct the circuit model based on (3.3), (3.4), and (3.6).
 - 8: **end if**
 - 9: // **Step III:**
 - 10: Use forward sweep to obtain the nodal voltages in (3.7).
 - 11: Use backward sweep to obtain the nodal voltages in (3.8).
 - 12: Calculate the voltage discrepancies as in (3.9).
 - 13: Obtain the event bus number by using (3.10).
-

The rational in (3.10) is that the forward sweep and the backward sweep both start from direct measurements at a WMU and they continue to be correct up until we pass the unknown event bus k . At that point, the results of the forward sweep and the backward sweep both become incorrect. In the forward sweep, V_1^f, \dots, V_k^f are calculated correctly; while V_{k+1}^f, \dots, V_N^f are calculated incorrectly. In the backward sweep, V_1^b, \dots, V_{k-1}^b are calculated incorrectly; while V_k^b, \dots, V_N^b are calculated correctly. We can conclude that $V_i^f = V_i^b$ for $i = k$, while $V_i^f \neq V_i^b$ for $i \neq k$. Thus, the location of the transient event is obtained as in (3.10).

3.5.2 Algorithm

By combining the analysis in Sections 3.3, 3.4, and 3.5.1, we can develop a three-step algorithm to identify the location of transient events by using WMU measurements, as shown in Algorithm 1. In Step I, we extract the characteristics of the transient event from the captured synchronized waveform measurements by doing a multi-signal modal analysis. In Step II, we construct the circuit model of the feeder under the dominant mode(s). In Step III, we conduct a forward sweep and a backward sweep on the constructed circuit model, followed by the discrepancy analysis to identify the location of the event.

3.5.3 Extension to Arbitrary Number of WMUs

Suppose multiple WMUs are available, one is at the beginning of the feeder, and the rest are at the end of the feeder/laterals, as in Fig. 3.5. Suppose Ω is the set of buses with WMUs. For the WMU at each bus $s \in \Omega \setminus \{1\}$, let us define $\Psi_i^{1,s}$ as the discrepancy index at bus i that is obtained by using (3.9); where we start the forward sweep from the WMU at bus 1 and we start the backward sweep from the WMU at bus s . We define

$$\Psi_i = \sum_{s \in \Omega \setminus \{1\}} \Psi_i^{1,s}, \quad \forall i = 1, \dots, N. \quad (3.11)$$

Accordingly, we identify the location of the transient event at the minimum of the above combined discrepancy index. The exact procedure is shown in Algorithm 2.

Algorithm 2 Event Location Identification: Multiple WMUs

Input: WMU measurements and network data

Output: The location of the transient event

- 1: **for** the WMU at each bus $s \in \Omega \setminus \{1\}$ **do**
 - 2: Use Algorithm 1 to obtain $\Psi_i^{1,s}$ at each bus i .
 - 3: **end for**
 - 4: Obtain Ψ_i at each bus i using (3.11).
 - 5: Obtain the event bus number using (3.10).
-

3.6 Case Studies

In this section, we assess the performance of the proposed event location identification method by applying it to the IEEE 33-bus test system. The single line diagram of the test system is shown in Fig. 3.5. Five WMUs are installed on this network; as marked on the figure. Each WMU reports the synchronized voltage and current waveform measurements. The waveform measurements in this study are taken from the PSCAD/EMTDC simulation [43] and supplied to the event location identification algorithm. The nominal frequency of the system is 60 Hz. Unless stated otherwise, the reporting rate of the WMUs is assumed to be 256 samples per cycle. The incipient fault is simulated in form an arc based on the existing Cassie model in PSCAD [70, 71]. We study different scenarios of transient events, such as sub-cycle incipient faults and multi-cycle incipient faults, and permanent events, such as permanent faults and capacitor bank switching events.

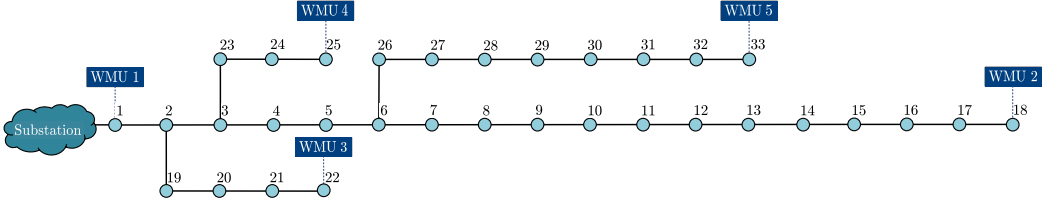


Figure 3.5: The IEEE 33-bus distribution system with five WMUs, where the set of buses with WMUs is $\Omega = \{1, 18, 22, 25, 33\}$.

3.6.1 Scenario I: Sub-cycle Incipient Fault

Suppose a sub-cycle incipient fault occurs at bus 9 and it lasts for *one quarter of a cycle*. Fig. 3.1 in Section 3.3 shows the voltage and current waveforms during this event that are captured by WMUs 1 and 2. First, we extract the modes of all the 10 waveforms from all the five WMUs by conducting a multi-signal modal analysis. The results for WMUs 1 and 2 are already shown in Table 3.1. Recall that this event does *not* create any new mode. Next, we construct the circuit model between the WMU at bus 1 and any of the other four WMUs at buses 18, 22, 25, and 33. Finally, we run Algorithm 1 for each pair of WMUs; or we run Algorithm 2 for all five WMUs.

The results of running Algorithm 1 are shown in Figs. 3.6(a)-(d); and the results of running Algorithm 2 are shown in Fig. 3.6(e). As shown in Fig. 3.6(a), if the waveform measurements are available only from WMUs 1 and 5, then the discrepancy index is minimized at buses 6 to 18, indicating that the incipient fault occurred somewhere at the downstream of bus 6. As shown in Fig. 3.6(b), if the waveform measurements are available only from WMUs 1 and 4, then the discrepancy index is minimized at buses 3 to 18, and buses 26 to 33, indicating that the fault occurred at one of these buses. As shown in Fig.

3.6(c), if the waveform measurements are available only from WMUs 1 and 3, then the discrepancy index is minimized at buses 2 to 18, and buses 23 to 33, indicating that the fault occurred at one of these buses. As shown in Fig. 3.6(d), if the waveform measurements are available only from WMUs 1 and 2, then the discrepancy index is minimized at bus 9; which is the correct event bus. Finally, as shown in Fig. 3.6(e), if the waveform measurements are available from all the five WMUs, the minimum discrepancy index occurs at bus 9; which is the correct event bus.

From the above cases, we can conclude that the proposed method is able to identify the correct location of the event even if *only two* WMUs are available; as long as the event occurs somewhere *between* those two WMUs. For example, suppose only WMU 1 and WMU 2 are available. In that case, we can *correctly* identify the location of the event if the event occurs anywhere on the main feeder, i.e., at buses 1, 2, 3, ..., 17, or 18. However, if the event occurs somewhere on the *first* lateral, i.e., at buses 19, 20, 21, or 22, then we identify bus 2, i.e., the head of the first lateral, as the event bus. This is because we do *not* have any WMU on the first lateral; of course, unless we *do* install WMU 3 at bus 22; which in that case we *can* identify the exact location of the event on the first lateral. Similarly, if the event occurs somewhere on the *second* lateral, i.e., at buses 23, 24, or 25, then we identify bus 3, i.e., the head of the second lateral, as the event bus. This is because we do *not* have any WMU on the second lateral; of course, unless we *do* install WMU 4 at bus 25; which in that case we *can* identify the exact location of the event on the second lateral. Similarly, if the event occurs somewhere on the *third* lateral, i.e., at buses 26, 27, ..., 32 or 33, then we identify bus 6, i.e., the head of the third lateral, as the event bus. This

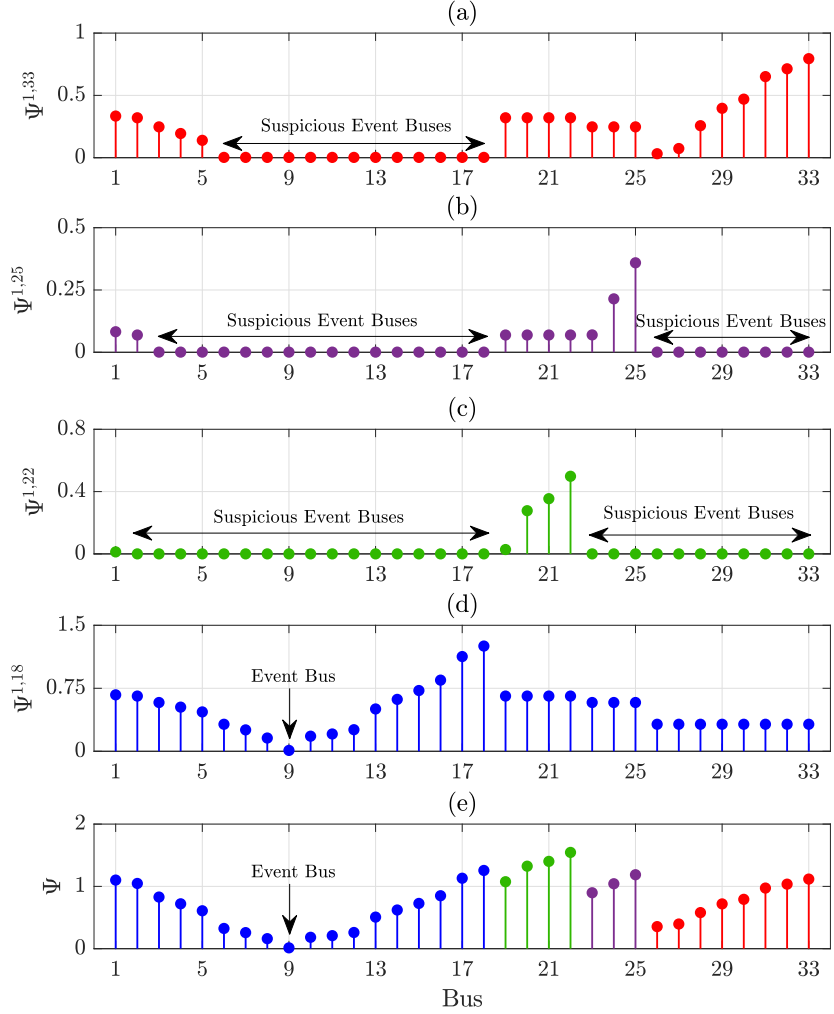


Figure 3.6: Discrepancy index in Scenario I, when the sub-cycle incipient fault occurs at bus 9 using the measurements from: (a) WMUs 1 and 5; (b) WMUs 1 and 4; (c) WMUs 1 and 3; (d) WMUs 1 and 2; (e) WMUs 1 to 5.

is because we do *not* have any WMU on the third lateral; of course, unless we *do* install WMU 5 at bus 33; which in that case we *can* identify the exact location of the event on the third lateral. In summary, the proposed method can work with at least two WMUs; depending on the location of the transient event, certain pairs of WMUs are more suitable

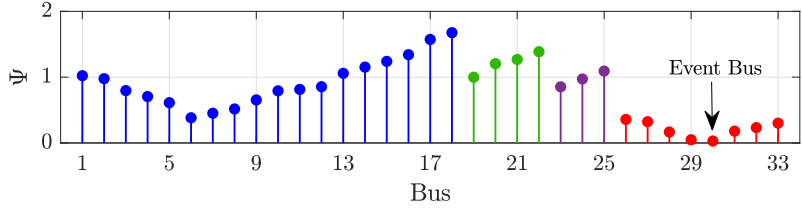


Figure 3.7: Discrepancy index in Scenario II, when the multi-cycle incipient fault occurs at bus 30, based on running Algorithm 2 on all five WMUs.

to provide the waveform measurements that can lead to correctly identify the location of the event by running Algorithm 1. However, since the event bus is *not* known in advance, it is necessary that we use the waveform measurements from all the five WMUs so that we can identify the exact location of the event; whether it occurs on the main feeder or on a lateral. For the rest of this chapter, we focus on identifying the event bus using the waveform measurements from all the five WMUs.

3.6.2 Scenario II: Multi-cycle Incipient Fault

Suppose a multi-cycle incipient fault occurs at bus 30 and it lasts for *two cycles*. As in Scenario I, this event does *not* create any new mode. Fig. 3.7 shows the results of running Algorithm 2 in this scenario based on the waveform measurements from all five WMUs. As we can see, our method is able to correctly identify bus 30 as the location of the incipient fault. This scenario further confirms the accuracy of our method.

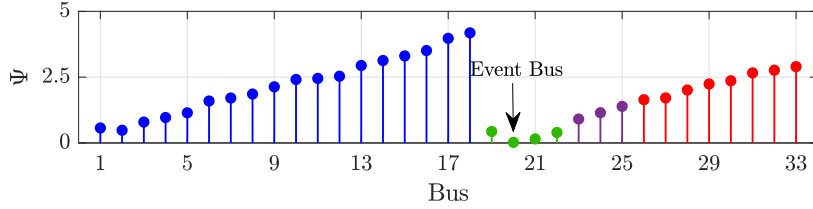


Figure 3.8: Discrepancy index in Scenario III, when the permanent fault occurs at bus 20, based on running Algorithm 2 on all five WMUs.

3.6.3 Scenario III: Permanent Fault

Suppose a permanent symmetric fault occurs at bus 20. We call it permanent because it is *not* self-cleared. It may last until it is cleared by a circuit breaker. As in Scenarios I and II; this permanent fault does *not* create any new mode. The results of running Algorithm 2 are shown in Fig. 3.8. The location of the permanent fault is correctly identified at bus 20. The results in this scenario confirm the accuracy of the proposed method even for transient events that lead to permanent events. Of course, our method still focuses only on the transient component of this event; and accordingly, it identifies its location very promptly. We will examine the performance of the proposed method for asymmetric faults in unbalanced networks later in Section 3.6.9.

3.6.4 Scenario IV: Capacitor Bank Switching Event

Suppose a capacitor bank is switched on at bus 24. Fig. 3.2 in Section 3.3 shows the voltage and current waveforms during this event that are captured by WMUs 1 and 4. The results of multi-signal modal analysis are already shown in Table 3.2. Unlike in Scenarios I, II, and III, in this scenario, the event not only magnifies the fundamental mode

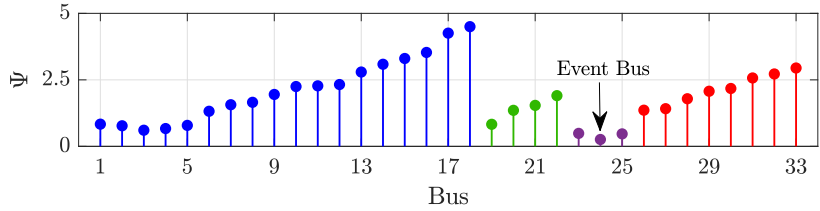


Figure 3.9: Discrepancy index in Scenario IV, when capacitor bank switching occurs at bus 24, based on running Algorithm 2 on all five WMUs.

but it also creates a new dominant mode, as we saw in Table 3.2. The results of running Algorithm 2 are shown in Fig. 3.9. As we can see, the proposed method is able to identify the correct event location.

3.6.5 Impact of Measurement Reporting Rate

Different types of WMUs may have different reporting rates. A higher reporting rate results in more information about the system and the event, but it requires larger data storage capabilities and faster data communication. A lower reporting rate leads to less information about the event, but it requires less computational efforts. Therefore, the reporting rate of WMUs can play an important role in the performance of any data-driven event analysis. In this regard, we examine the performance of the proposed event location identification method by down-sampling the reporting rate from 256 samples per cycle to 128, 64, and 32 samples per cycle. The results reveal that even when the reporting rate is as low as only 32 samples per cycle, the proposed event location identification method is able to correctly identify the location of the events in all the four types of events that we had discussed in Sections 3.6.1 to 3.6.4.

3.6.6 Performance Comparison

In this section, we compare the performance of our method with that of two state-of-the-art methods in [49] and [62].

Multi-Cycle Incipient Fault

In [49]; a distance-based method is proposed to identify the location of incipient faults. This method uses the waveform measurements from WMU 1 to estimate the distance between the fault location and the sensor location. This method does not use the measurements from the rest of the WMUs; because the fault current almost entirely flows through the substation and not through the loads. Figs. 3.10(a) and (b) show the estimated resistance and reactance, respectively, for the case of the multi-cycle incipient fault in Scenario II in Section 3.6.2. As we can see, the estimated impedance does not converge to the correct values. This is because there are loads between the sensor location and the fault location. They result in underestimating the impedance. This issue is alleviated by approximating the loads based on the measurements before the event occurs [59]. Translating the estimated impedance to distance and then to bus number, one can identify bus 27 as the event bus; which is *incorrect*. It is three buses away from bus 30, which is the correct event bus. This method also identifies bus 7 as the event bus. This is of course the main drawback of impedance-based methods that identify *multiple* locations for the event, see [52]. In summary, the method in [49] cannot identify the correct event bus. However, as we already saw in Fig. 3.7, our method can correctly identify the location of the incipient fault at bus 30.

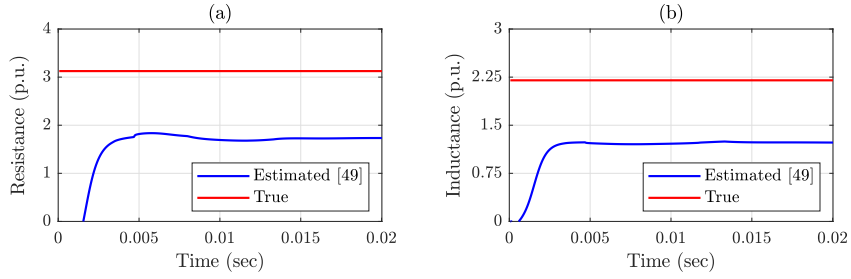


Figure 3.10: The results of estimating the impedance of an incipient fault by using the impedance-based method in [49]: (a) the estimated resistance; (b) the estimated inductance.

Capacitor Bank Switching

In [62], a method is proposed to identify the location of the capacitor bank switching event. The method is based on the Initial Value Theorem in circuit theory. It estimates the distance between the sensor location and the capacitor bank location by using the instantaneous voltages *before* and *after* the event. If we apply the method in [62] to the capacitor bank switching event in Scenario IV in Section 3.6.4, we can obtain the pre-event instantaneous voltage and the post-event instantaneous voltage as $v(t^-) = -0.952$ p.u. and $v(t^+) = -0.777$ p.u. According to [62], we can estimate the inductance from the sensor location to the event location as

$$L^{\text{est}} = \frac{v(t^+)}{v(t^-) - v(t^+)} L^{\text{th}}, \quad (3.12)$$

where L^{th} is the Thevenin inductance seen by WMU 1.

The estimated inductance is obtained as 1.049 p.u.; however the true inductance is 2.276 p.u. Translating this estimation to bus number, we identify bus 23 as the event bus. However, this is not the correct event bus. It is rather the neighboring bus of the correct bus, i.e., bus 24. It should be noted that the estimated inductance is smaller than

Table 3.3: Comparison Between [49], [62], and the Proposed Method

	[49]	[62]	Proposed Method
Methodology	Impedance-based	Initial Value-based	Wide Area-based
Type of Events	Faults	Capacitor Switching	Both
Use of Time Synchronization	No	No	Yes
Location Identification Accuracy	Low	Low	High
Robust Against Intermediate Loads	No	No	Yes

the true one. This is because there are loads between the sensor location and the fault location, which affect the estimation of impedance. In summary, the method in [62] is not able to identify the correct event bus. However, as we already saw in Fig. 3.9, our proposed method is able to correctly identify the location of the capacitor bank at bus 24.

Table 3.3 summarizes the comparison between the methods in [49], [62] and the proposed method. First, the method in [49] is designed to locate only faults, which are very severe events; and the method in [62] is designed to locate only capacitor bank switching events; however, the proposed method in this chapter can locate both types of events. Second, the proposed method is specifically designed to take advantage of the *synchronized measurements* from *multiple* WMUs; as opposed to the methods in [49] and [62] that inherently work based on measurements from one sensor; because they were designed before the advent of WMUs which have emerged only very recently. Third, the proposed method is able to identify the location of events with higher accuracy, as opposed to the methods in [49] and [62] that identify the location of certain events with considerable error. Fourth, the proposed method is not sensitive to the intermediate loads between the event location and the sensor location; as we will see in Section 3.6.7. However, such robustness is not reported for the methods in [49] and [62].

It bears mentioning that we absolutely do *not* say that there is any problem with the existing methods that use measurements from only one power quality sensor (which is the ancestor of WMU). Instead, we make the following argument: now that synchronized waveform measurements from *multiple* WMUs are gradually becoming available in practice, let us design methods that can take advantage of such *synchronized waveform* availability. The proposed method in this chapter tries to exactly do so by proposing a method that *does* take advantage of having access to synchronized waveform measurements from *multiple* WMUs. Furthermore, we show that once such data availability from multiple WMUs is used, the results can outperform the traditional methods that are designed to use waveform measurements from only one power quality sensor.

3.6.7 Sensitivity Analysis

Next, we use Monte Carlo simulation to assess the impact of errors in parameters and measurements on the accuracy of the proposed method. The number of random scenarios is 10,000.

1) Error in Line Parameters: Line inductance and resistance may deviate from their nominal values because of loading, aging, and weather conditions, to name a few. Table 3.4 shows the results for different levels of errors. As we can see, even when the error is at 50%, the proposed method can identify the correct location for the transient event in 98.9% of the random scenarios. In the remaining 1.1% of the cases, we identify the neighboring bus as the event location. Hence, the robustness of the proposed method is confirmed for errors in line parameters.

Table 3.4: Impact of Error in Line Parameters

Error (%)	Correct Bus	Neighboring Bus	Other Bus
25	100.0 %	0.0 %	0.0 %
50	98.9 %	1.1 %	0.0 %
75	93.0 %	7.0 %	0.0 %
100	85.8%	14.2 %	0.0 %

Table 3.5: Impact of Error in Pseudo-Measurements

Error (%)	Correct Bus	Neighboring Bus	Other Bus
25	100.0 %	0.0 %	0.0 %
50	100.0 %	0.0 %	0.0 %
75	100.0 %	0.0 %	0.0 %
100	99.8 %	0.1 %	0.1 %

2) Error in Pseudo-Measurements: Table 3.5 shows the location identification accuracy for different levels of errors in pseudo-measurements. Even when the error is at 100%, the proposed method can identify the correct location for the transient even in 99.8% of the random scenarios. In another 0.2% of the cases, we can still identify the neighboring bus. Thus, the robustness of the proposed method is further confirmed.

3) Noise and Harmonics in Waveform Measurements: Table 3.6 shows the results on the accuracy of the proposed event identification method for different levels of harmonics in the system as well as different levels of measurement noise in WMU measurements. The level of harmonics is specified in terms of the *total-harmonic-distortion* (THD) of the current waveforms. The measurement noise level is specified in terms of the *signal-to-noise-ratio* (SNR). As we can see, even when the THD is as high as 3% and the SNR is as low as 20 dB, the proposed method is still able to correctly identify the location of the event in 85.5% of the random scenarios. In another 6.2% of the random scenarios, an immediate neighboring bus of the correct event bus is identified. The results in Table

Table 3.6: Impact of Harmonic Distortion and Measurement Noise on the Accuracy of the Event Location Identification Method

	THD (%)	SNR (dB)	Correct Bus	Neighboring Bus	Other Bus
1		80	100.0 %	0.0 %	0.0 %
		50	100.0 %	0.0 %	0.0 %
		20	86.8 %	5.8 %	7.4 %
2		80	100.0 %	0.0 %	0.0 %
		50	99.9 %	0.1 %	0.0 %
		20	84.4 %	7.5 %	8.1 %
3		80	100.0 %	0.0 %	0.0 %
		50	99.8 %	0.2 %	0.0 %
		20	85.5 %	6.2 %	8.3 %

3.6 confirm the robustness of the proposed event location identification method even under considerable harmonic and measurement noise levels. It bears mentioning that, identifying the correct location of sub-cycle incipient faults becomes challenging when the levels of noise and harmonics in waveform measurements are high, due to their very short duration.

3.6.8 Active Distribution Networks

In this section, we apply the proposed method on an active power distribution network, i.e., a power distribution system with a Distributed Generation (DG) unit. In this regard, we install a DG at bus 33. Importantly, we do *not* include any knowledge about this DG in our analysis. In other words, we assume that we are *unaware* of the presence of this DG. Fig. 3.11 shows the results of running Algorithm 2 for the case of the sub-cycle incipient fault in Scenario I in Section 3.6.1, when the DG *is* connected to the network and when it is *not* connected to the network. As we can see, the proposed method is still able to correctly identify the location of the incipient fault at bus 9, even in the presence of the DG. Notice that, when the DG is connected to the network, the difference between the lowest

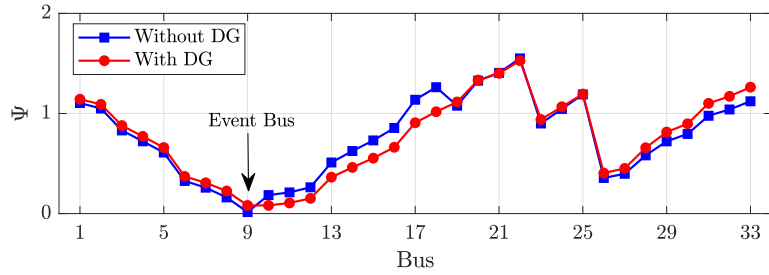


Figure 3.11: Comparing the discrepancy indices in identifying the location of the sub-cycle incipient fault in Scenario I in an *active* network and a *passive* network by running Algorithm 2 on all five WMUs.

discrepancy index and the second lowest discrepancy index is smaller; this means that the event location identification is now more challenging. However, this is simply because we assume that we do *not* know about the presence of the DG in Algorithm 2; yet we are still able to identify the location of the event correctly. If we *do* know about the DG, i.e., its location and its size, then we can reach the same accuracy as in the case without DG.

3.6.9 Extension to Unbalanced Three-Phase Networks

In this section, we apply the proposed event location identification method to an unbalanced three-phase power distribution network with asymmetric events. In this regard, first, we extend the IEEE 33-bus test system to an unbalanced three-phase network by changing the loading on the three phases. Other parameters and assumptions remain the same as those mentioned for the initial test system. Suppose a permanent two-phase line-to-ground fault on Phases A and B occurs at bus 20. It is an asymmetric event. Similar to the case of the fault in Scenario III in Section 3.6.3, this fault does not create any new mode in the system. Fig. 3.12 shows the results of running Algorithm 2 on Phases A, B,

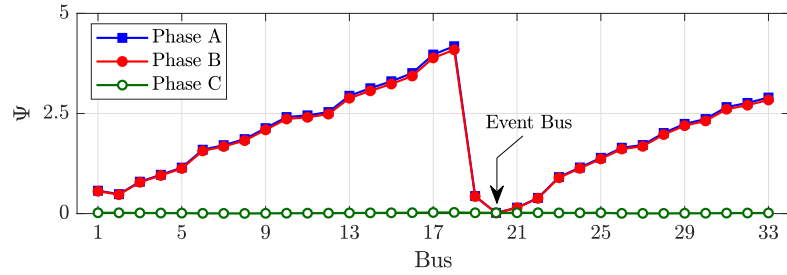


Figure 3.12: Discrepancy indices on different phases in identifying the location of an *asymmetric phase-to-phase* fault at bus 20, across Phases A and B, in an *unbalanced three-phase* network by running Algorithm 2 on all five WMUs.

and C. As we can see, the discrepancy index on Phases A and B is minimized at bus 20, indicating that the fault occurred at bus 20, which is correct. However, the discrepancy index on Phase C is almost zero at all buses, correctly indicating that the fault did not occur on Phase C. It should be noted that, there are small differences between the discrepancy indices on Phase A and Phase B. These differences are due to the load imbalance across the phases. Nevertheless, the proposed method is able to identify the correct bus as the location of the fault and it can also correctly identify Phases A and B as the phases of the fault. We can conclude that the proposed method can work well even for asymmetric events in unbalanced three-phase power distribution networks.

3.7 Conclusions of the Chapter

A novel three-step method is proposed to use synchronized waveform measurements from WMUs to identify the location of transient events, including sub-cycle and multi-cycle incipient faults, in power distribution networks. The proposed method requires

installing at least two WMUs, but its performance can further improve if we use multiple WMUs. Unlike the methods that use phasor measurements, which inherently require reaching the steady-state conditions before they can be applied, the proposed method is prompt; because it uses the waveform measurements during the transient conditions of the event. The method was tested on the IEEE 33-bus distribution network for different cases of transient events. The results confirmed the accuracy of the method in identifying the correct location of the transient events; even for very short events. The proposed method can also identify the location of permanent events, such as permanent symmetric and asymmetric faults and capacitor bank switching events. The proposed method is robust against error in line parameters and error in load parameters. Furthermore, the proposed method can reach a high accuracy, even with noisy waveform measurements and also at low measurement reporting rates. It works well also in active power distribution networks and in unbalanced three-phase networks, making the proposed method applicable in most practical power distribution networks.

Chapter 4

Network Parameters Estimation and Field Implementation

In this chapter, we propose a new data-drive framework to *estimate* the basic parameters of power distribution systems and eventually to identify the location of events by using real-world synchro-waveform measurements. In most power distribution systems, network parameters, such as line parameters, are often *unreliable* or even *not* available. Furthermore, most of the power system monitoring applications requires access such prior knowledge about the network parameters, such as in event location identification that we discussed in Chapter 3. This further highlights the need for estimating network parameters of the power distribution feeders before we run any monitoring applications. In this Chapter, we study a real-world case where the network parameters of the distribution feeder is *not* known. Instead, we are provided with the time-synchronized waveform measurements from a group of line-mounted sensors, which are inexpensive and easy to install class of WMUs. The

line-mounted sensors report the time synchronized waveforms of electric field (e-field) and current measurements in time-domain; but they do not report voltage waveform measurements. Our goal in this chapter is to identify the location of the events in the understudy distribution feeders using synchro-waveform measurements from only a few line-mounted sensors; without knowing the network parameters. This field implementation framework consists of three steps. The first step is to approximate the voltage waveform from the available e-field waveform measurement provided by the line-mounted sensors. The next step is to estimate network parameters of the distribution feeder by a novel event-based estimation method using synchronized approximated voltage waveform and synchronized current waveform measurements and to eventually reconstruct the circuit model of the distribution feeder. The proposed network parameters estimation method relies on the system condition at one AC cycle right after the event and at one AC cycle right before the event. This is the first study that proposes a novel event-based network parameters estimation that requires only data from a few locationally scarce synchro-waveform measurements and leveraging the events happening across the distribution systems. The final step is to identify the location of the events by adopting the event location identification method that we proposed in Chapter 3 on the data-driven reconstructed circuit model and leveraging the synchronized approximated voltage waveform and synchronized current waveform measurements. The framework in this chapter is purely data-driven and it is model-free. It does not require any prior information about the network. Hence, it is very suitable for real-world field implementation.

4.1 Problem Statement

In this real-world study, we are provided with the time-synchronized *electric field (e-field) waveform* and *current waveform* measurements from 12 line-mounted sensors [18] at four sites of a three-phase power distribution feeder in the United States. We do not have any prior knowledge about the network parameters of this feeder. When an event occurs, the line-mounted sensors record GPS-synchronized e-field and current waveforms. Each sensor can report 130 samples per cycle, i.e., 7,800 samples per second [18]. The locations of the sensors are known from their latitude and longitude coordinates. Sensor 1 is at the upstream of Sensor 2, Sensor 2 is at the upstream of Sensor 3, and Sensor 3 is at the upstream of Sensor 4. We label each sensor separately at each phase, thus, we denote the sensors as: $1A, 1B, 1C, \dots, 4A, 4B, 4C$. The synchronized waveform measurements are collected from all the sensors for 75 events that occurred over a period of six months, from March till August 2021.

Fig. 4.1 shows an example of the synchronized e-field waveform and current waveform measurements that are captured by the sensors during an *event* on the feeder. Based on visual inspection, we can argue that the event has occurred somewhere on Phase B between Sensor 2 and Sensor 3. The reason for this argument is that, the event causes very large changes in Phase B of the current waveform of Sensor 2, yet it causes very small changes in Phase B of the current waveform of Sensor 3. The question that we seek to answer in this chapter is: *can we use only these synchronized e-field and current waveform measurements, without any prior information about the network parameters, and automatically identify the precise location of the event?* We will show that the answer to this question is ‘Yes’.

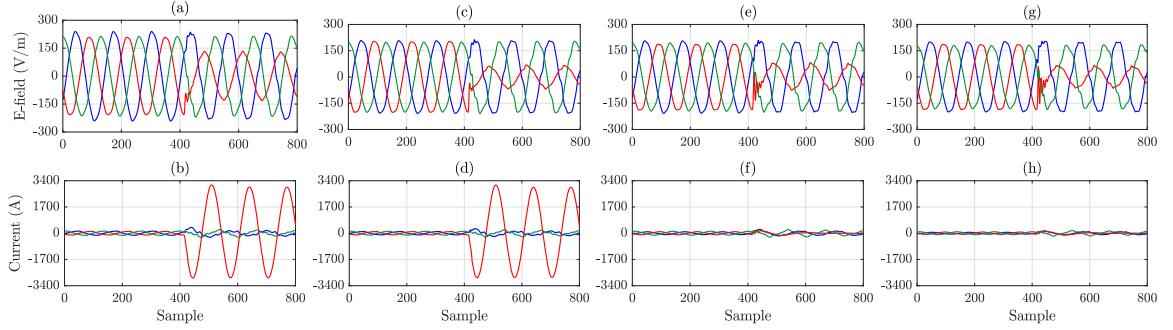


Figure 4.1: Real-world synchronized three-phase e-field waveform and three-phase current waveform measurements captured by line-mounted sensors at four sites on a distribution feeder in the United States during an event that occurred on April 26, 2021: (a)-(b) Sensor 1; (c)-(d) Sensor 2; (e)-(f) Sensor 3; (g)-(h) Sensor 4.

Different methods have been previously proposed to identify the location of events in power systems, including impedance-based methods [1, 49, 52, 72], traveling wave-based methods [73], and wide area-based methods [2, 8], as we reviewed them in Section 3.2 in Chapter 3. Of particular interest here is the work in [8] that we proposed in Chapter 3 in this thesis, which uses synchronized waveform measurements from waveform measurement units (WMUs). The method in Chapter 3 is able to identify the correct location of events in power distribution networks, including transient events, such as incipient faults, and permanent events, such as permanent faults and capacitor bank switching.

The method in Chapter 3 requires prior knowledge about the network parameters, namely the impedance of the line segments and the loading of the buses. However, such network information is *not* always available. Also, the method in Chapter 3 requires access to the synchronized voltage waveform measurements. However, in practice, the line-mounted sensors *cannot* measure voltage waveforms, instead they measure e-field waveforms.

Since the voltage waveforms and the network parameters are *not* available in this real-world problem, we propose to instead use synchronized e-field and current waveform measurements to identify the location of events in power distribution systems.

4.2 Voltage Waveform Approximation Based on Electric Field Waveform Measurements

As mentioned earlier, the line-mounted sensors in this real-world analysis do *not* measure voltage; instead, they measure e-field. The e-field and current waveform measurements are provided in *time-domain* whenever an event occurs.

Let $e(t)$ denote the e-field waveform around a line conductor that is measured by a line-mounted sensor; and let $v(t)$ denote the voltage waveform of the conductor. Since line-mounted sensors are installed very close to the conductor, they provide a very good approximation of the shape of the voltage waveform. In particular, e-field waveform measurements are almost in-phase with the voltage waveform of the conductor. Therefore, we can assume the following relationship between the voltage waveform and the e-field waveform at the conductor:

$$v(t) = \beta \times e(t), \quad (4.1)$$

where $\beta \geq 0$ is the tuning operator. We can analytically obtain β based on different environmental factors, such as the distance between the conductor and the sensor, the geometry of the conductor, and the dielectric permittivity of free space [74].

However, in this chapter, we do *not* need the true value of β , see *Lemma 1* in Section 4.4. Instead, we can consider the fact that, under normal grid operating conditions,

i.e., in the absence of an event, the voltage at any point on a conductor is very close to the voltage at the substation, where the voltage is measured directly as part of the typical substation monitoring system. Hence, we can assume that the peak amplitude of voltage waveform during normal operating conditions is available from the voltage measurements at the substation. Thus, we can obtain β in a data-driven fashion based on the peak amplitude of the e-field waveform and the peak amplitude of the voltage waveform during normal conditions and right *before* an event occurs.

For example, again consider the real-world e-field waveform measurements in Fig. 4.1(a). We can see that, the peak amplitude of the e-field waveform measurements on Phase B of Sensor 1 during the normal operating conditions, i.e., before the event occurs, is about 210 V/m. On the other hand, the under-study feeder is operated at 22.9 kV line-to-line. Thus, the peak amplitude of the voltage waveform during normal conditions is obtained as $22.9 \times 1000 \times \sqrt{2}/\sqrt{3} = 18,698$ V. Accordingly, we can obtain the tuning operator as $\beta = 18,698/210 = 89$.

Once the tuning operator is obtained, the voltage waveform can be approximated via (4.1). Similarly, we can obtain the tuning operators for other sensors on all three phases. Therefore, for the rest of this chapter, we assume that we have access to the current waveform measurements and the *approximated* voltage waveform measurements at each of the line-mounted sensors.

4.3 Reconstructing the Unknown Network Parameters

As mentioned earlier, one key advantage of the proposed framework is that we do *not* need any prior knowledge about the network parameters, namely the resistance and inductance of the distribution lines and the loading of the buses, to identify the location of events. We rather estimate those parameters based on the same measurements that we receive from the existing line-mounted sensors. We propose a novel event-based network parameter estimation method in this chapter. The method consists of three steps. First, we simplify the feeder between two WMUs during the event by using a circuit analysis intuition. Next, we estimate the network parameters of the simplified distribution feeder using a linear regression method. Finally, we completely reconstruct the feeder based on the number of utility poles and the estimated network parameters.

4.3.1 Intuition

Consider a power distribution feeder that is observed by two line sensors, as shown in Fig. 4.2(a). Let $i_1(t)$ denote the current waveform measurements and $v_1(t)$ denote the approximated voltage waveform measurements at Sensor 1. Also, let $i_2(t)$ denote the current waveform measurements and $v_2(t)$ denote the approximated voltage waveform measurements at Sensor 2. Suppose an event occurs at time $t = \tau$ at an *unknown* location. For the sake of our explanation, we assume that the event has occurred somewhere at the downstream of the two sensors, i.e., in the area that is marked in the downstream network.

To explain the intuition in obtaining the network parameters, let us first analyze the distribution feeder at one cycle, *right before* the event occurs, i.e., from time $\tau - T$

to time τ , where τ is the time that the event has occurred and $T = 16.667$ msec is the duration of one cycle. Fig. 4.2(a) shows the distribution feeder for the period from $\tau - T$ to τ . During this period, the feeder is under normal conditions, i.e., there is no event. Once the event occurs at $t = \tau$, the event current is injected to the network, as shown in Fig. 4.2(b). Given the waveforms *right before* the event occurs, i.e., from $\tau - T$ to τ , and the waveforms *right after* the event occurs, i.e., from τ to $\tau + T$, we can obtain the amount of changes in voltage waveforms and current waveforms at Sensors 1 and 2 as follows:

$$\begin{aligned}\Delta v_1(t) &= v_1(t) - v_1(t - T), \quad t = \tau, \dots, \tau + T, \\ \Delta v_2(t) &= v_2(t) - v_2(t - T), \quad t = \tau, \dots, \tau + T, \\ \Delta i_1(t) &= i_1(t) - i_1(t - T), \quad t = \tau, \dots, \tau + T, \\ \Delta i_2(t) &= i_2(t) - i_2(t - T), \quad t = \tau, \dots, \tau + T.\end{aligned}\tag{4.2}$$

By comparing the feeder *right before* the event occurs, as in Fig. 4.2(a), and the feeder *right after* the event occurs, as in Fig. 4.2(b), it is expected that the network parameters, including the line parameters and load parameters, remain the same. The reason comes from the fact that, once the event occurs, most of the event current is injected into the upstream network, because the Thevenin impedance of the upstream network is much smaller than the impedance of the load points [10]. In other words, almost all of the event current flows from the event location to the upstream network, as shown with the red line in Fig. 4.2(c). Accordingly, the currents of the line segments between Sensor 1 and Sensor 2 are the same. Thus, the changes in current waveforms at Sensor 1 and Sensor 2 are almost the same:

$$\Delta i_1(t) \simeq \Delta i_2(t), \quad t = \tau, \dots, \tau + T.\tag{4.3}$$

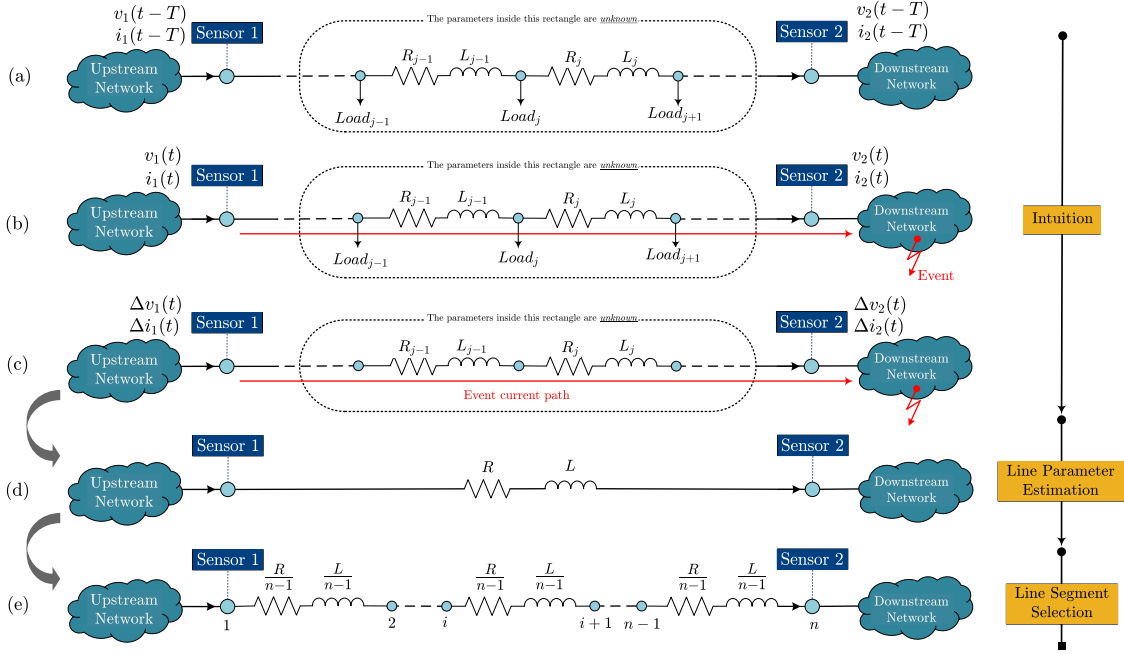


Figure 4.2: An illustration to reconstruct an unknown distribution feeder between two sensors to a known distribution feeder: (a) the feeder at one cycle *right before* the event; (b) the feeder at one cycle *right after* the event; (c) the difference between right after the event and right before the event; (d) the combined line parameters; (e) the reconstructed feeder model with even line parameters. The parameters inside the rectangle in (a)-(c) are unknown.

Thus, we can simplify the feeder between Sensor 1 and Sensor 2 during the event. That is, we can assume that there is no load points between the two sensors during the event, see Fig. 4.2(c). It should be noted that, the intuition is less reliable when the event causes very small changes in the waveform measurements.

4.3.2 Using Regression to Estimate Line Parameters

From Section 4.3.1, we can focus our analysis during the event on the simplified distribution feeder model in Fig. 4.2(c). In this simplified model, the nodal voltages are the

changes in the voltage waveforms between the two successive cycles, one cycle right after the event and one cycle right before the event, as in (4.2). Similarly, the line currents are the *changes* in current waveforms between the two successive cycles, one cycle right after the event and one cycle right before the event, as in (4.2). As a result, the line parameters of the line segments between Sensor 1 and Sensor 2 are connected in *series*, see Fig. 4.2(c).

Let R_j and L_j denote the resistance and the inductance of line segment j , respectively. Considering the series connection of the line parameters between Sensor 1 and Sensor 2 in Fig. 4.2(c), at each time $t = \tau, \dots, \tau + T$, we can write the voltage difference in time-domain between the two sensors as:

$$\begin{aligned}\Delta v_1(t) - \Delta v_2(t) &= \sum_{j \in \mathcal{S}} R_j \Delta i_1(t) + \sum_{j \in \mathcal{S}} L_j \frac{d\Delta i_1(t)}{dt}, \\ &= R \Delta i_1(t) + L \frac{d\Delta i_1(t)}{dt},\end{aligned}\quad (4.4)$$

where \mathcal{S} is the set of all the line segments between Sensor 1 and Sensor 2; R is the combined resistance that is obtained by adding up all the line resistances between Sensors 1 and 2; and L is the combined inductance that is obtained by adding up all the line inductances between Sensors 1 and 2. Fig. 4.2(d) shows the distribution feeder model with the combined line parameters R and L . We can write (4.4) in matrix form as:

$$\Delta V = \Delta I P, \quad (4.5)$$

where

$$\Delta V = \begin{bmatrix} \Delta v_1(\tau) - \Delta v_2(\tau) \\ \Delta v_1(\tau + \Delta t) - \Delta v_2(\tau + \Delta t) \\ \vdots \\ \Delta v_1(\tau + T) - \Delta v_2(\tau + T) \end{bmatrix}, \quad (4.6)$$

$$\Delta I = \begin{bmatrix} \Delta i_1(\tau) & \frac{d\Delta i_1(\tau)}{dt} \\ \Delta i_1(\tau + \Delta t) & \frac{d\Delta i_1(\tau + \Delta t)}{dt} \\ \vdots & \vdots \\ \Delta i_1(\tau + T) & \frac{d\Delta i_1(\tau + T)}{dt} \end{bmatrix}, \quad P = \begin{bmatrix} R \\ L \end{bmatrix}, \quad (4.7)$$

where $\Delta t = 120 \mu\text{sec}$ is the reporting interval of the line-mounted sensor [18].

We can estimate the line parameters in (4.5) by using the regression method with the following closed-form solution:

$$\hat{P} = (\Delta I^T \Delta I)^{-1} \Delta I^T \Delta V, \quad (4.8)$$

where \hat{P} is the estimation of the unknown line parameters.

4.3.3 Selecting the Number of Line Segments

Utility poles are used to carry overhead lines. For the sake of our analysis, we treat each pole as a bus for the feeder. Even in the absence of the utility model, the location of the utility poles can be detected by using aerial images, Google street view images, or field surveys [75]. Even if the location of the poles is not known, we can use the fact the distance between every two adjacent utility poles are usually equal. Thus, another option to obtain the number of poles is to use the distance between two sensors and the typical distance between two adjacent poles. It bears mentioning that, in cable networks, we treat each pad mounted box as a bus for the feeder.

Suppose the distance between two sensors is D and the distance between two adjacent poles is h . The number of poles between the two sensors is approximately obtained as follows:

$$n = [D/h] + 1, \quad (4.9)$$

where $[\cdot]$ returns the integer part. For example, the distance between Sensor 1 and Sensor 2 in Fig. 4.2 is 12670 ft and the typical distance between two adjacent poles of the under-study feeder is 150 ft. Thus, the number of poles/buses between Sensor 1 and Sensor 2 is $n = 85 = [12670/150] + 1$.

We number the buses from bus 1, where Sensor 1 is installed, to bus n , where Sensor 2 is installed, see Fig. 4.2(e). The number of line segments between the two sensors is $n - 1$. From (4.8), we obtain the resistance of each line as $R/(n - 1)$ and the inductance of each line as $L/(n - 1)$, as shown in Fig. 4.2(e).

The network model in Fig. 4.2(e) is the complete reconstruction of the circuit model between Sensor 1 and Sensor 2. We can similarly reconstruct the circuit model between Sensor 2 and Sensor 3, and also the circuit model between Sensor 3 and Sensor 4. This will provide us with the circuit model for the entire network. This reconstructed feeder model will be later used for event location identification. Importantly, obtaining such model does *not* require any prior information about the network parameters.

4.4 Event Location Identification

Consider the reconstructed feeder model in Fig. 4.2(e). It consists of n buses and $n - 1$ line segments. As we learned in Chapter 3, if a waveform measurement unit (WMU) is installed at the beginning of the feeder and another WMU is installed at the end of the feeder, the synchronized voltage waveform and current waveform measurements from the two WMUs can be used to accurately identify the event bus by conducting a forward

sweep and a backward sweep. Given that we have access to the current waveform and the approximated voltage waveform measurements, as in Section 4.2, and we also have access to the circuit model of the feeder, as in Section 4.3, we can now apply the event location identification method that we proposed in Chapter 3 to identify the location of events in the real-world problem in this chapter. The proposed event location algorithm in Section 3.5 in Chapter 3 is briefly summarized as follows. In the forward sweep, we start from Sensor 1 at bus 1 and calculate the nodal voltages all the way to bus n . In the backward sweep, we start from Sensor 2 at bus n and calculate the nodal voltages all the way to bus 1.

1. Suppose the location of the event is bus k . Parameter k is unknown. We can break down the calculations of the forward and backward sweeps into the following correct and incorrect calculations [8]:

$$\underbrace{\{V_1^f, \dots, V_{k-1}^f, V_k^f\}}_{\text{correct}}, \underbrace{V_{k+1}^f, \dots, V_n^f\}_{\text{incorrect}} \quad (4.10)$$

$$\underbrace{\{V_1^b, \dots, V_{k-1}^b\}}_{\text{incorrect}}, \underbrace{V_k^b, V_{k+1}^b, \dots, V_n^b\}_{\text{correct}} \quad (4.11)$$

where V_i^f and V_i^b denote the voltages at bus i that are calculated from forward and backward sweeps, respectively.

In (4.10)-(4.11), even though we do *not* know which bus is the event bus, we *do* know that the forward and backward voltage calculations at event bus k are correct. Since the *discrepancy* between the forward calculation and backward calculation is the lowest at event bus k , the event location is identified as [8]:

$$k^* = \arg \min_i |V_i^f - V_i^b| = \arg \min_i \Psi_i, \quad (4.12)$$

where Ψ_i is the discrepancy at bus i .

The above analysis can be easily extended to the case with multiple line-mounted sensors. For example, in our real-world case, if the event occurs somewhere unknown between Sensor 2 and Sensor 3, then there are two different sets of discrepancy indexes to examine. One set is obtained by using the waveform measurements from Sensor 1 and Sensor 3, denoted by $\Psi_i^{1,3}$. Another set is obtained by using the waveform measurements from Sensor 2 and Sensor 4, denoted by $\Psi_i^{2,4}$. A combined discrepancy index can be defined as $\Psi_i = \Psi_i^{1,3} + \Psi_i^{2,4}$.

It bears mentioning that, if the event occurs on a lateral, our method can still identify the bus at the beginning of the lateral as the event bus. To identify the true location of the event, it is necessary to use a sensor at the end of the lateral [2].

It is worth adding that, we do *not* need the true value of β in (4.1) to identify the location of events in this chapter. That means, the value of β in (4.1); has no impact in obtaining the location of the event. We will prove this in the following lemma.

Lemma 1: Suppose the tuning operators for Sensors 1 and 2 are the same and equal to β . The value of β has no impact on identifying the location of the event.

Proof: From (4.5), and since $\Delta v_1(t) = \beta \Delta e_1(t)$ and $\Delta v_2(t) = \beta \Delta e_2(t)$, we have $\Delta V = \beta \Delta E$. Similar to (4.8), we can obtain:

$$\hat{P} = \beta((\Delta I^T \Delta I)^{-1} \Delta I^T \Delta E) = \beta \hat{P}^e \quad (4.13)$$

Thus, the estimated line parameters using the voltage waveforms are proportional, with ratio β , to the estimated line parameters by using the e-field waveforms. Let Z_i and Z_i^e be the impedance of line segment i that are estimated by using the voltage waveform and by using the e-field waveform, respectively, where $Z_i = \beta Z_i^e$. From the Kirchoff Voltage

Law (KVL), we can obtain the nodal voltage in the forward sweep as $V_{i+1}^f = V_i^f - Z_i I_i^f$, see [2, Eq. (6)]. Thus, we can rewrite this equation as

$$\beta E_{i+1}^f = \beta E_i^f - \beta Z_i^e I_i^f \Rightarrow E_{i+1}^f = E_i^f - Z_i^e I_i^f. \quad (4.14)$$

Parameter β is canceled out from the KVL equation. Similarly, we can derive an equation in the backward sweep as $E_i^b = E_{i+1}^b + Z_i^e I_i^b$, see [2, Eq. (11)]. Accordingly, we have: $|V_i^f - V_i^b| = \beta |E_i^f - E_i^b|$. Therefore, from (4.12), the value of tuning operator β has no impact in obtaining the location of the event. ■

4.5 Case Studies

In this section, we assess the performance of the proposed framework in our real-world case that we explained in Section 4.1. The synchronized waveform measurements are collected from all the 12 sensors for 75 events that occurred over a period of six months, from March till August 2021.

4.5.1 Line Parameter Estimation Result

The structure and parameters of the under-study feeder is not available. However, we can use the latitude and longitude coordinates of the sensors to draw a picture of the distribution feeder and to obtain the distance between sites, as shown in Fig. 4.3(a). Our goal here is to estimate the network parameters of the feeder and eventually to reconstruct the complete circuit model of the distribution feeder.

First, we use the synchronized waveform measurements during the 75 captured events to estimate the combined line parameters between every two adjacent sensors on

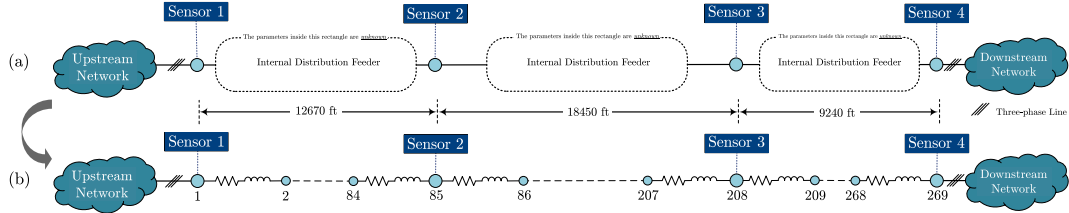


Figure 4.3: The single line diagram of the real-world power distribution feeder in the United States, with four sites of sensors: (a) a picture of the distribution feeder, where no information about the structure and parameters between every two sensors is available; (b) the corresponding constructed feeder model with 269 buses.

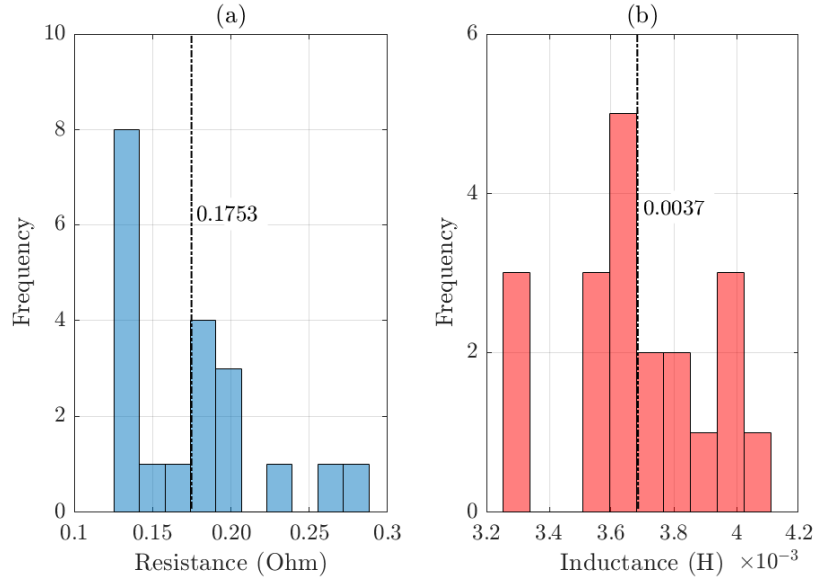


Figure 4.4: Distribution of (a) the combined resistance; (b) the combined inductance of Phase B of the line between Sensors 1 and 2 using the proposed method in Section 4.3.2. The means of the distributions are marked with dashed lines.

the same phase using the method in Section 4.3.2. Fig. 4.4 shows the distribution of the combined resistance and the combined inductance of Phase B of the line between Sensor 1

Table 4.1: Results of the Event-based Line Parameter Estimation

Sensors	Phase A		Phase B		Phase C	
	R (Ohm)	L (H)	R (Ohm)	L (H)	R (Ohm)	L (H)
1 - 2	0.1888	0.0025	0.1753	0.0037	0.1775	0.0032
2 - 3	0.2443	0.0035	0.2237	0.0029	0.2021	0.0047
3 - 4	0.2005	0.0017	0.3238	0.0032	0.2047	0.0017

and Sensor 2 using the method in Section 4.3.2.

The distribution of the estimated inductance fluctuates over a narrow range, while the estimated resistance varies over a wider range. This is because most of the events in this study have resistive characteristics which affect the estimation of the combined resistance. The average resistance and the average inductance over the number of events are marked on the dash lines. Table 4.1 shows the average value of the estimated line parameters of the overhead lines between different sensors. For the rest of this chapter, we use the average resistance and the average inductance of the lines.

Once we estimated the line parameters, next we obtain the number of poles between every two adjacent sensors using the technique in Section 4.3.3. The average distance between every two adjacent poles in this feeder is 150 ft. From (4.9), the number of poles/buses are obtained as: 85 poles between Sensors 1 and 2, 124 poles between Sensors 2 and 3, and 62 poles between Sensors 3 and 4. Thus, Sensor 1 is at bus 1, Sensor 2 is at bus 85, Sensor 3 is at bus $208 = 85 + 124 - 1$, and Sensor 4 is at bus $269 = 208 + 62 - 1$.

Fig. 4.3(b) shows the reconstructed model of the feeder. The model has 269 buses and 268 line segments. This model will be later used for event location identification.

4.5.2 Event Location Identification Results

Again consider the real-world waveform measurements in Fig. 4.1. Recall that the event in this figure occurred somewhere on Phase B between Sensor 2 and Sensor 3. Next, we apply the proposed event location identification method to identify the event bus based on the reconstructed model that we saw in Fig. 4.3(b).

Since we do *not* know which bus is the true event bus, we *cannot* verify the correctness of the event location identification results. However, we *can* check the *consistency* of the results across the following two independent sets of data: one set is the waveform data from Sensor 1B and Sensor 3B and the other set is the waveform data from Sensor 2B and Sensor 4B.

First, consider the profile for the discrepancy index $\Psi_i^{1B,3B}$ for $i = 1, \dots, 269$ in Fig. 4.5(a). The minimum is reached at bus 123. Next, consider the profile for the discrepancy index $\Psi_i^{2B,4B}$ for $i = 1, \dots, 269$ in Fig. 4.5(b). The minimum is reached at bus 93. From the results in Figs. 4.5(a) and (b), the identified event buses are always between Sensor 2 and Sensor 3, which is correct. This confirms the accuracy of the proposed event location identification method.

Importantly, the results in Figs. 4.5(a) and (b) vary in a narrow range of 31 buses from bus 93 to bus 123. Thus, it is expected that the exact location of the event, that we saw its waveforms in Fig. 4.1, is somewhere between bus 93 to bus 123. In this case, the identified zone of the event is at the downstream of Sensor 2 and somewhere between $150 \times (93 - 85 + 1) = 1350$ ft to $150 \times (123 - 85 + 1) = 5850$ ft. Accordingly, the identified event zone is $5850 - 1350 = 4500$ ft long, which is less than one mile.

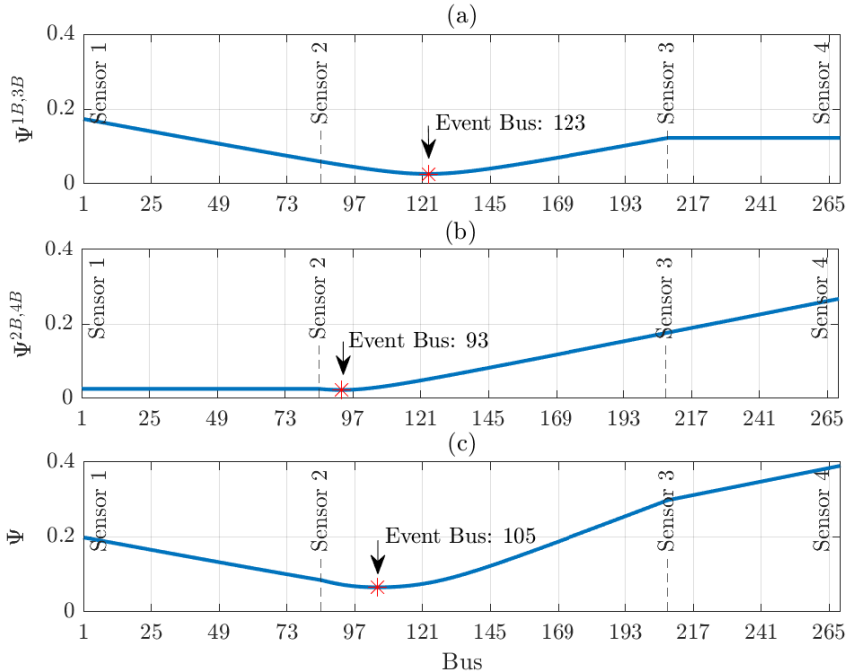


Figure 4.5: Discrepancy index using the waveform measurements from: (a) Sensors 1B and 3B; (b) Sensors 2B and 4B; (c) Sensors 1B, 2B, 3B, 4B.

The above results are much more specific than the initial event zone that we mentioned based on visual inspection in Section 4.1. Note that, such initial event zone is somewhere between Sensor 2 and Sensor 3, which is 18450 ft; see Fig. 4.3. Thus, the proposed event location identification method is able to significantly narrow down the event zone by 76% from 18450 ft to 4500 ft. This confirms the effectiveness of the proposed method. We shall emphasize that this method does not use any prior knowledge about the network parameters.

Finally, if we sum up the above two discrepancy indexes, we can obtain a combined discrepancy index $\Psi_i = \Psi_i^{1B,3B} + \Psi_i^{2B,4B}$; see Fig. 4.5(c). The minimum of the combined discrepancy occurs at bus 105, which is inside the identified event zone from bus 93 to bus 123. This confirms the consistency of the proposed event location identification method.

4.6 Conclusions of the Chapter

A model-free framework was proposed to identify the location of events using real-world synchronized e-field and current waveform data; without knowing the network parameters. We also proposed a novel event-based method to estimate network parameters of unknown power distribution networks using data from as few as only two sensors. The proposed network parameter estimation method takes advantages of events that frequently occur in power distribution systems to reconstruct the circuit model of the power distribution feeder. The proposed framework is purely data driven and model-free. It only requires data a few locationally scarce synchro-waveform measurements; it does not require any prior information about the network parameters. This is particularly important in practical power distribution networks whose network parameters are unreliable or even unknown. The proposed framework was applied to the real-world synchronized waveform measurements from 12 line-mounted sensors at four sites on a power distribution feeder in the United States. The results illustrated the accuracy, effectiveness, and consistency of the proposed method in identifying the correct location of events. On average, the proposed method is able to significantly narrow down the event zone by 76%.

Chapter 5

Conclusions and Future Works

In this section, we draw together the conclusions from the prior chapters. We also discuss future directions for follow-up research as well as some potential real-life applications of the proposed methods in this thesis.

5.1 Conclusions

The goal of this thesis was to make use of high-resolution, time-synchronized waveform measurements from a new class of smart grid sensors, called waveform measurement units (WMUs), to improve situational awareness in power distribution systems. On one hand, this thesis introduced new applications and use cases for WMUs. On the other hand, it addressed challenging problems in power distribution systems. We overview the final remarks and lessons that we learned throughout this thesis as follows.

In Chapter 1, we provided some background knowledge about the power electric grid and smart grid sensors that are useful to know throughout this thesis. We answered

to two key questions about situational awareness: 1) why do we need to focus on power distribution systems? and 2) why do we need to use smart grid sensors? We also discussed the emerging need for more accurate, high-resolution smart grid sensors to address the increased challenges in the power distribution systems and we introduced WMUs, as an emerging smart grid sensor. We also provided illustrative examples on the details that can be captured by WMUs but cannot be captured by other smart grid sensors.

In Chapter 2, we proposed new applications for WMUs data to detect and classify events in power distribution systems. The proposed methods are built upon the new concept of synchronized Lissajous curves. The proposed event detection method monitors the changes in the areas of two successive synchronized Lissajous curves. Once an event occurs, the area sharply changes, indicating that an event has occurred. The proposed event classification method works by classifying the synchronized Lissajous images. A Convolutional Neural Network (CNN) is developed as the image classification method. The proposed framework is able to correctly detect and classify a wide range of events, such as sustained events with steady-state component, e.g., high impedance fault; sustained events with transient component, e.g., capacitor bank switching; and temporary events with very short duration, e.g., incipient faults. The proposed detection and classification methods are model-free and they do not require any knowledge about the network. These methods require data from as few as only two WMUs.

In Chapter 3, we proposed a novel application for WMUs data to identify the source location of events in power distribution systems. The proposed event location identification method is based on modeling the underlying power distribution circuit at the dominant

mode of the event, which is often a complex mode comprising both oscillations and damping. The location of the source of the event is identified by using the forward and backward voltage calculations on the obtained circuit model. The proposed method is a hybrid data-driven and model-based approach; which results in an accurate and robust algorithm to identify the location of a wide range of events, such as sub-cycle incipient faults, multi-cycle incipient faults, permanent faults, as well as benign yet informative events such as capacitor bank switching. Furthermore, the proposed method can be adopted in practice at low cost, because it requires as few as only two WMUs to identify the location of an event.

In Chapter 4, we implemented the methods that we proposed in the previous chapters in a real-world distribution feeder in the United States to identify the location of events. We were faced with two key challenges in this study; one was we did not have access to network parameters of the understudy feeder, namely the impedance of the line segments and the loading of the buses, and two was we did not have access to voltage waveform measurements; instead we had access to the electric-field (e-field) waveform measurements. We addressed the first challenge by proposing a novel data-driven method to estimate network parameters of the unknown power distribution systems. The proposed network parameter estimation method takes advantages of events that frequently occur in power distribution systems to compensate the deficiency in measurements information. We addressed the second challenge by approximating the voltage waveform from the available e-field waveform measurements through a tuning operator. The proposed field implementation framework also brings together the event location identification method in Chapter 3 in this real-world case. The proposed framework is purely data-driven, i.e., it is model-free, and it does not

require any prior knowledge about the network parameters. Hence, this framework is very suitable for real-world field implementation, as it is evident from the results that is able to significantly narrow down the event zone by 76% by using data from only a few sensors.

5.2 Discussion on Potential Real-Life Applications

While the focus in this thesis is on the core technical tasks of event detection, event classification, and event location identification in synchro-waveform measurements, the results can ultimately support different real-life applications. Some of these potential applications are discussed as follows.

First, the methodologies that are developed in this thesis can help improve situational awareness with respect to the state of *health* and *safety* of various equipment in power distribution systems. In particular, by detecting and identifying incipient faults, the utility can take remedial actions in a timely manner to prevent catastrophic damages in the future, i.e., to resolve a major future failure while it is still in its early stages. Of course, since incipient faults are usually self-clearing and last for only a very short period of time [1, 8], improving our ability to detect and classify incipient faults can directly benefit the ultimate real-life applications in this area.

Second, detection and identification of specific equipment, such as capacitor banks, can also help with scrutinizing the operation of certain equipment of interest. This can benefit us with not only identifying any potential malfunctions but also updating the utility models to keep track of the changes in the system due to equipment aging [2]. The latter results can help improve the overall operation of the power distribution system.

Finally, as for the real-life applications of detecting and identifying high impedance faults, and even some incipient faults, they can be used for instance in wildfire detection and prevention [76–78]. Note that, a high impedance fault occurs when a line conductor touches a high grounding impedance object, such as during vegetation intrusion or when the power line is down. These circumstances can cause ignition and ultimately lead to wildfire [79]. In fact, many of the most destructive wildfires in California are reported to be caused by power equipment issues, see [80]. Hence, early detection and identification of high impedance faults can contribute to improving our ability to detect and prevent wildfires.

5.3 Future Works

The analysis in this thesis can be extended in various directions. In fact, we believe that the proposed synchronized Lissajous curves can be insightful even beyond event detection and event classification. For example, one option for future work is to examine the synchronized Lissajous curves to identify the location of events, specially during transient events and incipient faults. Another potential extension is to examine multi-dimensional images; which can be constructed to using synchronized waveform measurements from several sensors. Other extensions could include applying other methods in image processing to conduct event classification based on synchronized Lissajous images; such as the methods that are used in optical character recognition in computer vision.

Appendix A

Multi-Signal Modal Analysis

The multi-signal modal analysis in this thesis is done by using the multi-signal Prony method to simultaneously extract the modes of multiple waveform measurements. This is done by applying optimal curve fitting to the waveform measurements by using the least squares technique. Suppose $x_m(t)$ is one of the signals of the waveform measurements, where $m = 1, \dots, M$. Here, M is the number of signals. For example, if we have two WMUs and each WMU provides one signal for voltage waveform measurements and one signal for current waveform measurements, then $M = 4$. The goal of the Multi-signal Prony method is to fit a *damped sinusoidal model* to $x_m(t)$, along with all other waveform signals in the system, to estimate $\hat{x}_m(t)$ as follows:

$$\hat{x}_m(t) = \sum_{p=1}^P A_{p,m} e^{\sigma_p t} \cos(2\pi f_p t + \theta_p), \quad (\text{A.1})$$

where f_p and σ_p denote the frequency and the damping rate at mode p in the system; and $A_{p,m}$ and $\theta_{p,m}$ denote the amplitude and phase angle at mode p of waveform measurement m . Notice that, while f_p and σ_p are the same for all signals, each signal has its own $A_{p,m}$

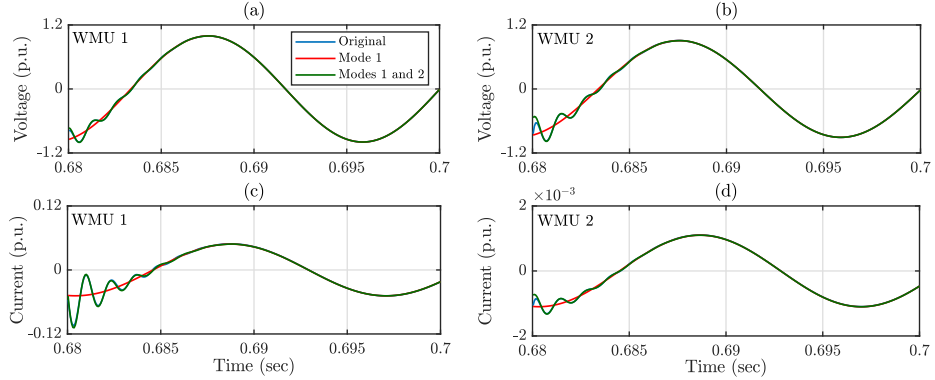


Figure A.1: An example for multi-signal Prony analysis in Appendix A: (a)-(b) voltage signals; (c)-(d) current signals. The blue curves are the original transient component of the waveform measurements in Fig. 3.2. The red curves are the reconstructed waveform measurements by using the first dominant mode. The green curves are the reconstructed waveform measurements by using both the first and the second dominant modes.

and $\theta_{p,m}$. In this regard, the phasor representation of waveform signal $x_m(t)$ at mode p is $A_{p,m} \angle \theta_{p,m}$. Fig. A.1 shows an illustrative example of the original transient components for each signal $x_m(t)$ of the total of $M = 4$ waveform measurements in Fig. 3.2 that we saw in Chapter 3, and their corresponding signal estimations $\hat{x}_m(t)$. The *blue* curves are the original waveforms, i.e., $x_m(t)$, the *red* curves are the estimated waveforms, i.e., $\hat{x}_m(t)$, which are obtained by using the first dominant mode, and *green* curves are the estimated waveforms, i.e., $\hat{x}_m(t)$, which are obtained by using the first and the second dominant modes. As we can see, the *reconstructed* waveforms using the first two dominant modes fit the original waveforms the best. The *root mean square error* (RMSE) of the red curves is about 2.4%, and the RMSE of the green curves is about 0.5%. Therefore, we can fully capture the transient behavior of the capacitor bank switching event with only the first two dominant modes. The characteristics of the first two dominant modes are shown in Table 3.2 in Chapter 3.

Appendix B

Load Types

Any load can be expressed in the generic form of an exponential model [82]. Specifically, the apparent power consumption of the load connected to bus i can be modeled as:

$$S_i = P_{io} \left(\frac{V_i}{V_{io}} \right)^{\eta_p} + Q_{io} \left(\frac{V_i}{V_{io}} \right)^{\eta_q}, \quad (\text{B.1})$$

where P_{io} , Q_{io} , and S_i denote the nominal active power, nominal reactive power, and operating apparent power of the load at bus i ; V_{io} and V_i denote the nominal and operating nodal voltage of bus i . In (B.1), if $\eta_p = 0, 1, 2$, then the load is *constant power*, *constant current*, and *constant impedance*, respectively. The reactive power component can be defined similarly by using η_q . In this equation, the nominal values P_{io} , Q_{io} and V_{io} are known at each bus i ; and the operating nodal voltage V_i is obtained from forward sweep and backward sweep calculations in (3.7) and (3.8) in Chapter 3. As a result, one can obtain S_i from (B.1) depending on the type of the load. Next, the resistance and inductance of the load at bus

i is obtained as follows:

$$R_i^d = \operatorname{Re} \left\{ \frac{V_i^2}{S_i^*} \right\}, \quad L_i^d = \frac{1}{\omega_o} \operatorname{Im} \left\{ \frac{V_i^2}{S_i^*} \right\} \quad (\text{B.2})$$

where $*$ returns the complex conjugate; $\operatorname{Re}\{\cdot\}$ and $\operatorname{Im}\{\cdot\}$ return the real part and the imaginary part, respectively. Once the resistance and inductance are obtained, the admittance of the load can be obtained via either (3.5) or (3.6), depending on the dominant mode. Of course, this makes the nodal voltages in (3.7) and (3.8) more complicated to calculate. However, the rest of the analysis in Section 3.5 in Chapter 3, which is based on examining the discrepancy between the forward sweep and backward sweep calculations, will remain the same.

Bibliography

- [1] H. Mohsenian-Rad, *Smart Grid Sensors: Principles and Applications*. Cambridge University Press, Cambridge, UK, 2022.
- [2] M. Izadi and H. Mohsenian-Rad, “Event location identification in distribution networks using waveform measurement units,” in *Proc. IEEE PES ISGT Europe*, the Hague, Netherlands, 2020, pp. 924–928.
- [3] M. Izadi, M. J. Mousavi, J. Min Lim, and H. Mohsenian-Rad, “Data-driven event location identification without knowing network parameters using synchronized electric-field and current waveform data,” in *Proc. IEEE PES General Meeting*, Denver, CO, 2022, pp. 1–5.
- [4] Grid Modernization and the Smart Grid. [Online]. Available: <https://www.energy.gov/>
- [5] W. R. Cassel, “Distribution management systems: functions and payback,” *IEEE Transactions on Power Systems*, vol. 8, no. 3, pp. 796–801, Aug. 1993.
- [6] H. Mohsenian-Rad, E. Stewart, and E. Cortez, “Distribution synchrophasors: pairing big data with analytics to create actionable information,” *IEEE Power Energy Mag.*, vol. 16, no. 3, pp. 26–34, May 2018.
- [7] M. Izadi and H. Mohsenian-Rad, “Characterizing synchronized lissajous curves to scrutinize power distribution synchro-waveform measurements,” *IEEE Trans. Power Syst.*, vol. 36, no. 5, pp. 4880–4883, Sep. 2021.
- [8] M. Izadi and H. Mohsenian-Rad, “Synchronous waveform measurements to locate transient events and incipient faults in power distribution networks,” *IEEE Trans. Smart Grid*, vol. 12, no. 5, pp. 4295–4307, Sep. 2021.
- [9] M. Izadi and H. Mohsenian-Rad, “A synchronized Lissajous-based approach to achieve situational awareness using synchronized waveform measurements,” in *Proc. IEEE PES General Meeting*, Washington, DC, 2021, pp. 1–5.
- [10] M. Izadi and H. Mohsenian-Rad, “A synchronized Lissajous-based method to detect and classify events in synchro-waveform measurements in power distribution networks,” *IEEE Trans. Smart Grid*, vol. 13, no. 3, pp. 2170–2184, May 2022.

- [11] A. F. Bastos, S. Santoso, W. Freitas, and W. Xu, "Synchronwaveform measurement units and applications," in *Proc. IEEE PES General Meeting*, Atlanta, GA, USA, 2019, pp. 1–5.
- [12] [Online]. Available: <https://selinc.com>
- [13] [Online]. Available: <https://www.candura.com>
- [14] T. Cooke, "Condensing pq data and visualization analytics," in Panel Session in *Proc. IEEE Power and Energy Society General Meeting*, 2015, pp. 1–25. [Online]. Available: <http://www.ieee-pes.org>
- [15] H. Akhavan-Hejazi and H. Mohsenian-Rad, "Power systems big data analytics: An assessment of paradigm shift barriers and prospects," *Energy Reports*, vol. 4, pp. 91–100, Nov. 2018.
- [16] K. L. Butler-Purry and M. Bagriyanik, "Characterization of transients in transformers using discrete wavelet transforms," *IEEE Trans. Power Syst.*, vol. 18, no. 2, pp. 648–656, May 2003.
- [17] T. S. Sidhu and Z. Xu, "Detection of incipient faults in distribution underground cables," *IEEE Trans. Power Deli.*, vol. 25, no. 3, pp. 1363–1371, Jul. 2010.
- [18] [Online]. Available: <https://www.sentient-energy.com>
- [19] D. Macii and D. Petri, "Rapid voltage change detection: Limits of the IEC standard approach and possible solutions," *IEEE Trans. Instrnm. Meas.*, vol. 69, no. 2, pp. 382–392, Feb. 2020.
- [20] W. Gao and J. Ning, "Wavelet-based disturbance analysis for power system wide-area monitoring," *IEEE Trans. Smart Grid*, vol. 2, no. 1, pp. 121–130, Mar. 2011.
- [21] S. M. A. Bhuiyan, J. Khan, and G. Murphy, "WPD for detecting disturbances in presence of noise in smart grid for PQ monitoring," *IEEE Trans. Ind. Appl.*, vol. 54, no. 1, pp. 702–711, Jan.-Feb. 2018.
- [22] P. K. Ray, N. Kishor, and S. R. Mohanty, "Islanding and power quality disturbance detection in grid-connected hybrid power system using wavelet and S-transform," *IEEE Trans. Smart Grid*, vol. 3, no. 3, pp. 1082–1094, Sep. 2012.
- [23] S. Santoso, W. M. Grady, E. J. Powers, J. Lamoree, and S. C. Bhatt, "Characterization of distribution power quality events with Fourier and wavelet transforms," *IEEE Trans. Power Deli.*, vol. 15, no. 1, pp. 247–254, Jan. 2000.
- [24] P. D. Achlerkar, S. R. Samantaray, and M. Sabarimalai Manikandan, "Variational mode decomposition and decision tree based detection and classification of power quality disturbances in grid-connected distributed generation system," *IEEE Trans. Smart Grid*, vol. 9, no. 4, pp. 3122–3132, Jul. 2018.

- [25] S. Mishra, C. N. Bhende, and B. K. Panigrahi, “Detection and classification of power quality disturbances using S-transform and probabilistic neural network,” *IEEE Trans. Power Deli.*, vol. 23, no. 1, pp. 280–287, Jan. 2008.
- [26] Z. Liu, Y. Cui, and W. Li, “A classification method for complex power quality disturbances using EEMD and rank wavelet SVM,” *IEEE Trans. Smart Grid*, vol. 6, no. 4, pp. 1678–1685, Jul. 2015.
- [27] A. J. Wilson, D. R. Reising, R. W. Hay, R. C. Johnson, A. A. Karrar, and T. Daniel Loveless, “Automated identification of electrical disturbance waveforms within an operational smart power grid,” *IEEE Trans. Smart Grid*, vol. 11, no. 5, pp. 4380–4389, Sep. 2020.
- [28] S. Ekici, F. Ucar, B. Dandil, and R. Arghandeh, “Power quality event classification using optimized bayesian convolutional neural networks,” *Electr. Eng.*, vol. 103, p. 67–77, Feb. 2021.
- [29] S. K. G. Manikonda, S. Gangwani, S. P. K. Sreckala, J. Santhosh, and D. N. Gaonkar, “Power quality event classification using convolutional neural networks on images,” in *Proc. IEEE Int’ Conf. Energy Syst. Inf. Process. (ICESIP)*, Chennai, India, 2019, pp. 1–5.
- [30] S. Wang and P. Dehghanian, “On the use of artificial intelligence for high impedance fault detection and electrical safety,” *IEEE Trans. Ind Appl.*, vol. 56, no. 6, pp. 7208–7216, Nov.-Dec. 2020.
- [31] A. Bagheri, I. Y. H. Gu, M. H. J. Bollen, and E. Balouji, “A robust transform-domain deep convolutional network for voltage dip classification,” *IEEE Trans. Power Deli.*, vol. 33, no. 6, pp. 2794–2802, Dec. 2018.
- [32] C. A. Desoer and E. S. Kuh, *Basic Circuit Theory*. New Delhi, India: Tata McGraw-Hill, 2009.
- [33] D. Karacor, S. Nazlibilek, M. H. Sazli, and E. S. Akarsu, “Discrete Lissajous figures and applications,” *IEEE Trans. Instrum. Meas.*, vol. 63, no. 12, pp. 2963–2972, Dec. 2014.
- [34] T. Hong and F. de León, “Lissajous curve methods for the identification of nonlinear circuits: calculation of a physical consistent reactive power,” *IEEE Trans. Circuits Syst. I, Reg. Papers*, vol. 62, no. 12, pp. 2874–2885, Dec. 2015.
- [35] A. Abu-Siada and S. Mir, “A new on-line technique to identify fault location within long transmission lines,” *Engineering Failure Analysis*, vol. 105, pp. 52–64, Nov. 2019.
- [36] C. Leys, C. Ley, O. Klein, P. Bernard, and L. Licata, “Detecting outliers: Do not use standard deviation around the mean, use absolute deviation around the median,” *Journal of Experimental Social Psychology*, vol. 49, no. 4, pp. 764–766, Jul. 2013.

- [37] MathWorks. Matlab Help Center - Getframe. [Online]. Available: <https://www.mathworks.com/help/matlab/ref/getframe.html>
- [38] MathWorks. Matlab Help Center - Frame2im. [Online]. Available: <https://www.mathworks.com/help/matlab/ref/frame2im.html>
- [39] K. Simonyan and A. Zisserman, “Very deep convolutional networks for large-scale image recognition,” *arXiv preprint arXiv:1409.1556*, 2015.
- [40] A. Krizhevsky, I. Sutskever, and G. E. Hinton, “ImageNet classification with deep convolutional neural networks,” in *Proc. Advances Neural Inf. Process. Syst.*, vol. 25, 2012, p. 1097–1105.
- [41] V. Nair and G. E. Hinton, “Rectified linear units improve restricted boltzmann machines,” in *Proc. Int’l Conf. Mach Learn.*, Haifa, Israel, 2010, pp. 807–814.
- [42] [Online]. Available: <https://www.mathworks.com/discovery/convolutional-neural-network-matlab>
- [43] Manitoba HVDC Research Centre. ver. 4.2 PSCAD/EMTDC (Software Package), Winnipeg, MB, Canada.
- [44] D. P. Kingma and J. Ba, “Adam: A method for stochastic optimization,” *arXiv preprint arXiv:1412.6980*, 2014.
- [45] EPRI/DOE National Database Repository of Power System Events. [Online]. Available: <http://pqmon.epri.com>
- [46] Real Time Digital Simulator (RTDS). [Online]. Available: <http://www.rtds.com>
- [47] Real Time Digital Simulator Tutorial Manual. ver. RSCAD FX (Software Package), Winnipeg, MB, Canada..
- [48] M. Farajollahi, A. Shahsavari, E. Stewart, and H. Mohsenian-Rad, “Locating the source of events in power distribution systems using micro-PMU data,” *IEEE Trans. Power Syst.*, vol. 33, no. 6, pp. 6343–6354, Nov. 2018.
- [49] S. Kulkarni, S. Santoso, and T. A. Short, “Incipient fault location algorithm for underground cables,” *IEEE Trans. Smart Grid*, vol. 5, no. 3, pp. 1165–1174, May 2014.
- [50] T. Takagi, Y. Yamakoshi, M. Yamaura, R. Kondow, and T. Matsushima, “Development of a new type fault locator using the one-terminal voltage and current data,” *IEEE Trans. Power App. Syst.*, vol. PAS-101, no. 8, pp. 2892–2898, Aug. 1982.
- [51] X. Yang, M. Choi, S. Lee, C. Ten, and S. Lim, “Fault location for underground power cable using distributed parameter approach,” *IEEE Trans. Power Syst.*, vol. 23, no. 4, pp. 1809–1816, Nov. 2008.
- [52] R. Krishnathevar and E. E. Ngu, “Generalized impedance-based fault location for distribution systems,” *IEEE Trans. Power Deli.*, vol. 27, no. 1, pp. 449–451, Jan. 2012.

- [53] X. Wang, H. Zhang, F. Shi, Q. Wu, V. Terzija, W. Xie, and C. Fang, “Location of single phase to ground faults in distribution networks based on synchronous transients energy analysis,” *IEEE Trans. Smart Grid*, vol. 11, no. 1, pp. 774–785, Jan. 2020.
- [54] Q. Cui and Y. Weng, “Enhance high impedance fault detection and location accuracy via μ -PMUs,” *IEEE Trans. Smart Grid*, vol. 11, no. 1, pp. 797–809, Jan. 2020.
- [55] M. M. Alamuti, H. Nouri, R. M. Cirić, and V. Terzija, “Intermittent fault location in distribution feeders,” *IEEE Trans. Power Deli.*, vol. 27, no. 1, pp. 96–103, Jan. 2012.
- [56] C. Kim, T. Bialek, and J. Awiylika, “An initial investigation for locating self-clearing faults in distribution systems,” *IEEE Trans. Smart Grid*, vol. 4, no. 2, pp. 1105–1112, Jun. 2013.
- [57] H. Nouri, M. M. Alamuti, and M. Montakhab, “Time-based fault location method for LV distribution systems,” *Electr. Eng.*, vol. 98, p. 87–96, Mar. 2016.
- [58] W. Zhang, X. Xiao, K. Zhou, W. Xu, and Y. Jing, “Multicycle incipient fault detection and location for medium voltage underground cable,” *IEEE Trans. Power Deli.*, vol. 32, no. 3, pp. 1450–1459, Jun. 2017.
- [59] A. R. Herrera-Orozco, A. S. Bretas, C. Orozco-Henao, L. U. Iurinic, and J. Mora-Flórez, “Incipient fault location formulation: a time-domain system model and parameter estimation approach,” *Elect. Power Energy Syst.*, vol. 90, pp. 112–123, Sep. 2017.
- [60] A. S. Bretas, A. R. Herrera-Orozco, C. A. Orozco-Henao, L. U. Iurinic, and J. Mora-Flórez, “Incipient fault location method for distribution networks with underground shielded cables: A system identification approach,” *Int. Trans. Electr. Energy Syst.*, vol. 27, no. 12, pp. 1–19, Oct. 2017.
- [61] L. A. da Costa, D. S. Gazzana, R. C. Leborgne, and D. W. P. Thomas, “Incipient fault location in underground distribution networks using electromagnetic time reversal,” in *IEEE EEEIC/ICPS Europe*, Madrid, Spain, 2020, pp. 1–6.
- [62] H. Khani, M. Moallem, S. Sadri, and M. Dolatshahi, “A new method for online determination of the location of switched capacitor banks in distribution systems,” *IEEE Trans. Power Deli.*, vol. 26, no. 1, pp. 341–351, Jan. 2011.
- [63] K. Hur and S. Santoso, “On two fundamental signatures for determining the relative location of switched capacitor banks,” *IEEE Trans. Power Deli.*, vol. 23, no. 2, pp. 1105–1112, Apr. 2008.
- [64] S. Xiong, Y. Liu, J. Fang, J. Dai, L. Luo, and X. Jiang, “Incipient fault identification in power distribution systems via human-level concept learning,” *IEEE Trans. Smart Grid*, vol. 11, no. 6, pp. 5239–5248, Nov. 2020.
- [65] Y. Hu, W. Wu, and B. Zhang, “A fast method to identify the order of frequency-dependent network equivalents,” *IEEE Trans. Power Syst.*, vol. 31, no. 1, pp. 54–62, Jan. 2016.

- [66] M. L. Crow and A. Singh, "The matrix pencil for power system modal extraction," *IEEE Trans. Power Syst.*, vol. 20, no. 1, pp. 501–502, Feb. 2005.
- [67] M. H. J. Bollen, E. Styvaktakis, and Irene Yu-Hua Gu, "Categorization and analysis of power system transients," *IEEE Trans. Power Deli.*, vol. 20, no. 3, pp. 2298–2306, Jul. 2005.
- [68] D. J. Trudnowski, J. M. Johnson, and J. F. Hauer, "Making prony analysis more accurate using multiple signals," *IEEE Trans. Power Syst.*, vol. 14, no. 1, pp. 226–231, Feb. 1999.
- [69] W. Kersting, *Distribution System Modeling and Analysis*. Boca Raton, FL: CRC Press, 2002.
- [70] T. E. Browne, "Practical modeling of the circuit breaker arc as a short line fault interrupter," *IEEE Trans. Power App. Syst.*, vol. PAS-97, no. 3, pp. 838–847, May 1978.
- [71] G. Idarraga Ospina, D. Cubillos, and L. Ibanez, "Analysis of arcing fault models," in *IEEE/Power Energy Soc. Transm. Distrib. Conf. Expo.*, Bogota, Colombia, 2008, pp. 1–5.
- [72] L. Iurinic, A. Herrera-Orozco, R. Ferraz, and A. Bretas, "Distribution systems high-impedance fault location: A parameter estimation approach," *IEEE Trans. Power Deli.*, vol. 31, no. 4, pp. 1806–1814, Aug. 2016.
- [73] A. Borghetti, M. Bosetti, C. A. Nucci, M. Paolone, and A. Abur, "Integrated use of time-frequency wavelet decompositions for fault location in distribution networks: theory and experimental validation," *IEEE Trans. Power Deli.*, vol. 25, no. 4, pp. 3139–3146, Oct. 2010.
- [74] K. Chen, X. Yang, and W. Xu, "Contactless voltage distortion measurement using electric field sensors," *IEEE Trans. Smart Grid*, vol. 9, no. 6, pp. 5643–5652, Nov. 2018.
- [75] W. Zhang, C. Witharana, W. Li, C. Zhang, X. Li, and J. Parent, "Using deep learning to identify utility poles with crossarms and estimate their locations from google street view images," *Sensors*, vol. 18, Aug. 2018.
- [76] M. Izadi. Preventing Wildfires Caused by Electrical Power Grid Systems. [Online]. Available: <https://www.youtube.com>
- [77] H. Mohsenian-Rad, "Synchro-waveforms in power distribution with application to wildfire monitoring," in Panel Session in *Proc. IEEE Power and Energy Society General Meeting*, Jul. 2021. [Online]. Available: <http://www.ieee-pes.org>
- [78] S. Jazebi, F. de León, and A. Nelson, "Review of wildfire management techniques—part I: causes, prevention, detection, suppression, and data analytics," *IEEE Trans. Power Deli.*, vol. 35, no. 1, pp. 430–439, Feb. 2020.

- [79] J. A. Wischkaemper, C. L. Benner, B. Don Russell, and K. Muthu Manivannan, “Application of advanced electrical waveform monitoring and analytics for reduction of wildfire risk,” in *Proc. IEEE PES ISGT*, Washington, DC, 2014, pp. 1–5.
- [80] Top 20 most destructive California wildfires, *California Department of Forestry and Fire Protection*, Sacramento, CA, USA, 2021. [Online]. Available: <https://www.fire.ca.gov>
- [81] B. Gao, R. Torquato, W. Xu, and W. Freitas, “Waveform-based method for fast and accurate identification of subsynchronous resonance events,” *IEEE Trans. Power Syst.*, vol. 34, no. 5, pp. 3626–3636, Sep. 2019.
- [82] J. V. Milanovic, K. Yamashita, S. Martínez Villanueva, S. Djokic, and L. M. Korunović, “International industry practice on power system load modeling,” *IEEE Trans. Power Syst.*, vol. 28, no. 3, pp. 3038–3046, Aug. 2013.